Chapter 2
Cooling Systems of Electronic Devices

We attempt here to describe the fundamental equations of fluid mechanics and heat transfer. The main emphasis, however, is on understanding the physical principles and on application of the theory to realistic problems. The state of the art in high-heat flux management schemes, pressure and temperature measurement, pressure drop and heat transfer in single-phase and two-phase micro-channels, design and fabrication of micro-channel heat sinks are discussed.

2.1 High-Heat Flux Management Schemes

With the trend towards increasing levels of integration in high-density, very large-scale integral circuits and heat sink technologies, higher level of performance are required to meet the elevated power dissipation in electronic and optical devices. Thermal design for cooling of microprocessor packages has become increasingly challenging in its thermal and fabrication aspects. Figure 2.1 shows the International Technology Roadmap for Semiconductors (ITRS) (Prasher et al. 2005). The upper line corresponds to high-performance semiconductors.

It can be seen that thermal design power (TDP) rises linearly up to about 2009–2010 and is expected to remain approximately constant afterwards. However, these data do not indicate whether new cooling technologies are needed for future packages. Due to die shrinkage and to other complexities of electronic and optical design, the heat flux will increase drastically, leading to highly non-uniform heat generation that will in turn cause localized hotspots. Breakthroughs in many semiconductor technologies are becoming increasingly dependent upon the ability to safely dissipate enormous amounts of heat from very small areas. Frequently, advanced electronic, optical, nuclear equipment and high-frequency microwave systems require cooling of some devices at heat fluxes on the order of $10^3\ \mathrm{W/cm^2}$ (Hetsroni et al. 2006a). Fusion reactors, for example, contain components that require continuous

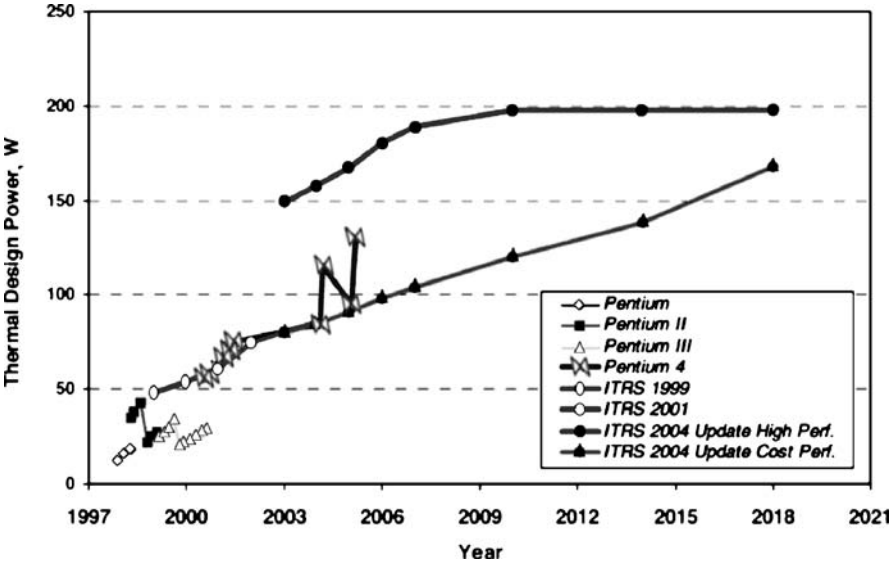

Fig. 2.1 International Technology Roadmap for Semiconductors (ITRS). Reprinted from Prasher et al. (2005) with permission

cooling on the order of $10^4\,\mathrm{W/m^2}$ (Boyd 1985). Cooling schemes exploiting recent research developments in high-heat flux thermal management were discussed and compared as to their potential heat dissipation reliability and packaging aspects by Lasance (Philips Research Laboratories) and Simons (IBM Corporation) (Lasance and Simons 2005). Some of these results are presented below.

Conduction and heat spreading

In all cooled appliances, the heat from the device's heat sources must first arrive via thermal conduction at the surfaces exposed to the cooling fluid before it can be transferred to the coolant. For example, as shown in Fig. 2.2, it must be conducted from the chip through the lid to the heat sink before it can be discharged to the ambient air. As can be seen, thermal interface materials (TIMs) may be used to facilitate this process. In many cases a heat spreader in the form of a flat plate with high thermal conductivity may be placed between the chip and the lid.

Heat spreading is a very effective means to alleviate the need for sophisticated high-heat flux cooling options. Of course, the benefit of reducing the heat flux density by increasing the area should outweigh the "penalty" of the additional layer in the path of the heat stream. Figure 2.3 shows heat spreading results for $q = 150\,\mathrm{W/cm^2}$ as a function of thermal conductivity, thickness and heat transfer coefficient. For example, using an $8 \times 8\,\mathrm{cm^2}$ heat spreader of some advanced composite with $k = 800\,\mathrm{W/m\,K}$ and thickness of $\delta = 4\,\mathrm{mm}$ results in a temperature rise of about 40 K at a heat transfer coefficient $h = 2{,}500\,\mathrm{W/m^2\,K}$.

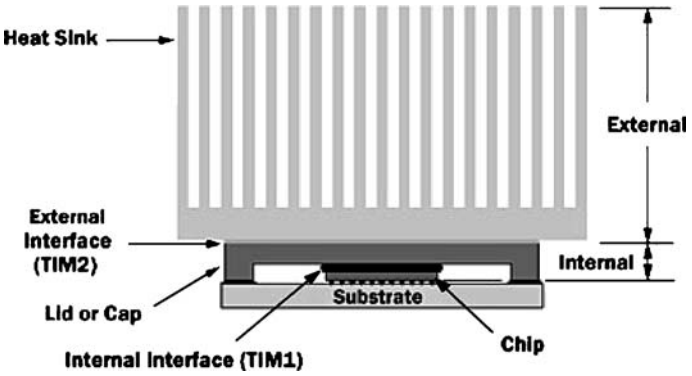

Fig. 2.2 Chip package with thermal conduction path to heat sink via TIMs. Reprinted from Lasance and Simons (2005) with permission

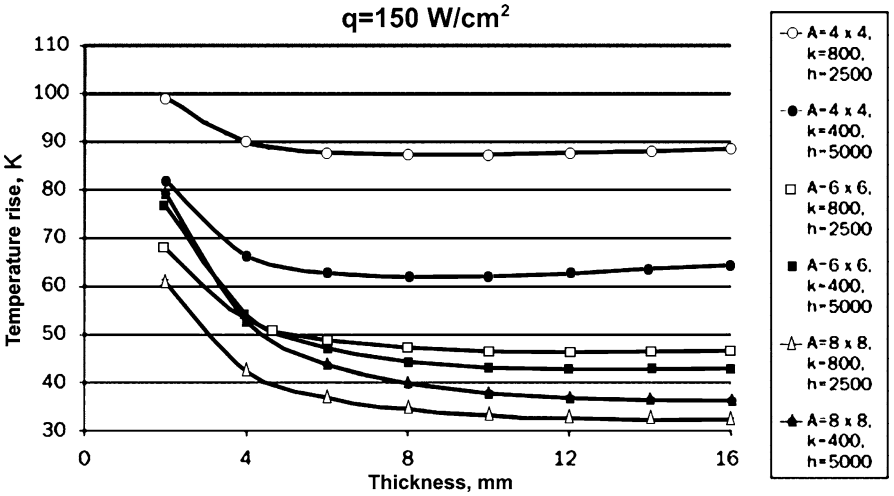

Fig. 2.3 Effect of thickness on heat spreading for different heat source areas, material thermal conductivities, and heat transfer coefficients (A in cm^2, k in $\mathrm{W/mK}$, h in $\mathrm{W/m^2K}$). Reprinted from Lasance and Simons (2005) with permission

Air cooling

It is generally acknowledged that traditional air-cooling techniques are about to reach their limit for high-power appliances. With standard fans a maximum heat transfer coefficient of about $150\,\mathrm{W/m^2\,K}$ can be reached with an acceptable noise level, which is about $1\,\mathrm{W/cm^2}$ for a $\Delta T = 60\,\mathrm{K}$ temperature difference. Using "macro-jet" impingement, theoretically we may reach $900\,\mathrm{W/m^2\,K}$, but with unacceptable noise levels. Non-standard fan/specialized heat sink combinations for CPU cooling are expected to have a maximum of about $q = 50\,\mathrm{W/cm^2}$. Recently,

some new initiatives have extended the useful range of air-cooling, such as piezo fans, "synthetic" jet cooling and "nanolightning."

Piezo fans

Piezoelectric fans are small, low-power, relatively low-noise, solid-state devices that provide viable thermal management solutions for a variety of portable electronic appliances, including laptop computers and cellular phones. In these fans piezoceramic patches are bonded onto thin, low-frequency flexible blades driven at resonance frequency, thereby creating an air stream directed at the electronics components. Thereby, up to 100% improvement over natural convective heat transfer can be achieved (Acikalin et al. 2004).

Synthetic jet cooling

An approach using periodic micro-jets called "synthetic jets" is still in the initial stages of study. Due to the pulsating nature of the flow, the jets create stronger entrainment than conventional steady jets with the same Reynolds number, and more vigorous mixing between the wall boundary layers and the rest of the flow. A test set-up is shown in Fig. 2.4. The jet entrains cool air from the environment, impinges on the top hot surface and returns the heated air to the environment. Radial current counter flow is created in the gap between the plates, with hot air dispersed along the top and the ambient air entrained along the bottom surface. The idea was further advanced by the development of flow actuators using micro-electromechanical systems (MEMS) technology (Beratlis and Smith 2003).

Nanolightning

An interesting new approach to increasing the heat transfer coefficient, known as "nanolightning," was also investigated. It is based on "micro-scale ion-driven airflow" using very strong electric fields created by nanotubes. As shown in Fig. 2.5, the ionized air molecules are moved by another electric field, thereby inducing secondary airflow (Peterson et al. 2003). Cooling at a heat flux level of $q = 40\,\mathrm{W/cm^2}$ has been reported.

Liquid cooling

Liquid cooling in electronics is generally divided into two main categories, indirect and direct, according to the type of contact between the coolant and the cooled components. The following sections discuss the two categories, represented by heat pipes and cold plates, and immersion cooling and jet impingement, respectively.

Heat pipes

Heat pipes are an enhanced means of transporting heat (in certain circumstances much better than copper) from a source to a heat sink where it can be transmit-

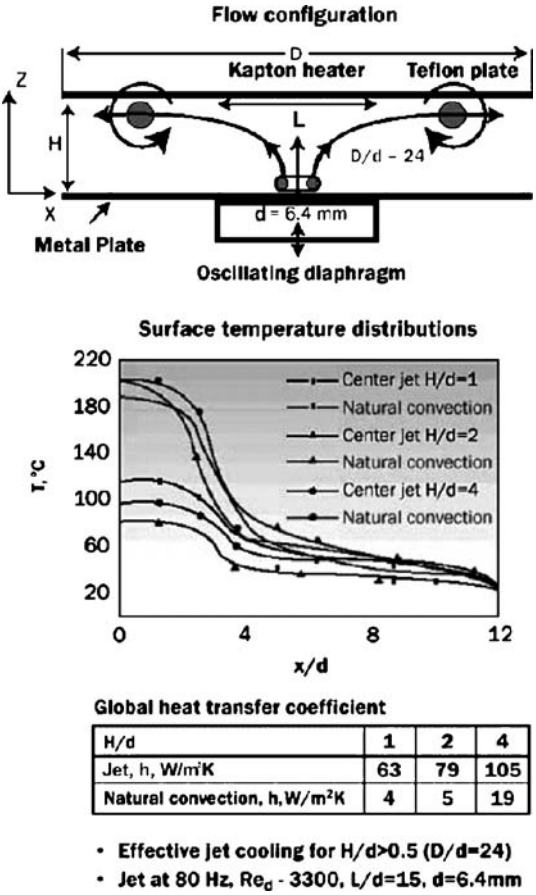

Fig. 2.4 Flow dynamics of normal jet impingement with an oscillating diaphragm. Reprinted from Lasance and Simons (2005) with permission

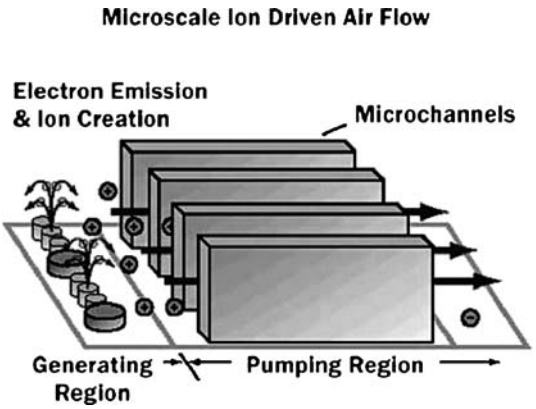

Fig. 2.5 Nanolightning sketch. Reprinted from Lasance and Simons (2005) with permission

ted to the cooling medium by natural or forced convection. They are sealed and vacuum-pumped vessels partially filled with liquid. Their internal walls are lined with a porous medium (the wick) that acts as a passive capillary pump. When heat is applied to one side of the pipe the liquid begins to vaporize. The pressure gradient causes the vapor to flow towards the cooler regions, where it condenses and is transported back by the wick structure, thereby closing the loop. Their performance scales from a heat flux of $10\,\mathrm{W/cm^2}$ to over $300\,\mathrm{W/cm^2}$. Loop heat pipes (LHP) have attracted increased attention. Their advantage over their conventional counterparts is that the vapor and liquid paths are separated, permitting much better performance of the liquid return loop. For example, Kim and Golliher (2002) showed the ability to accommodate a heat flux of $625\,\mathrm{W/cm^2}$.

Silicon micro-heat pipes (MHP) are passive systems used to transfer high heat fluxes and to increase the effective thermal conductivity of a Si substrate. Their working principle is based on two-phase heat transfer. A MHP consists of a noncircular closed channel, a few hundred micrometers wide and a few centimeters long. Similar to the preceding case, the liquid vaporizes at one end of the channel, where heat flux is applied (evaporator). The vapor, driven by the pressure gradient, flows to the other end of the channel, which is cooled (condenser). There it condenses and gives up its latent heat of vaporization. The capillary pressure difference between the evaporator and the condenser causes the liquid to flow back to the evaporator. Thereby, heat is transferred from the evaporator to the condenser by a continuous cycle of working fluid with a low thermal gradient. To increase the heat load, MHPs are implemented in arrays of several tens.

The role of a MHP is to reduce the maximum temperature of the wafer and decrease the temperature gradient across it, thereby increasing the effective thermal conductivity. Such a device was used in the study conducted by Le Berre et al. (2006). Its size was $20 \times 20\,\mathrm{mm^2}$ and consisted of a series of 27 parallel triangular channels, 500 μm wide and 350 μm deep (hydraulic diameter about 257 μm), micromachined into a silicon wafer using KOH anisotropic etching. The array volume was about $50\,\mathrm{mm^3}$, which represents a void fraction of 11%. Such a geometry with acute-angled corners is necessary for a proper heat pipe operation: the corners favor reduction of the meniscus curvature radius, which in turn increases the capillary pumping pressure.

The performances of the MHP array were evaluated for different methanol filling charges under different experimental conditions. The results indicated an increase in the effective thermal conductivity to about $200\,\mathrm{W/m\,K}$ under optimum conditions, equivalent to a 67% increase over an empty array. Performances are favored by reducing the input heat flux or increasing the cooling temperature.

Cold plates

Liquid-cooled cold plates perform a function analogous to that of air-cooled heat sinks. Unlike heat pipes, they may be considered active devices in that the liquid is usually forced through them by a pump.

Both direct and indirect liquid cooling methods can be further categorized as single-phase and two-phase methods. For example, jet impingement cooling may be a two-phase direct method, in contrast to the two-phase indirect technology of heat pipes and thermosiphons. Two-phase methods are preferable because of the high-heat transfer coefficients, although the systems tend to be more complex. In the mid-1980s, IBM employed an indirect liquid cooling technology using water for mainframes and supercomputers. This technology became the norm for high-performance computers, in which the large cold plates can be sufficiently separated from the electronics and thermally connected with the heat conduction devices. Two-phase cooling was not considered for notebook computers at that time, since most microprocessors were sufficiently cooled with metallic heat sinks and fans.

Immersion cooling

Direct liquid immersion cooling also provides a higher heat transfer coefficient, depending on the specific coolant and mode of convective heat transfer. Since there is no wall separating the heat source from the coolant, the heat can be removed directly from the chip. In these circumstances, consideration must be given to the coolant's chemical compatibility with the chip and other packaging materials exposed to the liquid. At present, with the continuous increase of heat flux at the chip level, microchannel cold plates are receiving renewed attention. The relative magnitude of the heat fluxes accommodated by liquid cooling depends on convective heat transfer processes classified as natural convection, forced convection, or boiling modes. The natural convection mode is derived from the mixing and fluid motion induced by density differences of the coolant. Its heat transfer rates are low and can be exceeded by forced convection mode in which the flow velocity of the liquid over the heated surface is increased with the aid of a pump. Boiling is a convective heat transfer process based on the phase change of the working fluid with vapor bubbles forming at the heated surface, and commonly has the form of pool boiling or flow boiling. The boiling curve (Fig. 2.6, Simons 1996) for a typical fluorocarbon coolant shows the

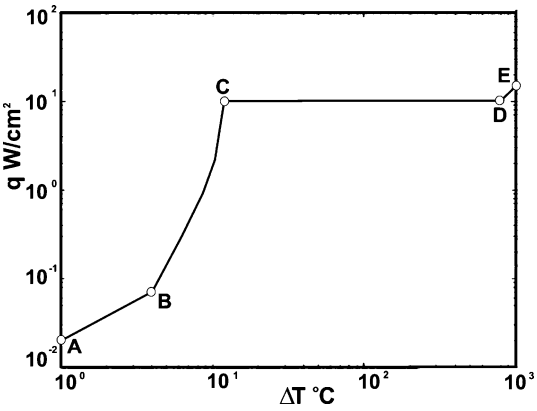

Fig. 2.6 Typical heat transfer regimes for immersion cooling with a fluorocarbon. Reprinted from Simons (1996) with permission

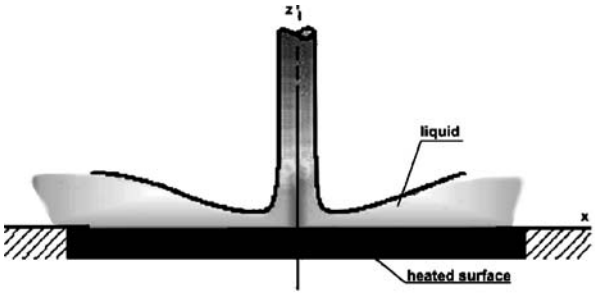

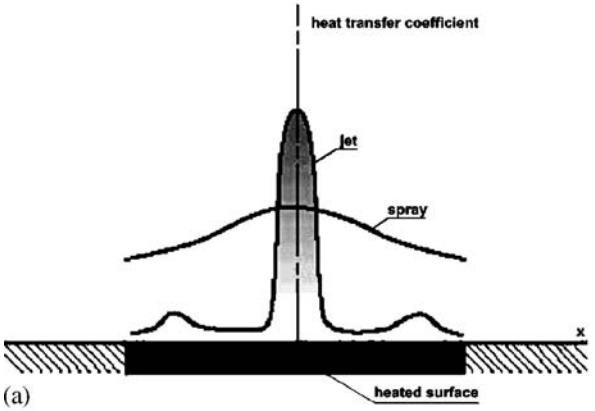

(a)

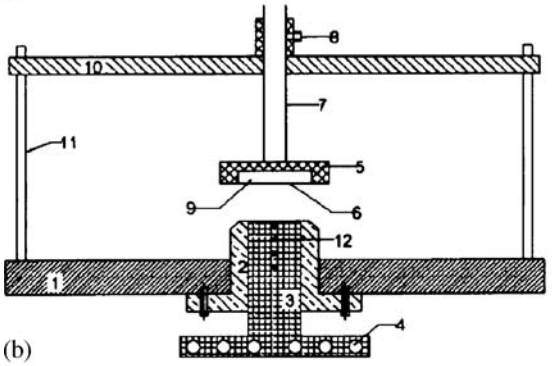

(b)

1 Stainless Steel Plate
2 Teflon Jacket
3 Copper Block
4 Cartridge Heater
5 Orifice Plate Support
6 Orifice Plate
7 Pipe
8 Vertical Position Set Screw
9 Distribution Chamber
10 Centering Flange
11Supporting Rod
12 Thermocouple
** 5 and 6 can be replaced by HAGO nozzle

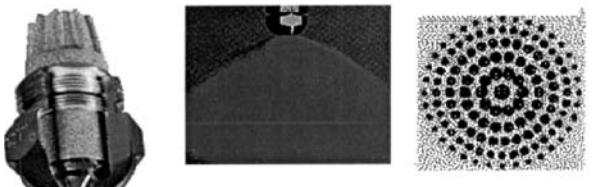

(c)

Fig. 2.7 (**a**) Spray and jet impingement cooling. Reprinted from Lasance and Simons (2005) with permission. (**b**) Details of the test section. (**c**) HAGO nozzle and spray details. Parts (**b–f**) reprinted from Fabbri et al. (2005) with permission

magnitude of heat fluxes as a function of excess temperature. At low chip powers, natural convection (A–B) initiates the heat transfer process until sufficient excess temperature is available to promote bubble growth on the surface, at which point boiling begins. As the power increases, more nucleation sites are activated and bubbles are detached at higher frequency, intensifying fluid circulation near the chip. This stretch between B and C is termed the nucleate boiling regime, where the intensified fluid circulation accommodates higher heat fluxes with minimal increase in the surface temperature. Line C–E represents nucleate boiling regime. Stretch D–E represents the transition to film boiling in which the heat transfer is realized by conduction through a vapor film. It is, however, very poor and may result in electronic failure due to the high temperatures. The most desirable mode for electronics cooling is the nucleate boiling regime. Immersion cooling is a well-established method, backed by over thirty years of university and industrial research. With natural convection two-phase flow, the critical heat flux using FC-72 is in the range of 5 to 20 W/cm^2. However, much higher heat fluxes up to 100 W/cm^2 can be accommodated through surface enhancement of the heat source.

Spray cooling and liquid jet impingement

Spray cooling and jet impingement (as shown in Fig. 2.7) are often considered as competing options for electronics cooling. In general, spraying requires lower flow rates but a higher nozzle pressure drop. In recent years spray cooling has received increasing attention as a means of supporting higher heat fluxes. In it the liquid is disintegrated into fine droplets that impinge individually on the heated wall. The cooling effect is achieved through a combination of thermal conduction through the liquid in contact with the surface, and vaporization at the liquid–vapor interface. The droplet impingement both enhances the spatial uniformity of heat removal and delays liquid separation at the wall during vigorous boiling.

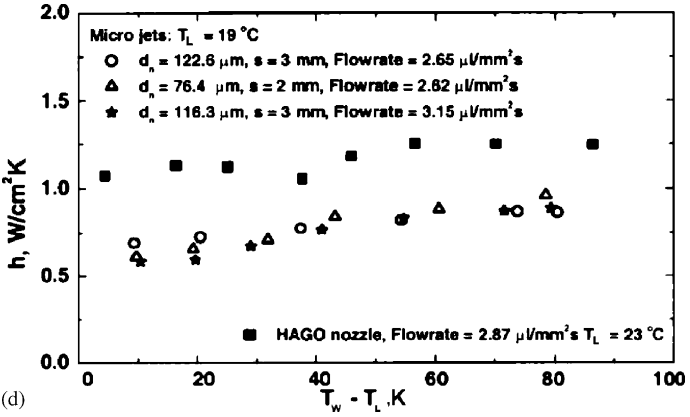

(d)

Fig. 2.7 (**d**) Comparison between spray and micro-jet performance for two flow rates 50.56 ml/min [2.87 μl/mm^2 s]. Parts (**b**–**f**) reprinted from Fabbri et al. (2005) with permission

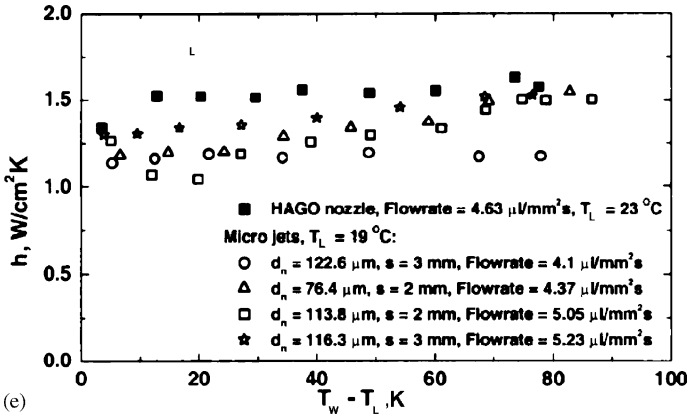

(e)

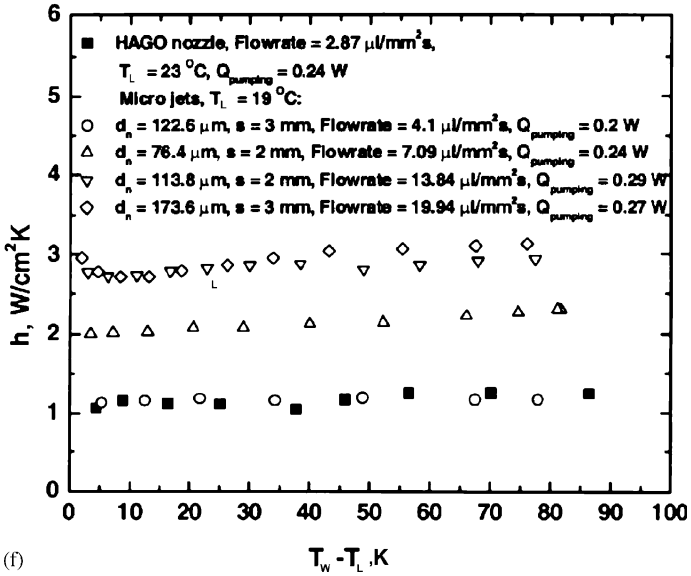

(f)

Fig. 2.7 (**e**) Comparison between spray and micro-jet performance for two flow rates 81.56 ml/min [4.63 μl/mm^{2}s]. (**f**) Comparison between spray and micro-jet performance for the same pumping power. Parts (**b–f**) reprinted from Fabbri et al. (2005) with permission

Single-phase heat transfer rates using droplet sprays and arrays of micro-jets have been compared by Fabbri et al. (2005). It was found that at a flow rate of 2.87 μl/mm^2 s spraying provides a higher heat transfer rate than any jet configuration, while at higher flow rate of 4.63 μl/mm^2 s jet arrays can perform as well as sprays.

Micro-jet arrays are usually associated with lower energy consumption rates than sprays generated by the special (HAGO) nozzle for the same flow rate. The liquid was pushed through a 0.5 mm stainless steel orifice plate to form the jets. The holes in the plate were laser drilled and were arranged in a circular pattern giving a radial

and circumferential pitch of 1 mm for 397 jets, 2 mm for 127 jets, and 3 for 61 jets. The results presented here are confined to this type of nozzle, although designs may exist involving lower pressure losses at the considered flow rates. For equal pumping power and $T_w - T_L = 76$ K, they can remove fluxes as high as 240 W/cm^2, while sprays can only handle 93 W/cm^2.

The pressure drop in the HAGO nozzle quickly reaches impractical values. There is always a combination of jet diameter and jet spacing that yields the same heat transfer coefficient as the spray, but at a much lower energy cost.

Liquid micro-jet arrays have been successfully put to use. The module has proved capable of dissipating 129 W, with a heat flux of 300 W/cm^2 at a surface temperature of 80 °C, a considerable achievement at the present state of the art. Reduction of the system pressure made for lower boiling inception temperatures, thus allowing for higher heat removal rates at lower surface temperatures.

Liquid metal cooling

High-electrical conducting fluids such as liquid metals offer a unique solution to current and future cooling needs of high-power density heat sources. The two principal advantages of single-phase cooling systems based on liquid metals lie in their superior thermophysical properties and in the feasibility of moving them efficiently with silent, non-moving pumps. Closed loops based on liquid metals and the requisite pumps make possible gravity-independent high-performance cooling systems. Analytical and experimental work has been presented, using miniature pumps operating at a greater than 8 kPa maximum pressure rise, and showing heat transfer coefficients on the order of 10 W/cm^2 K (Miner and Ghoshal 2004).

An example of a liquid cooling loop is shown in Fig. 2.8.

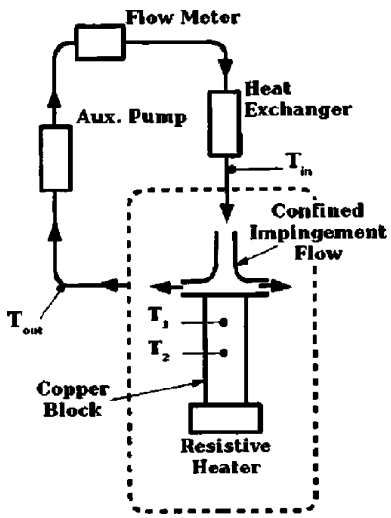

Fig. 2.8 Schematic representation of an experimental set-up for a liquid metal impingement/stagnation flow. Reprinted from Miner and Ghoshal (2004) with permission

Sintered porous inserts

The heat transfer and pressure drop in a rectangular channel with sintered porous inserts, made of stainless steels of different porosity, were investigated. The experimental set-up is shown in Fig. 2.9. Heat fluxes up to $6\,\mathrm{MW/m^2}$ were removed by using samples with a porosity of 32% and an average pore diameter of 20 µm. Under these experimental conditions, the temperature difference between the wall and the bulk water did not exceed $\Delta T = 55\,\mathrm{K}$ at a pressure drop of $\Delta P = 4.5$ bars (Hetsroni et al. 2006a).

Concept of micro-channel heat sink

For flow at a given rate, the only way to significantly increase the heat transfer coefficient is to reduce the channel size, whose optimum can be calculated assuming a practical limit on the available pressure. Recourse to multiple channels, instead of continuous coolant flow over the entire back substrate surface, enables one to multiply the substrate area by a factor φ, representing the total surface area of the channel walls which are in contact with fluid. Single-row micro-channels etched dir-

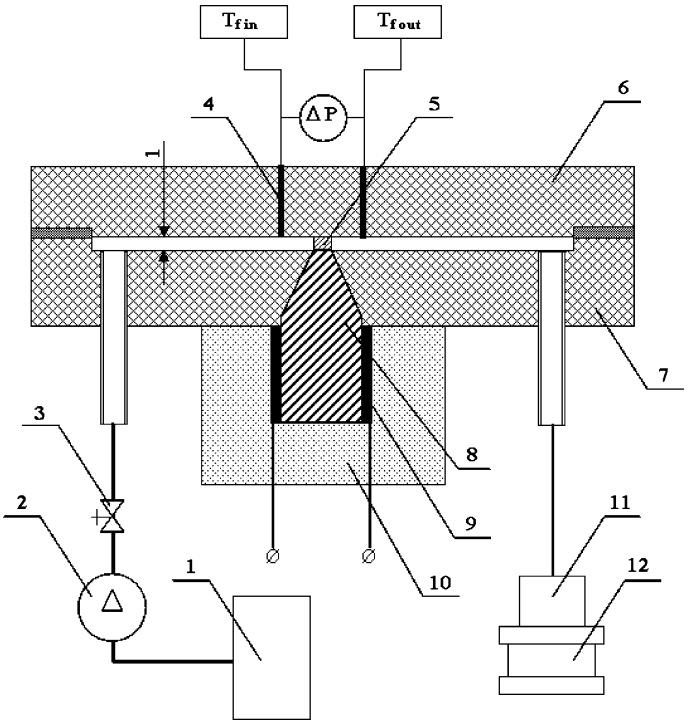

Fig. 2.9 Schematic diagram of experimental set-up: *1* inlet tank, *2* pump, *3* control valve, *4* temperature and pressure measurement ports, *5* sample of porous medium, *6* top of test section, *7* housing, *8* copper rod, *9* heater, *10* insulation, *11* exit tank, *12* electronic scales. Reprinted from Hetsroni et al. (2006a) with permission

ectly into the backs of silicon wafers were first shown to be effective by Tuckerman and Pease (1981) in which a maximum of $q = 790\,\mathrm{W/cm^2}$ was removed with a rise in water temperature $\Delta T = 71\,\mathrm{K}$ at water pressure $\Delta P = 2\,\mathrm{bar}$ (Fig. 2.10). The heat sink is made of deep rectangular channels of width w_c and depth H, separated by walls of thickness w_w. A cover plate is bonded onto the back, confining the coolant to the channels. The front surface of the substrate contains a planar heat source (the circuits).

The performance of a heat sink may be measured by its thermal resistance $R = \Delta T/q$, where ΔT is the temperature rise above that of the input coolant and q is the heat flux. As electronic and optical devices typically operate at a maximum $\Delta T_\mathrm{max} = 50{-}100\,\mathrm{K}$ above room temperature, their maximum power is determined by thermal resistance. In general, R is the sum of R_cond associated with conduction from the circuits through the substrate, package, and heat sink interface, R_conv with convection from the heat sink to the coolant, and R_heat with heating of the fluid as it absorbs the energy passing through the heat exchanger. To reduce R_cond, research into micro-scale heat exchangers has focused on heat sinks fabricated from a highly thermally conductive solid, such as copper or silicon, with rows of small channels fabricated into the surfaces. High solid conductivity is particularly important in multiple row structures, as the amount of heat by any given row can be large. A highly conductive medium increases heat conduction into subsequent layers where it can be transferred to the fluid. R_heat can be reduced by using a coolant of high volumetric heat capacity ρc_p. With these two components accounted for with relative ease, the convective thermal resistance R_conv becomes the dominant consideration in high-performance heat sinks. We focused on some aspects of single-phase and two-phase flow and heat transfer in small size channels.

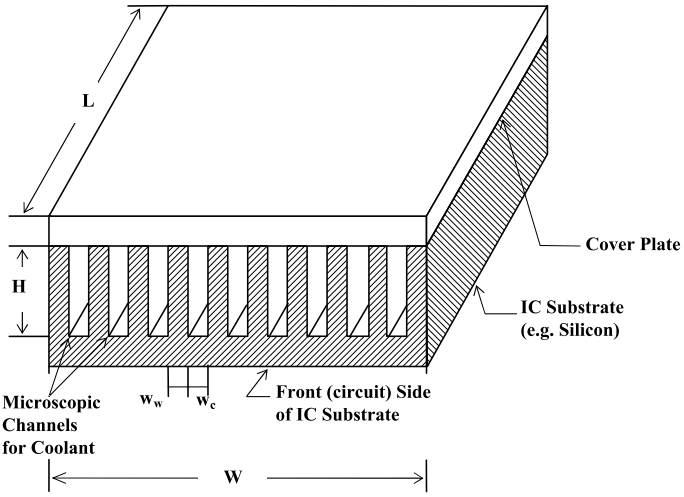

Fig. 2.10 High-performance micro-channel heat sink. Reprinted from Tuckerman and Pease (1981) with permission

Channel classification

The problems of micro-hydrodynamics were considered in different contexts: (1) drag at laminar, transient and turbulent single-phase flows; (2) heat transfer of liquids and gas flows; and (3) two-phase flows in adiabatic and heated micro-channels. As indicated by Kandlikar and Grande (2002), and by Hetsroni et al. (2005a, c), no fundamental change occurs in single-phase flow in the absence of rarefaction effects, which for gases are described by the Knudsen number, Kn, and are significant in the range $\mathrm{Kn} = 0.01-0.1$:

$$\mathrm{Kn} = \frac{\overline{\lambda}}{d_\mathrm{h}} \tag{2.1}$$

where $\overline{\lambda}$ is the mean free path for the gas:

$$\overline{\lambda} = \frac{\mu\sqrt{\pi}}{\rho\sqrt{2RT}} \tag{2.2}$$

with gas constant R in J/kg K, dynamic viscosity μ in kg/m s, density ρ in kg/m^3, temperature T in K.

The book by Karniadakis and Beskon (2002) addresses gas and liquid microflows with focus on the former, in which most of the deviations from macro-scales occur. The authors also treat liquid-specific phenomena and molecular dynamics.

Table 2.1 reproduced from the book by Karniadakis and Beskon, gives the mean free path for different gases at 300 K.

The classification in Table 2.2, based on the hydraulic diameter of the channel, was suggested by Kandlikar and Grande (2002).

The definition of mini-channels and micro-channels has not been clearly and strictly established in the literature although many related studies have been done. For example, for compact heat exchangers, Mehendale et al. (1999) gave a relatively

Table 2.1 Mean free path for gases at atmospheric pressure

Gas	T K	R J/kg K	ρ kg/m^3	μ kg/m s	$\overline{\lambda}$ μm
Air	300	287.0	1.1614	1.85×10^{-5}	0.068
Helium	300	2077	0.1625	1.99×10^{-5}	0.194
Hydrogen	300	4124	0.08078	8.96×10^{-6}	0.125
Nitrogen	300	296.8	1.1233	1.78×10^{-5}	0.066

Table 2.2 Channel classification

Conventional channels	$d_\mathrm{h} > 3$ mm
Mini-channels	200 μm $\le d_\mathrm{h} \le 3$ mm
Micro-channels	10 μm $\le d_\mathrm{h} \le 200$ μm
Transitional channels	0.1 μm $\le d_\mathrm{h} \le 10$ μm
Molecular nanochannels	$d_\mathrm{h} \le 0.1$ μm

loose definition of mini-channels, in terms of hydraulic diameter: $d_h = 1-6$ mm. In this book we will consider the channels with hydraulic diameters ranging roughly from 5 to 500 μm as micro-channels and the channels with hydraulic diameters $d_h > 500$ μm as conventional size channels. Traditional correlations may not be suitable to predict flow regimes, pressure drop and heat transfer in micro-channels and applicability of existing correlations for conventional size channels to micro-channels should be carefully examined.

Classification on the basis of the Knudsen number, as per Karniadakis and Beskon (2002), is given in Table 2.3.

The micro-electromechanical systems (MEMS) operate in a wide range of regimes covering continuum, slip and transition flows. Further miniaturization of the MEMS device components and appliances in the emerging field of nanoelectromechanical systems (NEMS) would result in high Knudsen numbers, making it necessary to study mass, momentum, and energy transport over the entire Knudsen range.

The overall performance of micro-channel heat sinks

Micro-channel heat sinks are devices that provide liquid flow through parallel channels having a hydraulic diameter of around 5–500 μm. Figure 2.11 shows the range of heat transfer coefficients attainable with different fluids and cooling schemes (Mudawar 2001). Air is the most readily available, and remains the most widely used coolant for most applications. However, its poor thermal transport properties limit its use to low-heat flux devices. Better results are obtained with fluorochemical liquids, and the most demanding cooling situations are typically managed with water.

Mudawar (2001) reviewed high-heat flux thermal management schemes, including ultra high-heat fluxes in the range of 1,000–100,000 W/cm^2. Garimella and Sobhan (2003) reviewed research on fluid dynamics and heat transfer in micro-channels up to 2000. Recent overviews were also provided by Morini (2004), Mohapatra and Loikitis (2005), Hetsroni et al. (2005a, 2006c), Thome (2006), and Cheng and Wu (2006).

A micro-channel heat sink can be classified as single-phase or two-phase according to the state of the coolant inside it. For single-phase fluid flow in smooth

Table 2.3 Classification on the basis of the Knudsen number

Range of Knudsen number	Type of flow
$Kn = 0.001-0.1$	Continuum flow: no rarefaction effects
$Kn = 0.01-0.1$	Slip flow: rarefaction effects that can be modeled with a modified continuum theory with wall slip taken into consideration
$Kn = 0.1-10$	Transition flow: between slip flow and free molecular flow, treated statistically, e.g., by the Boltzmann equation
$Kn > 10$	Free molecular flow: motion of individual molecules, that must be modeled and then treated statistically

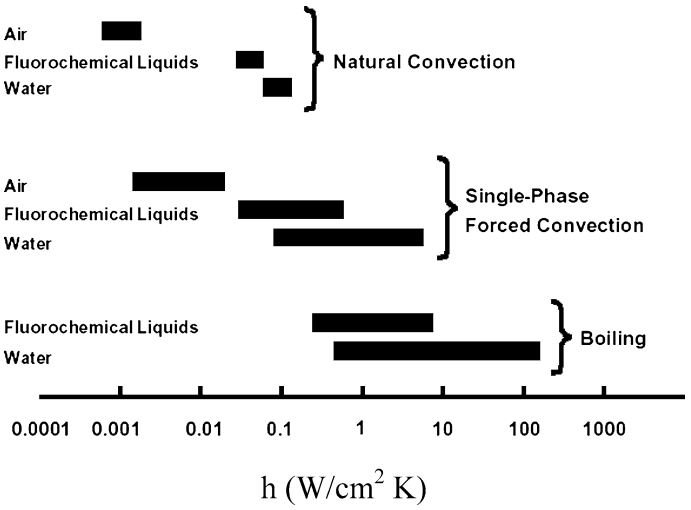

Fig. 2.11 Heat transfer coefficient for different coolants. Reprinted from Mudawar (2001) with permission

channels with a hydraulic diameter d_h from 15 to 4,000 μm, in the Reynolds number range $Re < Re_{crit}$, the Poiseuille number Po is independent of Re. For single-phase gas flow in channels with a hydraulic diameter from 100 to 4,000 μm, in the range $Re < Re_{crit}$, with Knudsen number $0.001 \leq Kn \leq 0.38$, and Mach number $0.07 \leq Ma \leq 0.84$, the experimental friction factor agrees quite well with the theoretical prediction for fully developed laminar flow. The behavior of single-phase flow in micro-channels shows no differences from macro-scale flow (Hetsroni et al. 2005a).

By contrast, two-phase flow in micro-channels of rectangular, circular, triangular, or trapezoidal cross-section showed significant differences when compared to macro-scale flow. Lee et al. (2004) studied the bubble growth dynamics in single micro-channels as small as 41.3 μm. They concluded that a conventional bubble departure model for convective boiling in conventional tubes larger than 6 mm cannot predict the growth pattern, and that the bubbles always nucleate from the corners. Chung and Kawaji (2004) investigated liquid and gas adiabatic two-phase flow in micro-capillaries of circular and square cross-sections and found that the transition of flow patterns occurred at lower surface velocities in the circular capillary than in the square one. Convective boiling in transparent single micro-channels with similar hydraulic diameters but different cross-sections was studied by Yen et al. (2006). Two types of glass micro-channels were tested: circular of $d = 210$ μm, and square of $d_h = 214$ μm. In the latter, the corners acted as active nucleation cavities, both the number of nucleation bubbles and the local heat transfer coefficient increased with decreasing vapor quality. The performance of a micro-channel heat sink is enhanced by increasing the heat transfer area and coefficient, the first being achieved by increasing the number of micro-channels and the second by reducing the hydraulic diameter, which makes for a dramatic increase in pressure drop. Calame et al. (2007)

carried out experiments on removing high heat flux from GaN-on-Sic semiconductors dies using micro-channels coolers. A wide variety of micro-channel materials and configurations were investigated. Silicon micro-channel coolers exhibited good performance at power densities of 1,000–1,200 W/cm^2. Polycrystalline chemical vapor deposited (CVD) Sic micro-channel coolers were found to be promising for higher power densities of 3,000–4,000 W/cm^2. The performance was good as a copper micro-channel cooler, but presumably without the stress problems associated with differential thermal expansion between the semiconductor and cooper.

Lee and Vafai (1999) compared jet impingement and micro-channel cooling for high-heat flux appliances. One of their conclusions is that micro-channel cooling is more effective for areas smaller than $7 \times 7\,cm^2$. Kandlikar and Upadhye (2005) showed enhanced micro-channel cooling by using off-set strip fins and a split-flow arrangement. Colgan et al. (2005) published a practical implementation of a silicon micro-channel cooler (shown in Fig. 2.12) for high-power chips. They argued that given the high cost of high-performance processor chips it is impractical to form the micro-channels directly on the chip. Instead, a separate micro-channel cold plate is bonded to the back of the chip, a design requiring very low interface thermal resistance. If the micro-cooler is based on silicon, rigid bonding dictates use of silver-filled epoxies or solder. Power densities in excess of 400 W/cm^2 are reported, for a flow of 1.2 l/min at 30 kPa.

Micro-channel heat transfer can be pushed even further by recourse to boiling. In addition to offering higher heat transfer coefficients, boiling convection in micro-channels is promising because it requires less pumping power than its single-phase liquid counterpart to achieve a given heat sink thermal resistance. For the same heat flux the pressure drops by a factor of 20. A review on boiling and evaporation in small-diameter channels was published by Bergles et al. (2003).

The vapor–liquid exchange process that is largely responsible for the effectiveness of phase-change cooling, requires uninterrupted liquid flow on the device surface. Higher heat fluxes are dissipated by a higher output of vapor bubbles per unit surface area. Unfortunately, bubble crowding may lead to significant vapor coalescence, eventually interfering with the liquid access to the device surface. Once the vapor–liquid exchange process is interrupted, the power dissipated in the device it-

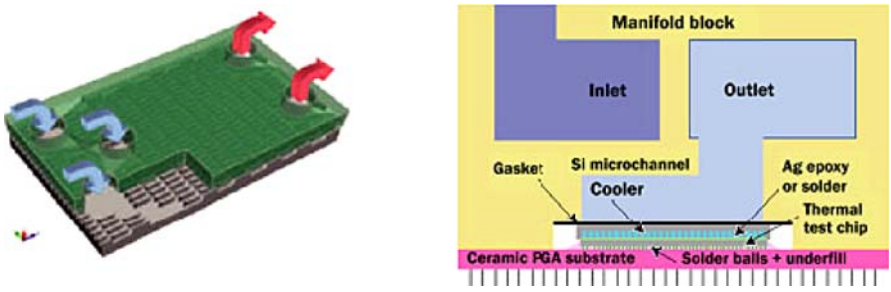

Fig. 2.12 Pictures from IBM paper showing high-performance liquid cooling technology using micro-channels. Reprinted from Colgan et al. (2005) with permission

Table 2.4 Comparison of pressure drops between PG 50% and water for the same thermal resistance

Liquid	Flow rate (ml/min)	Pressure drop (kPa)
Water	200	80
PG 50%	220	900

self will no longer be removed and the device temperature begins to escalate out of control. This is the highest point in the boiling curve, termed the critical heat flux (CHF), constituting the upper design limit for any phase-change cooling system.

The main problem in single-phase micro-channel cooling are freezing thresholds required in the electronics industry, which may be as low as 40 °C, in which case water is ruled out as cooling medium. Table 2.4 shows a comparison between the performance of the widely used propylene glycol antifreeze (1:1 PG and water) versus pure water for the same thermal performance. The micro-channel size for this study is $50 \times 300\,\mu m$ (Prasher et al. 2005). It is seen that the pressure drop for conventional antifreeze is very large due to its low thermal conductivity and high viscosity. As a result, strong forces act on the pump bearings. Therefore, for single-phase micro-channel cooling, other antifreeze coolants are needed, with high-thermal conductivity and low viscosity.

Another major problem in this context is that the coolant also has to be used as lubricant for pump bearings, as the pump has to be hermetically sealed. This creates a situation of conflicting requirements: high viscosity from lubrication viewpoint, low viscosity from pressure drop viewpoint. Figure 2.13 shows the thermal performance of the package-based micro-channel cold plate as a function of the pressure drop (Prasher et al. 2005). It can be seen that reducing the thermal resistance of the micro-channels will result in a large pressure drop. In turn, this large pressure

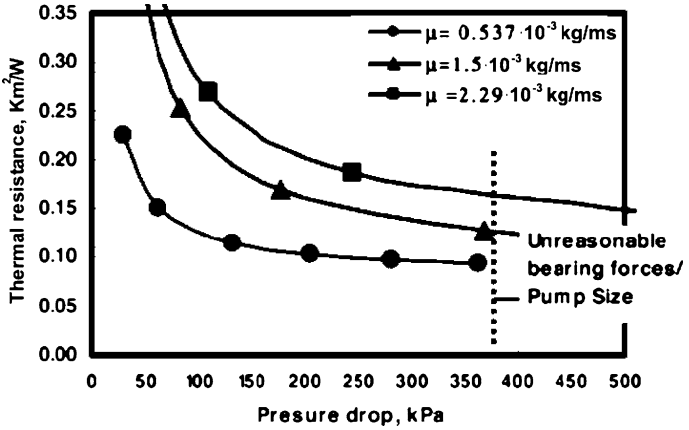

Fig. 2.13 Thermal resistance vs. pressure drop for fluids with different viscosity. Reprinted from Prasher et al. (2005) with permission

Table 2.5 Saturation thermophysical properties of some liquid coolants at 1 bar

Fluid	Saturation temperature T_{sat} [°C]	Liquid density ρ_L [kg/m^3]	Liquid specific heat $c_{p,L}$ [J/kg K]	Vapor density ρ_G [kg/m^3]	Latent heat of vaporization h_{LG} [kJ/kg]	Surface tension $\sigma \times 10^3$ [N/m]
FC-72	56.6	1600.1	1102.0	13.43	94.8	8.35
FC-87	3.0	1595.0	1060.0	13.65	87.93	14.53
PF-5052	50.0	1643.2	936.3	11.98	104.7	13.00
Water	100.0	957.9	4217.0	0.60	2256.7	58.91

drop across the device will generate significantly large forces on the bearings, thus increasing the wear and possibly reducing the life time of the pumps. In addition, the low physical size of the pump shaft may impose significant additional challenges on the bearing design.

Phase-change cooling systems make do with smaller sizes without necessarily imposing a larger pumping power requirement compared with single-phase systems.

The saturation thermophysical properties of some liquid coolants are presented in Table 2.5 (Mudawar 2001).

Poor flow distributions may result in localized dry hotspots which, absent control of the temperature fluctuations, may cause rapid overheating. Temperature and pressure fluctuations, and poor flow distribution, are the main problems that accompany the use of two-phase micro-channels.

2.2 Pressure and Temperature Measurements

Pressure measurement

Until recently pressures and temperatures were not measured directly inside the micro-channels because of size limitations. To obtain the channel inlet and exit pressures, measurements were taken in a plenum or supply line prior to entering the channel. Special coefficients were sometimes assumed to account for losses at the ends and in any piping between the channel plenums and the pressure transducers. In attempts to obviate the need for such assumptions experiments were conducted on integration of pressure sensors with a micro-channel, allowing the static pressure inside it to be measured at multiple locations. These early experiments involved either surface micro-machined channels with channel heights on the order of 1–2 μm (Shih et al. 1996; Li et al. 2000), or of conventionally machined channels, which are typically larger than $d_h = 250$ mm (Pfund et al. 2000). Due to the difficulty of getting integrated sensors to operate properly and the limited range of channel dimensions tested, the experiments provided little additional information about micro-channel flows at Kn < 0.01. As a further step Kohl et al. (2005), using micro-fabrication technologies, restored the integration of tap lines and pressure sensing membranes

into a system consisting of three silicon chips (Fig. 2.14). The micro-channel was fabricated by etching silicon wafers in KOH, producing a rectangular cross-section.

The lower chip contains the micro-channel test section with inlet and exit plenums, eight static pressure tap lines intersecting the micro-channel at equally spaced intervals, and one tap line per plenum. The tap line to the micro-channel

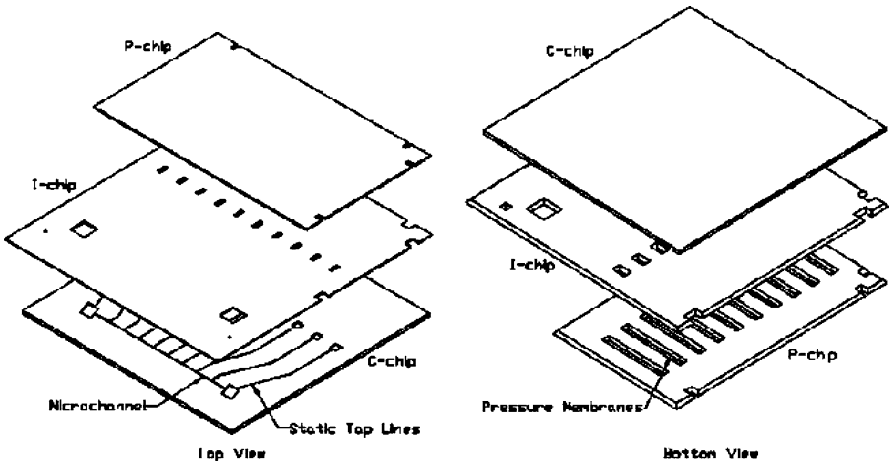

Fig. 2.14 Micro-fabricated test section components, *top* and *bottom* views. Reprinted from Kohl et al. (2005) with permission

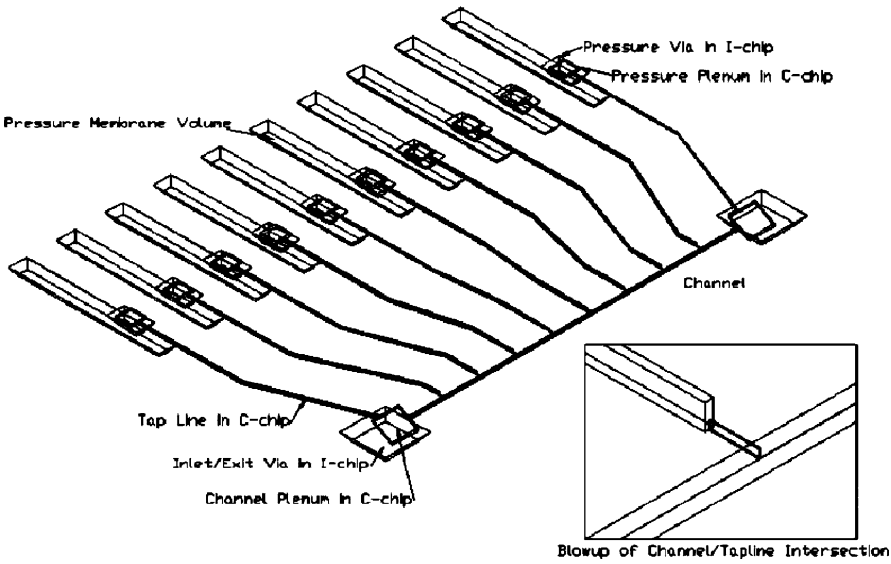

Fig. 2.15 Fluid-filled volume of the micro-channel system showing the connections between the micro-channel, static tap lines, and the fluid-filled volume of the pressure sensors. Reprinted from Kohl et al. (2005) with permission

intersection is etched by a deep silicon RIE process to a width less than 7 μm and depths on the order of 10 μm. The middle chip is used to seal the channel and tap lines and provides ports for introducing and removing fluid from the plenums, as well as for connecting the tap lines to the pressure membrane chip, which is located at the top. The pressure membrane chip contains 10 rectangular membranes for sensing pressure from the tap lines. The membranes are KOH etched out of silicon wafers and are approximately 0.564 mm wide, 10 mm long, and 50 μm thick. Figure 2.15 is a schematic of the fluid-filled volume of the micro-channel and system including the tap lines and pressure sensor volumes.

The investigation shows agreement between the standard laminar incompressible flow predictions and the measured results for water. Based on these observations the predictions based on the analytical results of Shah and London (1978) can be used to predict the pressure drop for water in channels with d_h as small as 24.9 μm. This investigation shows also that it is insufficient to assume that the friction factor for laminar compressible flow can be determined by means of the well-known analytical predictions for its incompressible counterpart. In fact, the experimental and numerical results both show that the friction factor increases for compressible flows as Re is increased for a given channel with air.

Temperature measurements

Reliable micro-scale measurement and control of the temperature are required in developing thermal micro-devices. Available measurement techniques can be largely classified into contact and non-contact groups. While the resistance thermometer, thermocouples, thermodiodes, and thermotransistors measure temperature at specific points in contact with them, infrared thermography, thermochromic liquid crystals (TLC), and temperature-sensitive fluorescent dyes cover the whole temperature field (Yoo 2006).

Resistance thermometry

Resistance thermometry, based on the variation of the resistance with temperature, is one of the most traditional techniques used for temperature measurement in the micro-scale. It is stable and applicable to a wide range of temperatures, but subject to inaccuracies due to self-heating since it involves use of electric current. The resistance temperature detector (RTD) and thermistor are the most frequently used forms. Polysilicon microthermistors have been used to study the heat transfer characteristics in micro-channels (Jiang et al. 1999a,b, 2000) and applied to the wall shear stress measurement (Lin et al. 2000). Resistance thermometry is also applied in thermocapillary pumping systems (Sammarco and Burns 1999), micro-machined chips (Yoon et al. 2002), and transient temperature measurement in thermal bubble formation (Tsai and Lin 2002). It requires carefully controlled fabrication including sensor materials of high purity, precise control of the dosage, and calibration of the sensors. In the latter, one should bear in mind that all components can be temperature-dependent.

Thermocouples

A thermocouple is one of the most common temperature sensors – inexpensive, reliable, interchangeable, and covering a wide range of temperature. For reduced size and improved spatial resolution, the micro-machined thermocouple attached to a cantilever-based probe tip such as in atomic force microscopy (AFM) has been developed. This technique, which is called scanning thermal microscopy (STM), generates a thermal map simultaneously with a topographical map by scanning the thermoelectric voltage on the surface. The spatial resolution of the technique has been reduced down to 24 nm (Luo et al. 1997). Significant improvements on the STM technique and its applications have been reviewed in detail by Majumdar (1999). Varesi and Majumdar (1998) reported a new technique called scanning joule expansion microscopy (SJEM) that could simultaneously image surface topography and material expansion due to joule heating.

Thermochromic liquid crystal

In the thermochromic liquid crystal (TLC) the dominant reflected wavelength is temperature-dependent and it has been employed for full-field mapping of temperature fields for over three decades. Although it is non-intrusive and cost effective, there are some problems in applying it to micro-scale measurements, because of size (typically tens of micrometers) and time response (from a few milliseconds to several hundred milliseconds depending on the material and the form). Examples of application are micro-fabricated systems (Chaudhari et al. 1998; Liu et al. 2002) and electronic components (Azar et al. 1991).

The liquid crystal thermographs method has been used for measuring microtube surface temperature with uncertainties of lower than ± 0.4 K by Lin and Yang (2007). The average outside diameter micro-tubes was 250 μm and 1,260 μm, respectively. The surface was coated with thermochromic liquid crystal (TLC). The diameters of encapsulated TLC were ranging from 5 to 15 μm. The TLC was painted on the tested tubes surface with thickness of approximately 30 μm.

Laser-induced fluorescence

Fluorescence is the capacity of certain molecules to absorb energy at a particular wavelength and to reemit it at a longer wavelength, in the range of visible light. Examples of relevant studies are Kim and Kihm (2001), and Ross et al. (2001).

Infrared thermography

Infrared (IR) thermography is one of the most advanced non-destructive (NDT) methods based on the fact that all bodies whose absolute temperature is above zero emit electromagnetic radiation over a wide spectrum of wavelengths depending on the temperature. Recently, several researchers have applied it to micro-scale temperature measurement. Hetsroni et al. (2001a) constructed a thermal micro-system

and studied the effect of the geometric configuration on the flow and heat transfer. Using a flow visualization system, they observed that the heat transfer was enhanced under conditions of flow boiling. Subsequently, more detailed investigations regarding boiling in capillary tubes have been conducted (Hetsroni et al. 2003a,b). IR thermography was also used to confirm formation of thermally isolated integral micro-hotplates, which is the key element in the development of an array of micropilasters and conductivity-type gas sensors (Furjes et al. 2002). In the case of liquids, a problem is that the temperature is measured on the basis of the radiation emitted from an object, which means that it is necessary to know the accurate value of the emissivity, which in liquids is sensitive to the wavelength in the infrared range.

Mishan et al. (2007) developed an infrared technique to measure the temperature of the fluid and wall in a micro-channel, using a transparent cover made of sapphire glass with a wavelength range of 0.15 to 7 μm, thus permitting visual observation. When radiant energy strikes a surface, a part of the radiation is reflected, a part is absorbed and a part is transmitted. The transmission of the sapphire window with a thickness of 10 mm is shown in Fig. 2.16. From this figure one can conclude that the transmission is constant for most of the wavelength range, and for $\lambda = 5\,\mu\text{m}$ and $T = 273\,\text{K}$, it equals about 85%, a suitable value for the IR technique. The measurements were preceded by calibration, with the temperature of the water flowing into the manifolds (range 30 to 90 °C) measured by a thermocouple and IR camera with $\pm 1\,\text{K}$ accuracy.

The IR technique also yielded temperature distributions (Fig. 2.17) in the symmetry plane at $\text{Re} = 30$ and $q = 19 \times 10^4\,\text{W/m}^2$. The wall temperature decreases by axial conduction through the solid walls in the last part of the micro-channel ($x/L > 0.75$) since this part is not heated. Neither the wall nor the fluid bulk temperature distribution can be approximated as linear.

The temperature distribution depends on the material and design of the module, the flow rate, and the heat flux. Figure 2.18a shows the IR image (top view) of the central part of the test module obtained at $\text{Re} = 100$ and $q = 25 \times 10^4\,\text{W/m}^2$, and Fig. 2.18b shows its counterpart in the spanwise direction. The field of view is

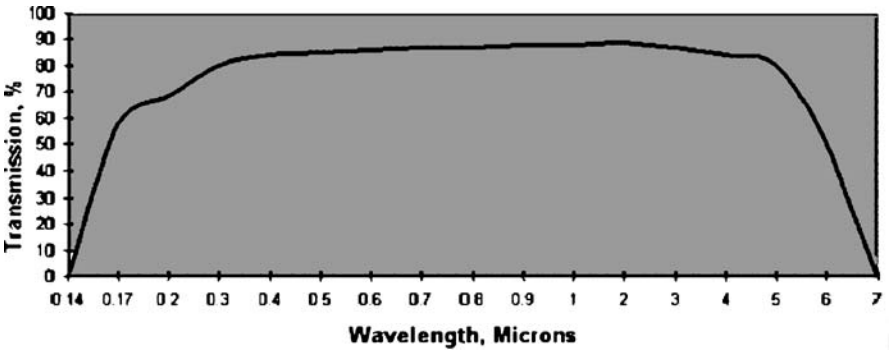

Fig. 2.16 Transmission vs. wavelength at 10 mm thick sapphire glass. Reprinted from Mishan et al. (2007) with permission

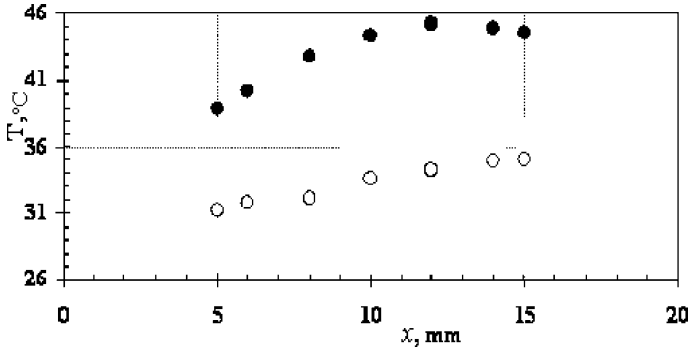

Fig. 2.17 Temperature distribution in the streamwise direction. The *solid circles* (•) represent the bottom temperature, and the *empty circles* (○) represent the fluid temperature. Reprinted from Mishan et al. (2007) with permission

3.6 mm and 3.6 mm in the streamwise and spanwise direction, respectively, the gray strips refer to the temperature on the channel walls (about 31.2 °C), the black strips to that of the water (about 29.9 °C).

Uncertainty in experimental measurements

For each result presented, the experimental data should include the following information:

1. The precision limit P. The $\pm P$ interval about a nominal result (single or average) is the region, with 95% confidence, within which the mean of many such results would fall, if the experiment were repeated under the same conditions using the same equipment. Thus, the precision limit is an estimate of the lack of repeatability caused by random errors and unsteadiness.
2. The bias limit B. The bias limit is an estimate of the constant error. It is assigned with the understanding that the true value of the bias error, if known, would be less than $|B|$ with 95% confidence.
3. The uncertainty U. The $\pm U$ interval about the nominal result is the band within which true value of the result lies with 95% confidence. It is calculated from

$$U = [B^2 + P^2]^{1/2} \tag{2.3}$$

Example

Consider an experiment in which an air-cooled device is being tested and it is desired to determine the rate of heat transfer Q to the cooling air (ASME 2000). This can be accomplished by measuring the mass flow rate m, and the inlet and outlet air temperatures, T_{in} and T_{out}, and computing:

$$Q = mc_{\text{p}}(T_{\text{out}} - T_{\text{in}}) \tag{2.4}$$

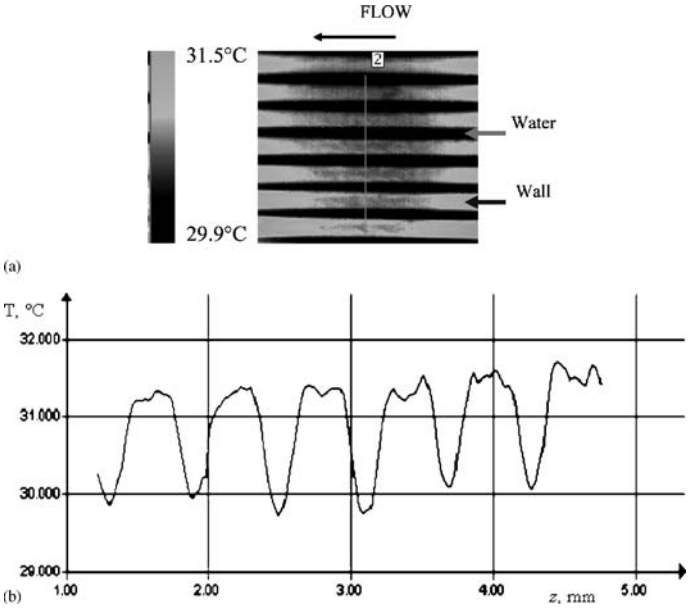

Fig. 2.18a,b Top view of the temperature field, Re = 100, $q = 25 \times 10^4$ W/m^2. (**a**) IR image. (**b**) Temperature variation in the spanwise direction. Reprinted from Mishan et al. (2007) with permission

where Q is the heat rate, c_p is the constant-pressure specific heat of air, and m is the mass flow rate in kg/s.

The 95% confidence uncertainty U_Q in the experimental result Q, is given by the following combination of the precision (random) contribution P_Q, and the bias contribution B_Q:

$$U_Q = \sqrt{P_Q^2 + B_Q^2} \tag{2.5}$$

These two contributions can be evaluated separately in terms of the sensitivity coefficients of the result to the measured quantities by using the propagation equation of Kline and McClintock (1953):

$$P_Q^2 = \left(\frac{\partial Q}{\partial m}\right)^2 P_m^2 + \left(\frac{\partial Q}{\partial c_\mathrm{p}}\right)^2 P_{c_\mathrm{p}}^2 + \left(\frac{\partial Q}{\partial T_\mathrm{out}}\right)^2 P_{T_\mathrm{out}}^2 + \left(\frac{\partial Q}{\partial T_\mathrm{in}}\right)^2 P_{T_\mathrm{in}}^2 \tag{2.6}$$

and

$$\begin{aligned} B_Q^2 = &\left(\frac{\partial Q}{\partial m}\right)^2 B_m^2 + \left(\frac{\partial Q}{\partial c_\mathrm{p}}\right)^2 B_{c_\mathrm{p}}^2 + \left(\frac{\partial Q}{\partial T_\mathrm{out}}\right)^2 B_{T_\mathrm{out}}^2 \\ &+ \left(\frac{\partial Q}{\partial T_\mathrm{in}}\right)^2 B_{T_\mathrm{in}}^2 + 2\left(\frac{\partial Q}{\partial T_\mathrm{out}}\right)\left(\frac{\partial Q}{\partial T_\mathrm{in}}\right) B'_{T_\mathrm{out}} B'_{T_\mathrm{in}} \end{aligned} \tag{2.7}$$

where $B'_{T_{\text{out}}}$ and $B'_{T_{\text{in}}}$ are the combination of $B_{T_{\text{out}}}$ and $B_{T_{\text{in}}}$, which arise from identical error sources (as in the case of the thermocouples calibrated using the same standards, equipment, and procedures), and are therefore presumed to be perfectly correlated.

Using Eq. (2.4) to evaluate the derivatives, denoting $\Delta T = T_{\text{out}} - T_{\text{in}}$ and rearranging, one obtains

$$\left(\frac{P_Q}{Q}\right)^2 = \left(\frac{P_m}{m}\right)^2 + \left(\frac{P_{c_{\text{p}}}}{c_{\text{p}}}\right)^2 + \left(\frac{P_{T_{\text{out}}}}{\Delta T}\right)^2 + \left(\frac{P_{T_{\text{in}}}}{\Delta T}\right)^2 \tag{2.8}$$

and

$$\left(\frac{B_Q}{Q}\right)^2 = \left(\frac{B_m}{m}\right)^2 + \left(\frac{B_{c_{\text{p}}}}{c_{\text{p}}}\right)^2 + \left(\frac{B_{T_{\text{out}}}}{\Delta T}\right)^2 + \left(\frac{B_{T_{\text{in}}}}{\Delta T}\right)^2 + 2\left(\frac{B'_{T_{\text{out}}}}{\Delta T}\right)\left(\frac{B'_{T_{\text{in}}}}{\Delta T}\right). \tag{2.9}$$

These derivatives can be evaluated numerically, using a data reduction program, or analytically.

In Eq. (2.4) the temperatures T_{out} and T_{in}, denote the bulk mean air temperatures at the outlet and inlet cross-sections, respectively. Their representation by point measurements introduces a bias error equal to the difference between the latter and the corresponding bulk means. In evaluating it, allowance should be made for the residual uncertainty involved in the bias errors from the probe calibration, etc.

Consider now a situation in which the bias limits in the temperature measurements are uncorrelated and are estimated as 0.5 °C, and the bias limit on the specific heat value is 0.5%. The estimated bias error of the mass flow meter system is specified as "0.25% of reading from 10 to 90% of full scale." According to the manufacturer, this is a fixed error estimate (it cannot be reduced by taking the average of multiple readings and is, thus, a true bias error), and B_m is taken as 0.0025 times the value of m. For $\Delta T = 20\,^{\circ}\text{C}$, Eq. (2.9) gives:

$$\frac{B_Q}{Q} = \sqrt{(0.0025)^2 + (0.005)^2 + \left(\frac{0.5\,^{\circ}\text{C}}{20\,^{\circ}\text{C}}\right)^2 + \left(\frac{0.5\,^{\circ}\text{C}}{20\,^{\circ}\text{C}}\right)^2} = 0.036 (= 3.6\%). \tag{2.10}$$

Obviously, the bias limits on the temperature measurements are dominant in this specific case. When they are totally correlated, the last term in Eq. (2.9) cancels out the third and fourth terms, and B_Q/Q equals 0.0056 instead if 0.036.

If the random errors and process unsteadiness are such that the precision limit for Q, P_Q, calculated from Eq. (2.7), is 2.7%, the overall uncertainty in the determination of Q, U_Q, is:

$$\frac{U_Q}{Q} = \sqrt{\left(\frac{B_Q}{Q}\right)^2 + \left(\frac{P_Q}{Q}\right)^2} = \sqrt{(0.036)^2 + (0.027)^2} = 0.045 (= 4.5\%). \tag{2.11}$$

2.3 Pressure Drop and Heat Transfer in a Single-Phase Flow

Many correlations have been proposed in literature for the friction factor and heat transfer, based on experimental investigations on liquid and gas flow in micro-channels. Garimella and Sobhan (2003) presented a comprehensive review of these investigations conducted over the past decade.

Incompressible flow: friction correlations

According to Schlichting and Gersten's (2000) equation, the friction factor is:

$$\lambda = 2\Delta P \frac{d_\mathrm{h}}{L} \frac{1}{\rho U^2} \tag{2.12}$$

where ΔP is the pressure drop across the channel, d_h is the channel hydraulic diameter, L is the channel length, ρ is the fluid density, and U is the bulk fluid velocity.

Laminar flow

For developed laminar flow in smooth channels of $d_\mathrm{h} > 1$ mm, the product $\lambda \mathrm{Re} =$ const. Its value depends on the geometry of the channel. For a circular pipe $\lambda \mathrm{Re} = 64$, where $\mathrm{Re} = U d_\mathrm{h}/\nu$ is the Reynolds number, and ν is the kinematic viscosity.

The correlations of Wu and Little (1984), Choi et al. (1991), and Yu et al. (1995), Maynes and Webb (2002), Turner et al. (2002), Celata et al. (2004), Hetsroni et al. (2005a) predict constant values of $\lambda \mathrm{Re}$ for micro-channels. Predictions by Peng et al. (1994a) for water flow in rectangular micro-channels in the range of d_h from 133 to 343 μm show an altogether different trend: in all cases, $\lambda \mathrm{Re}$ decreases with an increase of the Reynolds number. While the slopes of the curves for all test cases presented by Peng et al. (1994a) are identical, the magnitude of $\lambda \mathrm{Re}$ is highest for the largest micro-channels and lowest for the smallest. Several experimental results of $\lambda \mathrm{Re}$ in the laminar regime for smooth micro-channels are shown in Fig. 2.19. The unusual results obtained by Peng et al. (1994a) are attributable, at least in part, to uncertainties of the experimental data.

Transition and turbulent flows

Transition from laminar to turbulent flow occurs when the friction factor exceeds the low $\lambda \mathrm{Re}$ range. In Fig. 2.20a the results obtained for a tube of diameter 705 μm by Maynes and Webb (2002) are compared against the value accepted for laminar flow $\lambda = 64/\mathrm{Re}$. Based on the above data, one can conclude that the transition occurs at $Re > 2{,}100$.

The friction correlations in the turbulent regime are compared against conventional correlations in Fig. 2.20b. Predictions for nitrogen flow by Choi et al. (1991) agree very well with conventional results; the Wu and Little (1984) correlation is similar to those two in its trend, but the predicted values are much higher in mag-

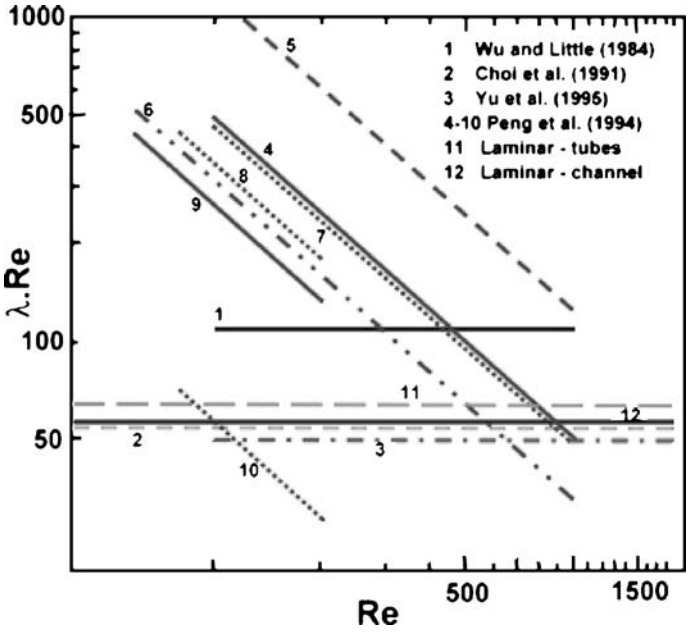

Fig. 2.19 Laminar flow and friction correlations. Reprinted from Sobhan and Garimella (2001) with permission

nitude. The correlations of Peng et al. (1994a) for water flow again exhibit a very different trend: in all cases, λRe decreases with increase of the Reynolds number in contradiction to conventional correlations. The detailed data for single-phase flow in micro-channels (experimental conditions, effect of roughness, energy dissipation) will be discussed later.

Heat transfer. Experimental data for laminar and turbulent flow regimes

The experimental studies have shown departure from the conventional theory for heat transfer. Choi et al. (1991) found that the measured Nusselt number in laminar flow exhibits a Reynolds number dependence, in contrast to the conventional prediction for fully developed laminar flow, in which the Nusselt number is constant. The heat transfer at forced convection in channels with cross-section 0.6×0.7 mm was investigated by Peng and Wang (1998), who observed an unusual trend in this dependence of the Nusselt number. Weisberg et al. (1992) and Bowers and Mudawar (1994) also noted that the behavior of fluid flow and heat transfer in micro-channels without phase change is substantially different from that which typically occurs in conventionally sized channels. Wang and Peng (1994) reported single-phase heat transfer coefficients in six rectangular channels having $0.31 < d_h < 0.75$ mm for water and methanol. The Nusselt numbers were only 35% of those predicted by the Dittus–Boelter equation. By contrast, Webb and Zhang

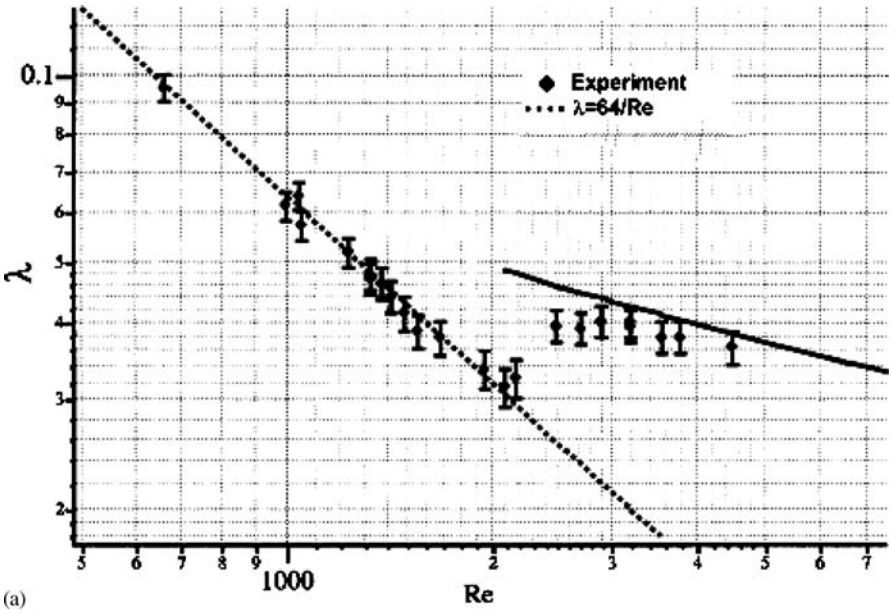

(a)

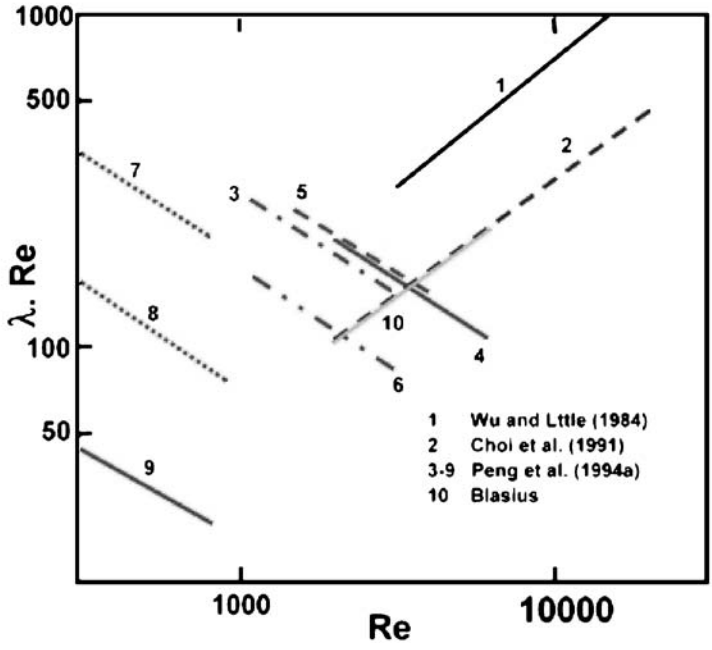

(b)

Fig. 2.20 (**a**) Dependence of the friction factor on Reynolds number for tube of diameter 705 μm. Reprinted from Maynes and Webb (2002) with permission. (**b**) Turbulent flow: friction correlations. Reprinted from Sobhan and Garimella (2001) with permission

(1998) results were adequately predicted by the commonly accepted correlations for single-phase flow in multiple tubes having hydraulic diameters between 0.96 and 2.1 mm. Wu and Little (1984) measured the flow and heat transfer characteristics for the flow of nitrogen gas in heat exchangers. The Nusselt numbers for laminar flow (Re $<$ 600) were lower than those predicted by the correlations. Peng and Peterson (1995) showed a strong effect of the geometric configuration (aspect ratio and ratio of the hydraulic diameter to the center-to-center spacing of the micro-channels) on the heat transfer and flow characteristics in single-phase laminar flow.

The heat transfer correlations are considered separately in the laminar and turbulent regimes in Figs. 2.21 and 2.22, respectively. The dependence of the Nusselt number on the Reynolds number is stronger in all the micro-channel predictions compared to conventional results, as indicated by the steeper slopes of the former; Choi et al. (1991) predict the strongest variation of Nusselt number with Re. The predictions for all cases by Peng et al. (1996) also fall below those for a conventional channel.

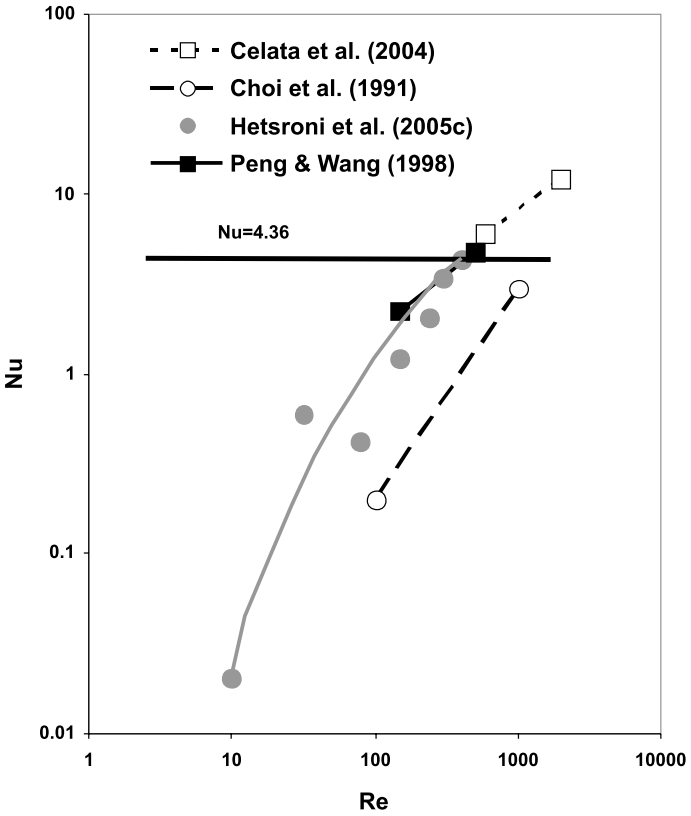

Fig. 2.21 Laminar flow: heat transfer

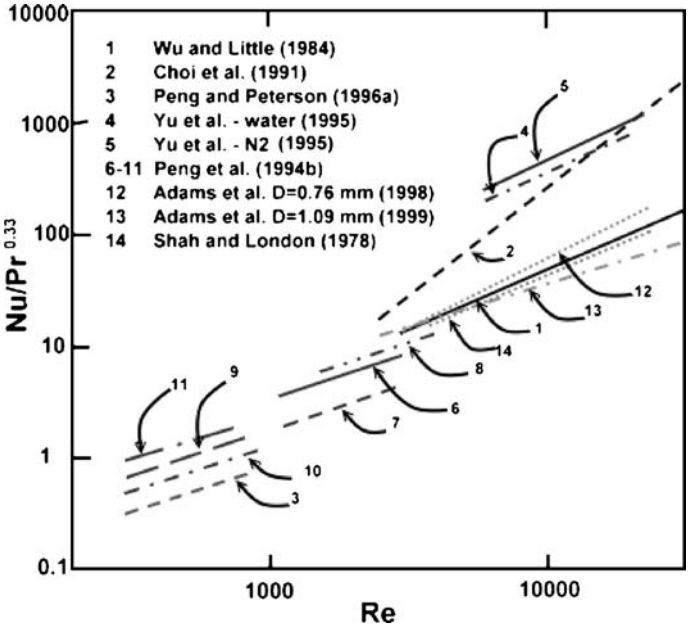

Fig. 2.22 Turbulent flow: heat transfer. Reprinted from Sobhan and Garimella (2001) with permission

Experimental and numerical study of the pressure drop and heat transfer in a single-phase micro-channel heat sink by Qu and Mudawar (2002a,b) demonstrated that the conventional Navier–Stokes and energy equations can adequately predict the fluid flow and heat transfer characteristics.

New questions have arisen in micro-scale flow and heat transfer. The review by Gad-el-Hak (1999) focused on the physical aspect of the breakdown of the Navier–Stokes equations. Mehendale et al. (1999) concluded that since the heat transfer coefficients were based on the inlet and/or outlet fluid temperatures, rather than on the bulk temperatures in almost all studies, comparison of conventional correlations is problematic. Palm (2001) also suggested several possible explanations for the deviations of micro-scale single-phase heat transfer from convectional theory, including surface roughness and entrance effects.

Effect of axial heat conduction in the channel wall

In general, the axial heat conduction in the channel wall, for conventional size channels, can be neglected because the wall is usually very thin compared to the diameter. Shah and London (1978) found that the Nusselt number for developed laminar flow in a circular tube fell between 4.36 and 3.66, corresponding to values for constant heat flux and constant temperature boundary conditions, respectively.

However, for flow in micro-channels, the wall thickness can be of the same order of channel diameter and will affect the heat transfer significantly. For example, Choi et al. (1991) reported that the average Nusselt numbers in micro-channels were much lower than for standard channels and increased with the Reynolds number.

Hetsroni et al. (2004a) obtained similar results for heat transfer in a circular stainless steel tube of inner diameter 1.07 mm and outer diameter 1.50 mm. In the turbulent regime, the predictions of all investigators with the exception of Peng et al. (1994b) and Peng and Peterson (1996) fell below the conventional channel values. In particular, those of Adams et al. (1998, 1999) and Wu and Little (1984) lay in one group. The predictions of Choi et al. (1991) and Yu et al. (1995) were also somewhat comparable, forming a different group. It should be noted that these groups differ neither in fluid type (both groups cases refer to nitrogen and water) nor in micro-channel dimensions. The rectangular micro-channels of different dimensions considered in Peng et al. (1994b) exhibited a wide range of the predicted Nusselt numbers. In all these cases, as well as in that of Peng and Peterson (1996), the predicted values lay below those of the Dittus–Boelter equation presented by Shah and London (1978).

One drawback of a single-phase micro-channel heat exchanger is a relatively high temperature rise longitudinally compared to traditional heat sinks. Furthermore, the fluid flow rate might not be evenly distributed between the parallel micro-channels. Steep temperature gradients produce thermal stresses in the elements and packages due to the differences in the coefficient of thermal expansion, thus impairing the device reliability. Heat transfer in gas flow and thermal effects will be discussed in Chaps. 3 and 4.

Special features of gas flow

In designing micro-scale devices, it is necessary to establish the physical laws governing gas flow in small conduits. Among other things, such flow may differ from its macroscopic counterpart in that relatively high, subsonic Mach numbers may be maintained concurrently with low Reynolds numbers, the surface area to the volume ratio is huge (on the order $10^6\,\mathrm{m}^2/\mathrm{m}^3$), the fabrication process may lead to relatively heavy surface roughness, and non-continuum effects may occur at pressures above one atmosphere. In a recent review of single-phase flow and heat transfer data at the micro-scale, Guo and Li (2003) discussed the influence of gas rarefaction, and the combined influence of channel size and surface roughness. Their primary conclusion was that the small characteristic length of the micro-channels favors wide variation of the flow properties – pressure, density, and velocity – even in the absence of rarefaction. In viscosity-dominated flows, their compressibility has to be taken into account. It was recognized that there can be significant differences between the inlet and exit Mach numbers and that flow compressibility is likely to influence the friction factor and Nusselt number. Surface effects like friction-induced compressibility, surface roughness, viscous forces and axial heat conduction were attributed to the large surface area to volume ra-

tio of micro-channels, compared to conventional conduits. Finally, it was acknowledged that between experimental results and theoretical values there could be a result of entranced effects and measurement error rather than specific micro-scale phenomena.

Turner et al. (2004) studied the independent variables: relative surface roughness, Knudsen number and Mach number and their influence on the friction factor. The micro-channels were etched into silicon wafers, capped with glass, with hydraulic diameters between 5 and 96 μm. Their surface roughness was $0.002 < k_s <$ 0.06 μm for the smooth channels, and $0.33 < k_s < 1.6$ μm for the glass-capped ones. The surface roughness of the glass micro-channels was measured to be in the range $0.0014 < k_s < 0.003$ μm.

Continuum friction factor and entrance length

The average friction factor for the helium test cases is plotted against the Reynolds number in Fig. 2.23, with designation of the sample ($N = 319\ldots$), the hydraulic diameter d_h, the relative roughness k_s/H, and the Knudsen and Mach number ranges, indicated for each case. For the largest micro-channel, the experimental friction factor agrees with the theoretical value. As d_h decreases, so does the friction factor. This is most noticeable in the case $N = 0.72$ in which Kn $= 0.01$ for the entire length of the channel.

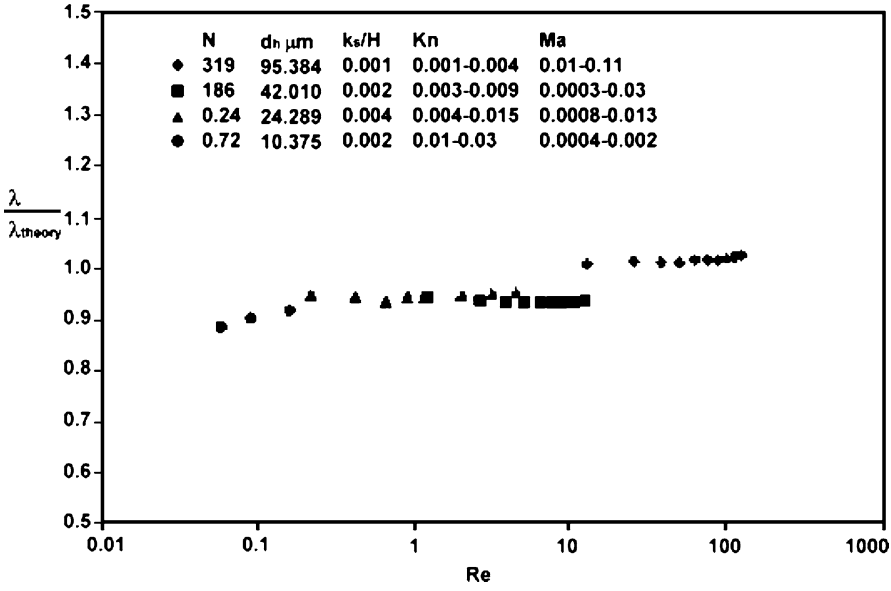

Fig. 2.23 Average friction factor for helium flow plotted against Reynolds number. Reprinted from Turner et al. (2004) with permission

Rarefaction

The influence of rarefaction was isolated from that of compressibility and surface roughness by conducting low-Re, low-Ma flow tests through smooth micro-channels. For a given micro-channel, Kn was varied by testing gases with different mean free paths ($\overline{\lambda}_{\mathrm{He}} \approx 3\overline{\lambda}_{\mathrm{air}}$) and by reducing the pressure to below atmospheric conditions. The Kn range was also expanded by testing micro-channels of different length. Additionally, since Kn increases along the channel length (as the pressure decreases), the local pressure measurements were used to determine the friction factor for four different values of average Kn along the channel. The experimental λ was normalized versus the incompressible $\lambda_{\mathrm{theory}}$ and is plotted versus Kn in Fig. 2.24, which shows close agreement between λ and $\lambda_{\mathrm{theory}}$ for $\mathrm{Kn} < 0.01$ (continuum flow regime). As Kn was increased above 0.01, λ decreased significantly up to 50% of the continuum value at $\mathrm{Kn} = 0.15$.

Compressibility

Experiments were conducted with air through micro-channel $N = 319$ ($d_{\mathrm{h}} = 95.384\,\mu\mathrm{m}$) to determine the effect of compressibility on the friction factor. The relative surface roughness was low ($k_{\mathrm{s}}/H = 0.001$) and $\mathrm{Kn} < 0.001$, thus the experiments were effectively isolated from the influence of surface roughness and rarefaction. The local friction factor is plotted versus Ma in Fig. 2.25 for air. The experimental λ increases about 8% above the theoretical λ as Ma increases to 0.35.

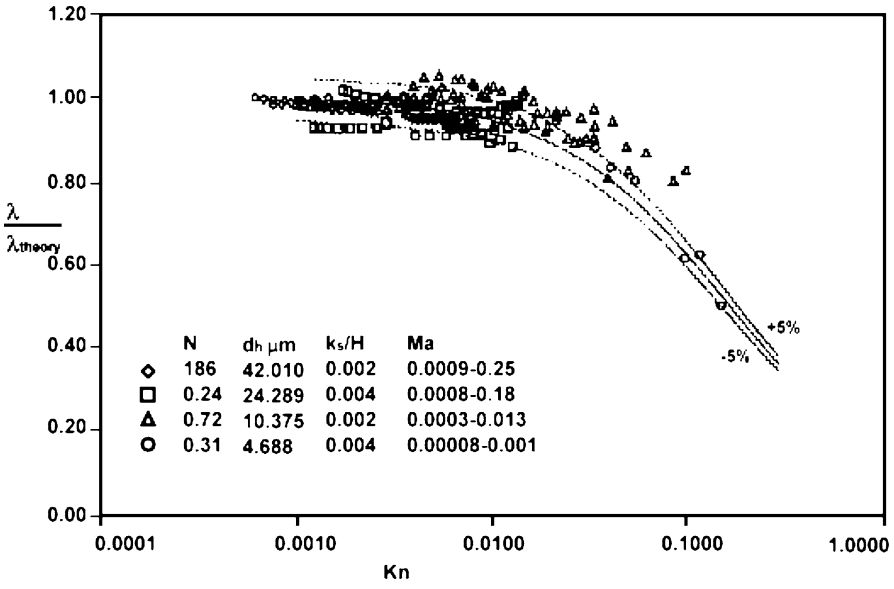

Fig. 2.24 Influence of rarefaction on the local friction factor. Reprinted from Turner et al. (2004) with permission

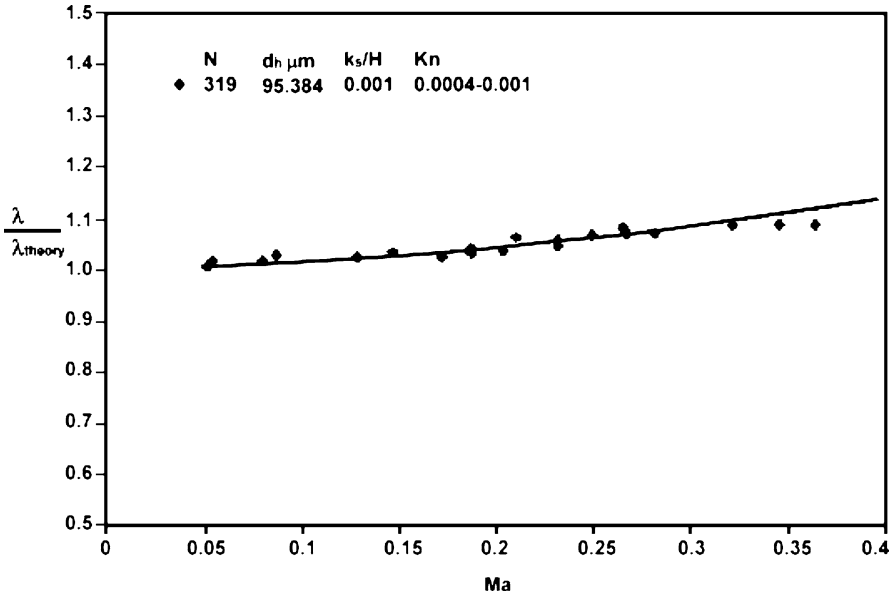

Fig. 2.25 Influence of compressibility on local friction factor for air. Reprinted from Turner et al. (2004) with permission

Celata et al. (2005) studied the gaseous flow of helium through micro-tubes of diameter between 30 and 254 μm and high L/d ratio (between 300 and 2400) at Reynolds numbers up to 500. They concluded that the quantitative behavior is satisfactory predicted by incompressible theory, and that the friction losses at the inlet and outlet give only a minor contribution to the total pressure drop. Morini et al. (2006) investigated the characteristics of gaseous flow of nitrogen in commercial stainless steel micro-tubes of $d = 762$, 558 and 127 μm and $L/d = 800-3{,}800$ at $\mathrm{Re} = 300-4{,}000$. It was observed that in laminar regime the Poiseuille low correctly predicts the value of the pressure drop. Laminar to turbulent transition takes place at $\mathrm{Re} = 1{,}800-1{,}900$.

Surface roughness

The average λ is plotted versus Re for $H = 10\,\mu\mathrm{m}$ channels in Fig. 2.26. In this figure, the difference in λ between the smooth and rough channels is generally less than 3%. To investigate the effect of surface roughness on rarefied gas flow, the smooth and rough channels of $H = 5$ and 10 μm were tested with air and helium at below atmospheric pressure. The test resulted in a Knudsen number range of $0.006 < \mathrm{Kn} < 0.11$, and friction factor λ was normalized by $\lambda_{\mathrm{theory}}$ ($\mathrm{Kn} = 0$) and is plotted versus Kn in Fig. 2.27. In the slip flow regime ($0.01 < \mathrm{Kn} < 0.1$) there is no clear difference in λ for the smooth and roughness cases. Overall, the influence of the relative surface roughness on the friction factor appears to be quite weak

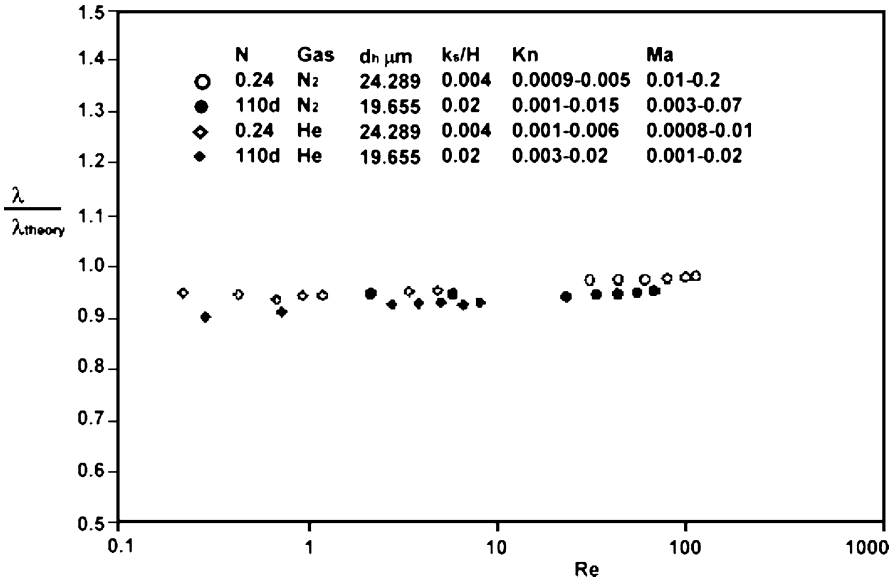

Fig. 2.26 Influence of surface roughness on friction factor. Reprinted from Turner et al. (2004) with permission

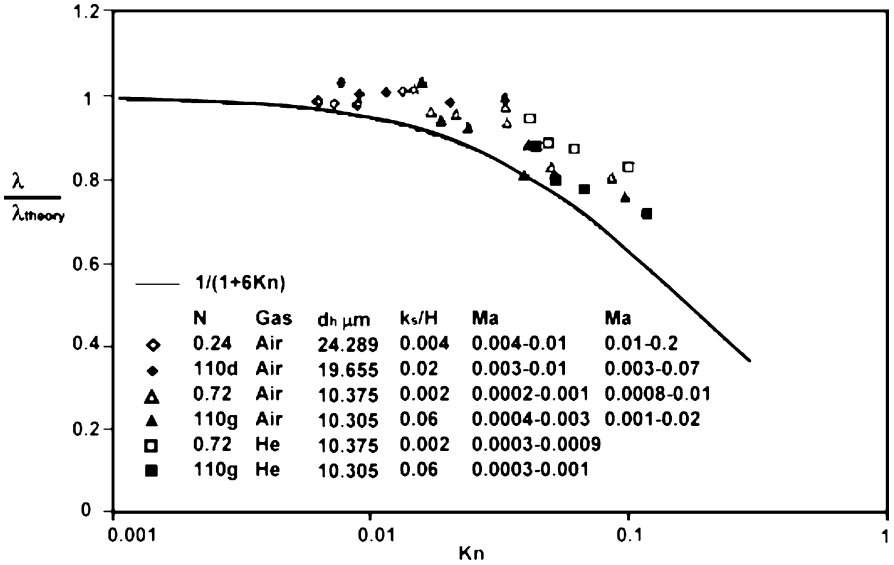

Fig. 2.27 Influence of surface roughness on rarefied flow. Reprinted from Turner et al. (2004) with permission

(within 2 to 6%). The experiments showed that λ for the smooth case is within 3% of that for the rough case, which is also within the experimental uncertainty. Considering that the rough channels have a higher uncertainty associated with the friction

factor, there is no statistical difference between the two cases. The friction factor is strongly dependent on the measurement of channel height. Consequently, as its standard deviation increases (as is expected and desired for rough surfaces), so does the uncertainty of the friction factor. To accommodate for this inherent uncertainty, great care is to be taken to ensure uniform channel depth and surface roughness along both the channel width and length.

The above results show close agreement between the experimental and theoretical friction factor (solid line) in the limiting case of the continuum flow regime. The Knudsen number was varied to determine the influence of rarefaction on the friction factor with k_s/H and Ma kept low. The data shows that for Kn < 0.01, the measured friction factor is accurately predicted by the incompressible value. As Kn increased above 0.01, the friction factor was seen to decrease (up to a 50% λ as Kn approached 0.15). The experimental friction factor showed agreement within 5% with the first-order slip velocity model.

The influence of compressibility was assessed by varying the Mach number in the range $0 <$ Ma < 0.38, while Kn and k_s/H were kept low. Friction factor data were reported only with Ma < 1 at the exit, to ensure the flow rate was controlled by viscous forces alone. A mild increase in the friction factor (8%) was observed as Ma approached 0.38. This effect was verified independently by numerical analysis for the same conditions as in the experiment. The range of relative surface roughness tested was $0.001 < k_s/H < 0.06$, yet there was no significant influence on the friction factor for laminar gas flow.

2.4 Steam–Fluid Flow

To achieve higher heat dissipation rates for micro-electronic technologies, the fundamentals of two-phase heat transfer in micro-channels are being studied ever more extensively. Two-phase flow maps and heat transfer prediction methods exist for vaporization in macro-channels, but these are not applicable in micro-channels due to the small-scale phenomena involved, which have to be studied separately. A state-of-the-art overview of boiling and two-phase flows in micro-channels was published by Thome (2006). The most important aspects to control are the frequencies, lengths and velocities of the bubbles and the coalescence processes, which control the flow pattern transitions. To better predict the heat transfer coefficients in micro-cooling elements and heat spreaders for electronics cooling, for example, it is desirable to develop a map for predicting the flow regimes. Due to the predominance of surface tension over the gravity forces, the tube orientation has a negligible influence on the flow pattern. For this reason stratified flow does not exist in horizontal micro-channels (Triplett et al. 1999).

Single micro-channel

Thome et al. (2004) and Dupont et al. (2004) proposed the first mechanistic analysis for vaporization in a micro-channel, with a three-zone flow boiling model describing

the transient variation in the local heat transfer coefficient during sequential and cyclic passage of (1) a liquid slug, (2) a vaporizing elongated bubble, and (3) a vapor slug created by film dryout. Figure 2.28 shows this model, in which δ_0 is the initial liquid film thickness, δ_{min} the minimum liquid film thickness, L_L the length of the liquid slug, L_G the length of the vapor bubble, L_p the length of the pair (liquid slug/bubble), L_{dry} the length of the dryout zone, L_{film} the length of the liquid film, q the heat flux and r, d the radius and diameter of the tube. The new model illustrates the strong dependence of heat transfer on the bubble frequency, the lengths of the system elements, and the liquid film thickness, and is so far only applicable to the slug flow regime.

Flow patterns

Serizawa et al. (2002) studied the flow patterns in steam–water flow. Figure 2.29 shows their observations in a 0.05 mm glass channel. Here a new pattern was identified, namely, liquid ring flow.

The micro-scale flow patterns described by Revellin et al. (2006) were categorized as follows:

1. Bubbly flow. Here the bubbles were shorter than the tube diameter and the vapor phase was distributed as discrete bubbles in a continuous liquid phase (Fig. 2.30a).
2. Bubbly/slug flow. Bubbles both longer and shorter than the channel diameter (Fig. 2.30b). The bubble frequencies increase rapidly with the heat flux in the evaporator, reached a peak 900 Hz and then decreased due to coalescence.
3. Slug flow. Vapor bubbles longer than the channel diameter, which is slightly smaller than that of the tube. The bubbles were separated from the inner channel

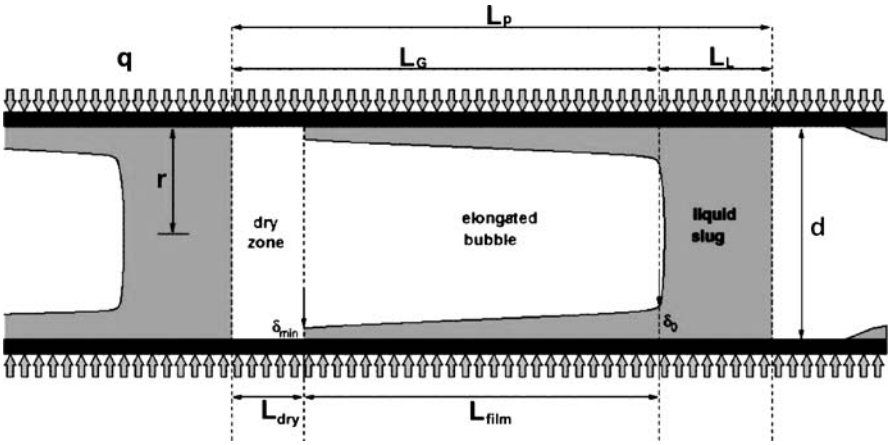

Fig. 2.28 Schematic of three-zone vaporization model. Reprinted from Thome et al. (2004) with permission

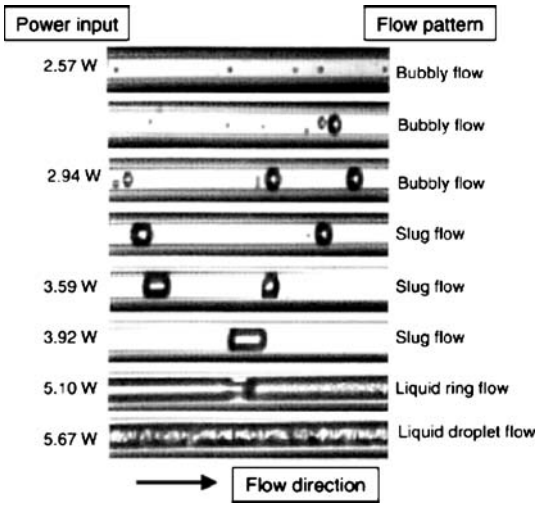

Fig. 2.29 Flow regimes in 50 μm channel for steam–water flows. Reprinted from Serizawa et al. (2002) with permission

wall by a thin film of liquid and from one another by liquid slugs (Fig. 2.30c). The bubble frequency decreased with increasing vapor quality due to coalescence but at a slower rate than in the case of small bubbles.

4. Slug/semi-annular flow. Here both slug and semi-annular flows were present. The vapor velocity increased with the heat flux and the rear of elongated bubbles began to break up (Fig. 2.30d). Coalescence was no longer clean and created a churn-like zone where the liquid slug had been.
5. Semi-annular flow. Liquid slugs were non-existent (Fig. 2.30e). A liquid film formed at the tube wall with a nearly continuous central vapor core, truncated periodically by churning liquid–vapor zones, which disappear gradually.
6. Annular flow (wavy and smooth). A liquid film flowed on the tube wall with a continuous central vapor core without churning zones (Fig. 2.30f,g).

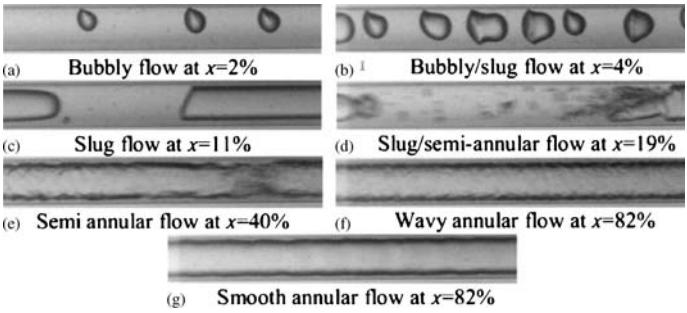

Fig. 2.30a–g Flow patterns and transitions for $d = 0.5$ mm, $L = 70$ mm, $G = 500\,\mathrm{kg/m^2s}$, $T_s = 30\,^{\circ}\mathrm{C}$ and $\Delta T_{sub} = 3$ K. Reprinted from Revellin et al. (2006) with permission

Flow pattern maps

Two-phase flow pattern maps, observed by Revellin et al. (2006), are presented in Fig. 2.31 in mass flux versus vapor quality, and superficial liquid velocity versus superficial vapor velocity formats calculated from the test results as follows:

$$U_{\mathrm{LS}} = \frac{(1-\chi)G}{\rho_{\mathrm{L}}} \tag{2.13}$$

$$U_{\mathrm{GS}} = \frac{\chi G}{\rho_{\mathrm{G}}} \tag{2.14}$$

where U_{LS} and U_{GS} are the liquid and vapor superficial velocities, respectively, and χ is the vapor quality.

Notably, the higher the mass flux, the earlier annular flow is reached. Bubbly flow is more or less non-existent for mass fluxes exceeding $1{,}000\,\mathrm{kg/m^2\,s}$. The most important observation about the flow patterns is that their transitions are controlled primarily by the rate of coalescence, which is not recognized as a contributing factor by any of the micro-scale or macro-scale flow pattern maps.

Coalescing flow map for vaporizing flows in micro-channels

In order to create phenomenological heat transfer and frictional pressure drop models as opposed to wholly empirical methods, the two-phase flow characteristics of each type of flow need to be discernible. For example, the Thome et al. (2004) three-zone flow boiling model (Fig. 2.28) is currently applicable to slug (elongated bubble) flow and includes the effect of bubble frequency, but only assuming that no coalescence occurs. For further development of such models, it is clear that coalescence must be dealt with directly to account for the variation of the heat transfer coefficient due to the decrease in bubble frequency and increase in bubble length as the coalescence proceeds along the channel. For distinct, high-frequency elongated bubbles, the heat transfer coefficient is controlled primarily by transient conduction through the liquid film surrounding them as against convection through the liquid films in the annular flow regime. To extend the three-zone heat transfer model in the elongated bubble regime and then generalize it to include the heat transfer mechanisms controlling bubbly and annular flows, a composite coalescing flow and diabatic flow type of map is required that reflects both the bubble coalescence phenomena and the critical heat flux limitation. Furthermore, as can be observed in Fig. 2.31, conventional flow pattern maps do not provide the necessary information for development of such models here, since coalescence changes the flow pattern along the channel length and the critical heat flux limits the feasible combinations of mass velocity and vapor quality.

An example of a diabatic coalescing bubble map for vaporizing flow in microchannels is shown Fig. 2.32 (Thome et al. 2006) where Bo is the boiling number, $\mathrm{Bo} = q/Gh_{\mathrm{LG}}$, G is the mass velocity of liquid plus vapor ($\mathrm{kg/m^2\,s}$), h_{LG} is the latent heat of vaporization ($\mathrm{J/kg}$), q_{crit} is the critical heat flux ($\mathrm{W/m^2}$), $\mathrm{Re_L}$ is the

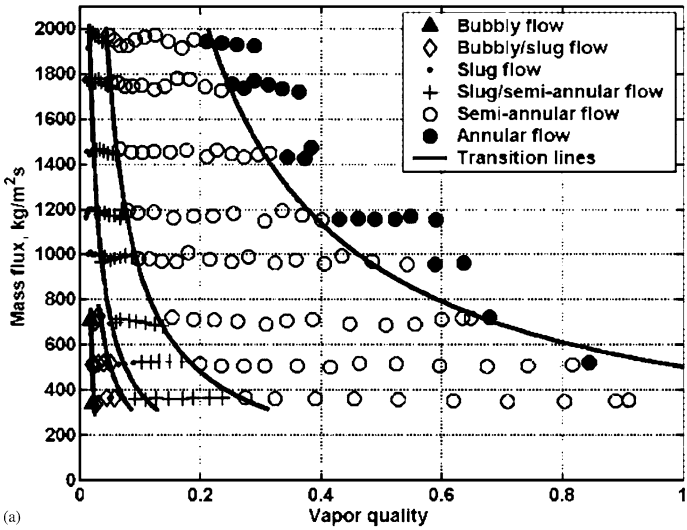

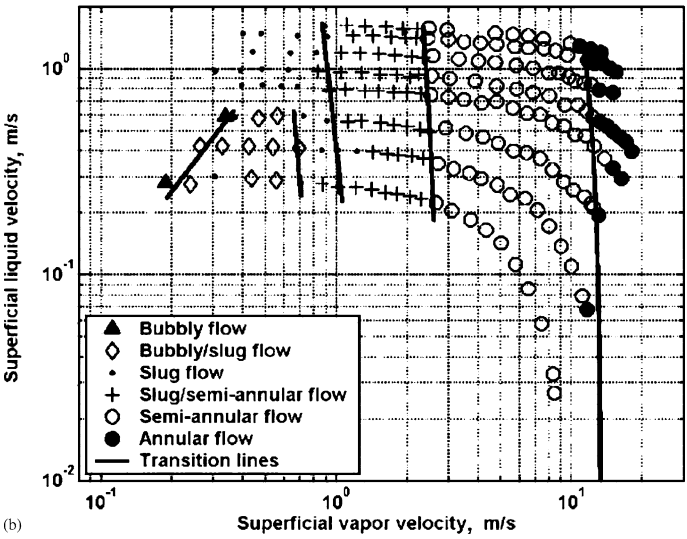

Fig. 2.31a,b Flow pattern maps with experimental transition lines for R-134a, $d = 0.5$ mm, $L = 70$ mm, $T_s = 30\,^{\circ}$C and $\Delta T_{sub} = 3$ K. Reprinted from Revellin et al. (2006) with permission

liquid Reynolds number, $\mathrm{Re_L} = Gd/\mu_L$, $\mathrm{We_G}$ is the vapor Weber number, $\mathrm{We_G} = G^2 d/(\sigma\rho_G)$, and $\mathrm{We_L}$ is the liquid Weber number, $\mathrm{We_L} = G^2 d/(\sigma\rho_L)$.

The first flow pattern zone corresponds to the isolated bubble (IB) regime where the bubble generation rate is much higher than the coalescence rate. It includes both bubbly flow and/or slug flows and is present up to the onset of coalescence process domination. The second zone is the coalescing bubble (CB) regime, which is

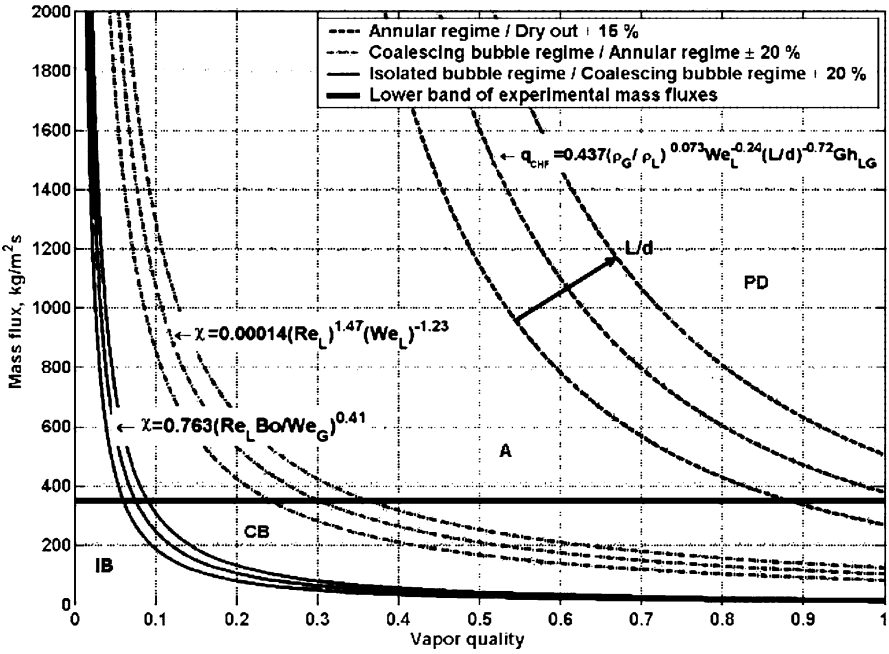

Fig. 2.32 Diabatic flow pattern map for vaporizing flow in uniformly heated micro-channel, R-134a, $d = 0.5$ mm, $L = 70$ mm, $T_s = 30\,^{\circ}\mathrm{C}$, $q = 50\,\mathrm{kW/m^2}$ without subcooling at inlet. Flow patterns: isolated bubble regime (IB), coalescing bubble regime (CB), annular (completely coalesced) regime (A), post-dryout regime (PD). Reprinted from Thome et al. (2006) with permission

present up to the end of the coalescence process. This zone is present when the bubble coalescence rate is higher than the bubble generation rate. The third zone is the annular (A) zone and is limited by the fourth zone of this diabatic map, the post-dryout (PD) zone, whose transition is given by the critical vapor quality signaling the onset of critical heat flux. The transition lines in Fig. 2.32 are predicted by the methods discussed below (notably also showing the accuracy limits of the new transition predictions that are absent in prior conventional flow maps). The lower end of the transition lines below the horizontal black line represents extrapolation below the lowest mass velocities tested, where two-phase flow instabilities occur. Thus the present map does not specifically capture the threshold of two-phase instability at low mass velocities, but this feature remains as a possibility in future tests. Such a diabatic/coalescing flow pattern map with instability limits would provide a complete picture of the physical process for the thermal/hydraulic design of micro-channel evaporators.

Before describing the transition prediction methods, it is instructive to describe how a diabatic map is used. One chooses a desired mass flux and sets the heat flux to be dissipated (assumed uniform along and around the circular channel) up to the desired local length from the inlet to find the corresponding local vapor quality (from an energy balance) and thus the location of this process condition on the map. The

inlet is for a saturated or slightly subcooled liquid ($\chi \approx 0$) and the exit conditions are applied to find the location (at the extreme right), and the resulting horizontal line joining these points represents the flow regimes that will be encountered from inlet to outlet. Significantly, the location of the outlet to the left or right of the dryout transition curve (indicating the vapor quality at which the critical heat flux is reached) shows whether the intended operating conditions are feasible or not. Saturation conditions and the physical properties at the inlet pressure of the micro-evaporator are used for calculating the map.

Parallel micro-channels

The behavior of the flow pattern in a parallel micro-channel is different from that in a single micro-channel. It was shown by Hetsroni et al. (2003b) that at the same value of heat flux, different flow regimes may be observed in different micro-channels, depending on the time interval. Moreover, at the same time interval different flow regimes may exist in each of the component micro-channels. In Fig. 2.33 two-phase steam–water flow in the central part of such a parallel system $d_h = 100\,\mu m$ is shown as the top view observed through a transparent cover. The

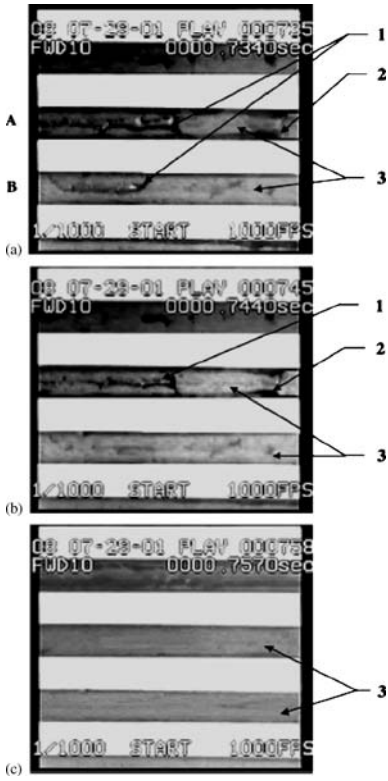

Fig. 2.33a–c Boiling in the central part of micro-channels. $U_{LS} = 0.14\,m/s$, $q = 220\,kW/m^2$. *1* Clusters of liquid droplets at the bottom of the channel. *2* Clusters of the liquid droplets on the side-wall. *3* Steam. Reprinted from Hetsroni et al. (2003b) with permission

field of view is 2.4 mm in the streamwise direction and 2.0 mm in the spanwise direction, the flow moves from left to right. In these images three micro-channels are shown, marked by uniform gray color or by gray color with light and dark regions. In channels A and B, clusters of liquid droplets were observed (Fig. 2.33a). One of the findings of the study is the extreme shortness of the period during which the "vapor with clusters of droplets" regime was observed. The clusters may appear at the corner of the bottom as on the side-walls (Fig. 2.33a, channel A). After 0.01 s, liquid drops were not observed on the bottom of channel B (Fig. 2.33b). Figure 2.33c shows no presence of liquid droplets in both channels.

The temperature distribution on the heated wall depends on the material and design of the module, the inflow rate and the heat flux. For given values of flow rate and heat flux, the infrared (IR) image of the heated module side was clearly observed. Typical IR images of the heated side of the module, which contained 26 micro-channels of $d_h = 100\,\mu m$, are shown in Figs. 2.34 and 2.35. The area of the heater is marked as a square, the flow moved from right to left. We restricted the thermal image analysis to the marked square area of $10 \times 10\,mm^2$. The temperature distribution on the heated wall and the histogram of the thermal field at $q = 190\,kW/m^2$ and $U_{LS} = 0.14\,m/s$ are shown in Fig. 2.34a,b, respectively. In this case the mean temperature (averaged over the surface of the heater) was $T_{mean} = 93.3\,°C$ and boiling was observed in part of the parallel micro-channels only. The temperature measurements indicate that this "partial" boiling took place at $T_{mean} < T_S$ (T_S being the satu-

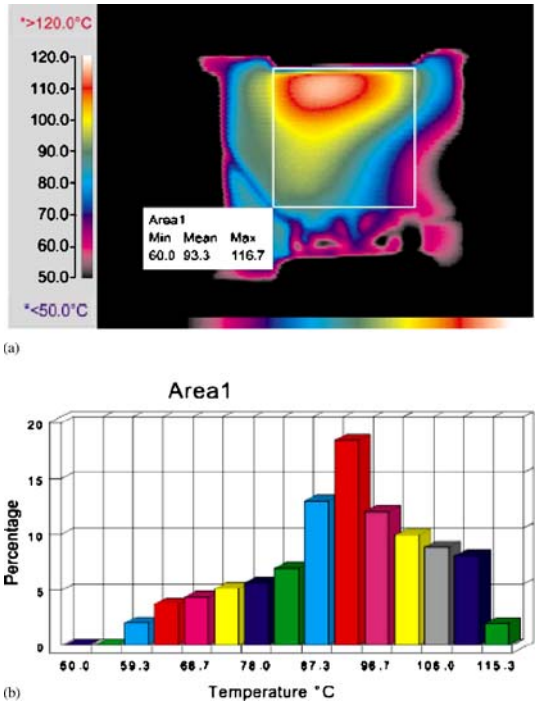

Fig. 2.34a,b Thermal field on the heated wall. $U_{LS} = 0.14\,m/s$, $q = 190\,kW/m^2$. (**a**) Infrared image. (**b**) Histogram of temperature distribution. Reprinted from Hetsroni et al. (2003b) with permission

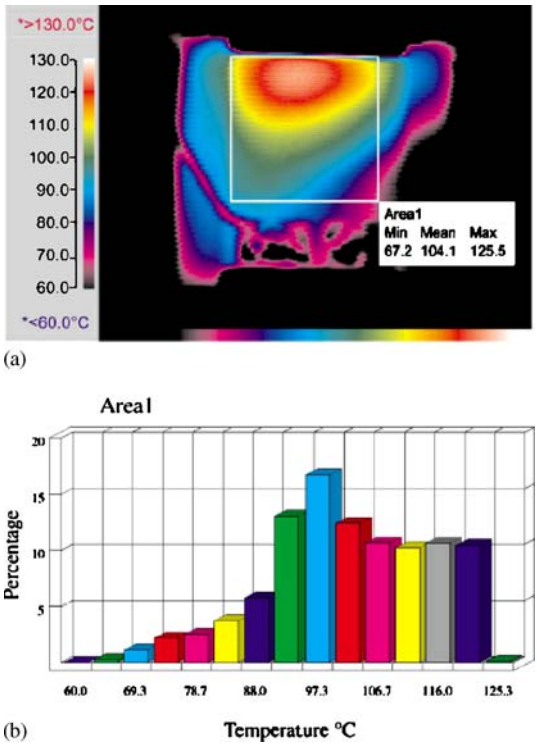

Fig. 2.35a,b Thermal field on the heated wall. $U_{LS} = 0.14\,\mathrm{m/s}$, $q = 220\,\mathrm{kW/m^2}$. (**a**) Infrared image. (**b**) Histogram of temperature distribution. Reprinted from Hetsroni et al. (2003b) with permission

ration temperature), whereas at $T_{mean} > T_S$ boiling in all parallel micro-channels was observed. The temperature distribution on the heated wall and the histogram of the thermal field at $T_{mean} = 104.1\,^{\circ}\mathrm{C}$, $q = 220\,\mathrm{kW/m^2}$ and $U_{LS} = 0.14\,\mathrm{m/s}$ are shown in Fig. 2.35a,b, respectively. From Figs. 2.34 and 2.35 one can conclude that the variation of $(T_{max} - T_S)$ is more than 20 K, where T_{max} is the maximum temperature on the heated surface. It is clear that consideration of boiling curve and flow regimes in parallel micro-channels should take into account such wide variation of the wall temperature.

Boiling regimes

In Fig. 2.36 the dimensionless heat flux q^* is plotted versus the difference $(T_{max} - T_S)$. The dimensionless heat flux is defined as $q^* = [q/(Gc_p\Delta T)](T_{max}/T_{mean})$, where q is the heat flux, G is the mass flux, c_p is the specific heat, $\Delta T = T_S - T_{in}$, T_S is the saturation temperature, T_{in} is the water temperature supplied to the inlet collector, and T_{max} and T_{mean} are maximum and average temperature of the heated surface, respectively. The term $q/(Gc_p\Delta T)$ reflects the effect of subcooling.

In physical objects involving thermal and fluid flow systems, the dual problem of how the heater is represented, and boiling as a local-instantaneous effect, should be considered. The temperature variations on the chip surface are a key characteristic of

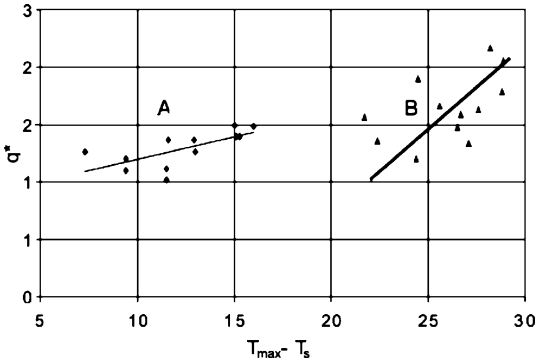

Fig. 2.36 Flow regime map for parallel micro-channels. Region A is the low-heat flux region, and region B the high-heat flux region. Reprinted from Hetsroni et al. (2003b) with permission

such a problem. In Fig. 2.36 two regions of convective boiling may be distinguished. In region A the value of $(T_{\max} - T_S) < 20\,\mathrm{K}$ and boiling was observed in part of the parallel micro-channels only. It may be referred to as the low-heat flux region. Region B, shown in Fig. 2.36, may be referred to as the high-heat flux region; in this case $(T_{\max} - T_S)$ exceeds 20 K.

It should be noted that these results were obtained under conditions of intermittent dryout. The physical implication of such a phenomenon will be discussed in the next section.

Intermittent dryout

Two-phase micro-channel heat sinks generally involve flow boiling in straight, constant cross-section channels. Flow boiling in parallel channels was studied from the subcooled liquid entry at the inlet to a liquid–vapor mixture flow at the outlet. Once nucleation begins, the heat flux causes a sudden release of energy into the vapor bubble, which grows rapidly and occupies the entire channel. The vapor slug may be considered as an elongated bubble. The rapid bubble growth pushes the liquid–vapor interface on both caps of the vapor slug at the upstream and the downstream ends and leads to reversed flow. When in some parallel channels the liquid on the upstream side is pushed back, the other parallel channels carry the resulting excess flow. Figure 2.37 illustrates two-phase flow, driven by the pump, in a certain part of the parallel micro-channels of $d_h = 130\,\mu\mathrm{m}$ (Hetsroni et al. 2005b). It is the top view and the flow pattern was observed through the transparent cover. The field of view is 8 mm in the streamwise direction and 4 mm in the spanwise direction, the flow moves from the bottom to the top, the mass flux is $G = 95\,\mathrm{kg/m^2\,s}$, and the heat flux is $q = 160\,\mathrm{kW/m^2}$. The vapor (the white regions in Fig. 2.37) may be observed at different distances from the inlet. The successive images obtained, using high-speed video, showed that the flow patterns were periodic. The liquid front was seen to pass periodically the region located near the inlet manifold, and the vapor phase occupied most of the channel core; the periodic wetting and rewetting phenomena were also observed. The behavior of long vapor bubbles in a micro-channel was not similar to annular flow with intermittent slugs of liquid between two long vapor

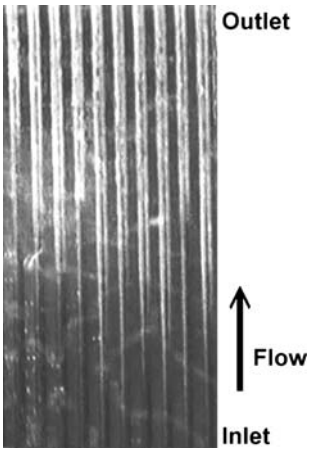

Fig. 2.37 Flow boiling in parallel micro-channels. $G = 95\,\mathrm{kg/m^2 s}$, $q = 160\,\mathrm{kW/m^2}$. Reprinted from Hetsroni et al. (2005b) with permission

trains. The periodic phenomena described above may be regarded as explosive boiling. The trigger mechanism of such a regime is venting of the elongated bubble due to very rapid expansion. Downstream of the onset of nucleate boiling (ONB point) the region of the venting of elongated bubble and dryout was observed.

Bubble growth in micro-channel

The location (along the channel) of appearance of the first bubble at a given flow rate, depends on the local surface temperature variation. Since the heated length of the test section is short (10 mm), at high values of heat flux significant interaction takes place between the steam generated in the micro-channel and the feed water. It is very difficult to capture the behavior of the elongated bubble at high values of heat flux. We investigated this phenomenon at mass flux $G = 95\,\mathrm{kg/m^2\,s}$ and heat flux $q = 80\,\mathrm{kW/m^2}$. Figure 2.38a–h shows a sequence of bubble formation in one of the parallel triangular channels of $d_\mathrm{h} = 130\,\mu\mathrm{m}$. Visualization of the flow pattern was realized near the ONB point. The incipience of boiling is a local phenomenon, which strongly depends on both the hydrodynamic and thermal conditions. The onset of nucleate boiling was established when the first bubbles were observed and the channel wall exceeded the saturation temperature. In general, at a given flow rate the ONB location moved upstream as the heat flux increased, as in ordinary sized channels. The main flow moved from the bottom to the top. Figure 2.38a shows a single bubble, which begins to grow along the channel. Figure 2.38b–d illustrate the bubble growth in the axial direction. Note that at this stage the bubble expands preferentially in the streamwise direction. Figure 2.38e,f show venting of the elongated bubble. Figure 2.38g,h show rewetting. The life time of the elongated bubble (the time between images shown in Fig. 2.38b and Fig. 2.38e) is about 0.01 s. At a given mass flow rate the life time sharply decreases with increasing heat flux. This is why under certain conditions (periodic flow reversal) we consider the mechanism of saturated boiling in micro-channels as an explosive boiling process. Het-

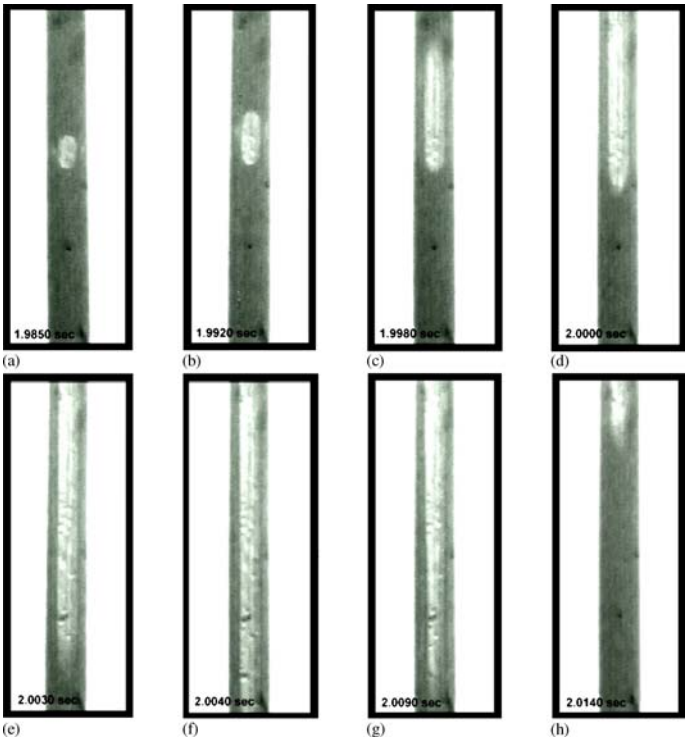

Fig. 2.38a–h Bubble growth at low heat flux. $G = 95\,\mathrm{kg/m^2s}$, $q = 80\,\mathrm{kW/m^2}$. Reprinted from Hetsroni et al. (2003b) with permission

sroni et al. (2001a, 2002a) observed rapid flow reversal inside an individual channel in parallel triangular micro-channels; Steinke and Kandlikar (2003) reported reverse displacement in a set of six parallel micro-channels, $d_h = 200\,\mu\mathrm{m}$. The system departs from stable operating conditions, and hydrodynamic instability sets in. This boiling mode leads to liquid–vapor alternating flow in the region located near the ONB.

Region along the channel after venting of an elongated bubble

After venting of the elongated bubble, the region of "liquid droplets" begins. The vapor phase occupies most of the channel core. The distinctive feature of this region is the periodic dryout and wetting phenomenon. The duration of the two-phase period, i.e., the presence of a vapor phase and micro-droplet clusters on the heated wall, affects the wall temperature and heat transfer in micro-channels. As the heat flux increases, while other experimental conditions remain unchanged, the duration of the two-phase period decreases, and CHF is closer.

Figure 2.39a–o illustrates a typical example of alternate two-phase flow patterns at a distance of 1,000–1,500 μm downstream from the inlet of the test section. In

Fig. 2.39a–o a single triangular channel of $d_h = 130\,\mu m$ and the walls between the adjacent channels (white strips) are depicted in the central part and in the peripheral parts of each image, respectively. The field of view (including the channel and the walls) is $0.6 \times 0.6\,mm^2$, the flow moves from the bottom to the top, the mass flux is $G = 95\,kg/m^2\,s$, and the heat flux is $q = 160\,kW/m^2$. Figure 2.39a shows

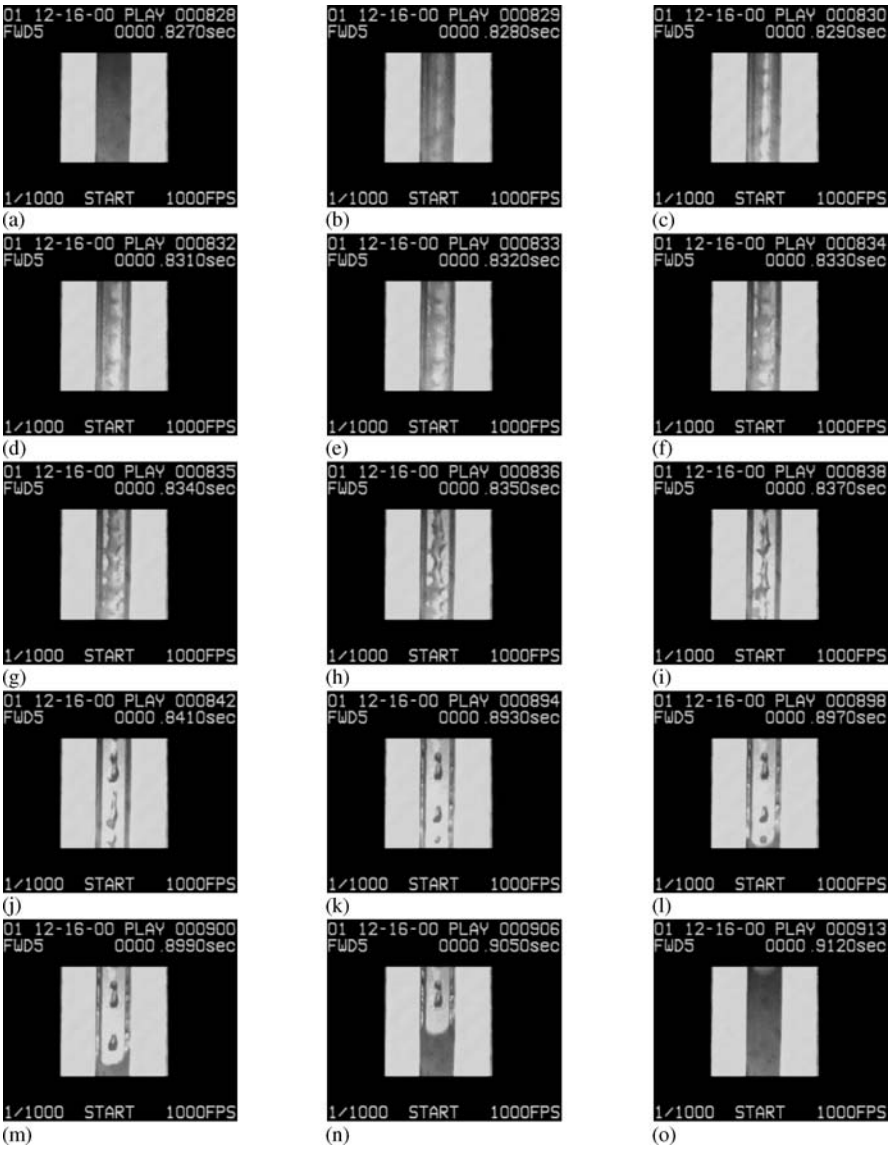

Fig. 2.39a–o Flow pattern at high heat flux. $G = 95\,kg/m^2s$, $q = 160\,kW/m^2$. Reprinted from Hetsroni et al. (2005b) with permission

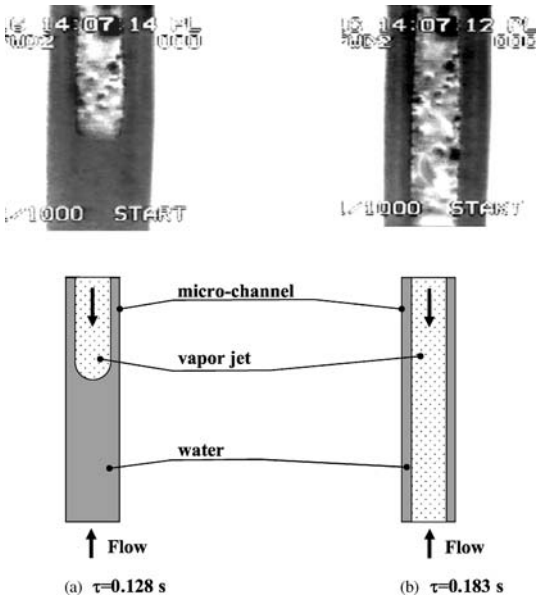

Fig. 2.40a,b Flow pattern upstream of the ONB. (**a**) Single-phase water flow. (**b**) Jet that penetrates the bulk of the water. Reprinted from Hetsroni et al. (2006b) with permission

the water flow that moved through the micro-channel. When the water moves along the channel it is heated up to saturation temperature and then the elongated bubble vents in a short time. Figure 2.39b displays the onset of two-phase reversal flow, which evolved due to venting of the elongated bubble downstream from the observation point. From Fig. 2.39a,b one can conclude that at the specified conditions of this experiment, the life time of the elongated bubble did not exceed 0.001 s. Comparison between the present results obtained at mass flux $G = 95\,\mathrm{kg/m^2\,s}$ and heat flux $q = 160\,\mathrm{kW/m^2}$ to those shown in Fig. 2.38 and obtained at mass flux $G = 95\,\mathrm{kg/m^2 s}$ and heat flux $q = 80\,\mathrm{kW/m^2}$ indicates that doubling of the heat flux causes an approximately tenfold decrease of the life time of the elongated bubble.

Figure 2.39c–f show the annular flow, where the liquid film on the wall is symmetrically distributed.

Figure 2.39g,h display the onset of dryout, where liquid droplets are accumulated at the bottom of the triangular channel. Figure 2.39i–k show that the amount of liquid phase decreases, and only a few droplets of water remain on the channel bottom. Figure 2.39l shows the beginning of wetting and the channel is filled with liquid (Fig. 2.39m–o). The flow patterns depicted in Fig. 2.39a–o were also observed by Serizawa et al. (2002) in steam–water flow in a 50 μm silicon tube. The authors reported that at low liquid flow rates, partially continuous liquid film flow changed to rivulets or even to discrete liquid lumps or large liquid droplets.

The periodic phenomenon described above indicates that the entire channel acts like the area beneath a growing bubble, going through periodic drying and rewetting. The cycle was repetitive with venting of the elongated bubble. Such a behavior affects the mean flow characteristics that usually are measured at the manifolds.

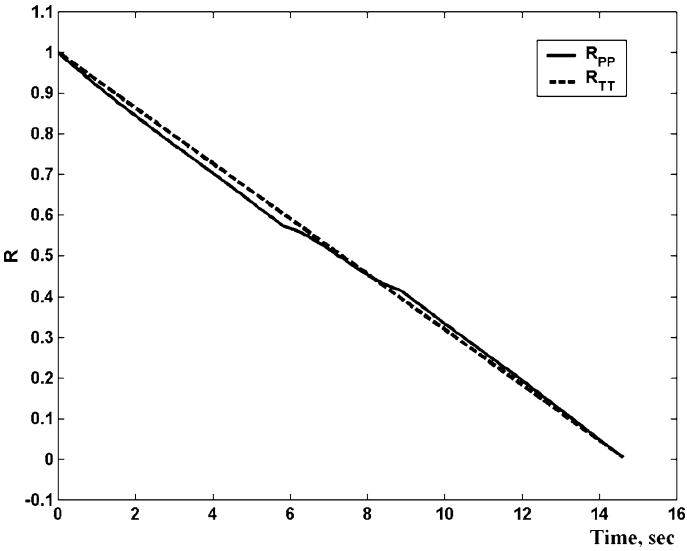

Fig. 2.41 Auto-correlation functions for pressure and temperature fluctuations. Reprinted from Hetsroni et al. (2002b) with permission

Figure 2.40 shows the unsteady flow upstream of the ONB in one of the parallel micro-channels of $d_h = 130\,\mu m$ at $q = 228\,kW/m^2$, $m = 0.044\,g/s$ (Hetsroni et al. 2001b). In this part of the micro-channel single-phase water flow was mainly observed. Clusters of water appeared as a jet, penetrating the bulk of the water (Fig. 2.40a). The vapor jet moved in the upstream direction, and the space that it occupied increased (Fig. 2.40b). In Fig. 2.40a,b the flow moved from bottom to top. These pictures were obtained at the same part of the micro-channel but not simultaneously. The time interval between events shown in Fig. 2.40a and Fig. 2.40b is 0.055 s. As a result, the vapor accumulated in the inlet plenum and led to increased inlet temperature and to increased temperature and pressure fluctuations.

The auto-correlation functions for the pressure R_{pp} and temperature R_{TT} fluctuations are presented in Fig. 2.41. It is clear that the temporal behavior of the temperature fluctuations corresponds to that of the pressure fluctuations (Hetsroni et al. 2002b).

As the heat flux increases, while other experimental conditions remain unchanged, the duration of the two-phase period decreases, and the critical heat flux is closer.

Critical heat flux

As boiling in micro-channel heat sinks is an attractive method for cooling computer CPUs and other high-heat flux devices (such as laser diodes), it is of crucial importance to accurately predict the critical heat flux (CHF) in the small-diameter channels. Critical heat flux or burnout is a limiting value for safe operation of heat dis-

sipation applications and refers to replacement of liquid in contact with the heated surface with a vapor blanket. The thermal conductivity of the vapor is very low compared to the liquid and the surface heat transfer coefficient drops dramatically, resulting in sudden increase of the surface temperature and possible failure of the cooled device. CHF may occur in natural convection boiling, subcooled, as well as in low quality and high-quality saturated boiling conditions.

Natural convection boiling

The effect of annular channel size and length on the CHF was studied under conditions of natural convection boiling by Hetsroni et al. (2007). Restriction of the boiling space was achieved by using unheated glass tubes of different inner diameter, from 2.5 to 9 mm, and length of 24 and 36 mm (typical of micro-channel heat exchangers). The generated vapor rose up through the annular channel between the heated stainless steel tube and the glass tube to the free interface and condensed in a water-cooled condenser.

Data were taken for both increasing and decreasing heat fluxes. Yao and Chang (1983) showed that the squeezing effect of a bubble due to the confinement may be described by the Bond number. For water boiling in gap sizes of $\delta = 0.45$, 1.2, 2.2, and 3.7 mm, the Bond numbers, $\mathrm{Bn} = \delta(\sigma/g(\rho_\mathrm{L} - \rho_\mathrm{G}))^{-0.5}$, were 0.185, 0.493, 0.9 and 1.52, respectively, where δ is the gap size, σ is the surface tension, g is the acceleration due to gravity, and ρ_L and ρ_G are the liquid and vapor densities.

Effect of channel size

Figure 2.42 shows boiling curves obtained in an annular channel with length 24 mm and different gap size (Bond numbers). The heat flux q is plotted versus the wall excess temperature $\Delta T = T_\mathrm{W} - T_\mathrm{S}$ (the natural convection data are not shown). The horizontal arrows indicate the critical heat flux. In these experiments we did not observe any signs of hysteresis. The wall excess temperature was reduced as the Bond number (gap size) decreased. One can see that the bubbles grew in the narrow channel, and the liquid layer between the wall and the base of the bubble was enlarged. It facilitates evaporation and increases latent heat transfer.

For low Bond numbers (on the order of or less), the squeezing effect is important since bubbles cannot grow when the channel is narrower than the bubble diameter. In Fig. 2.42 boiling curves 1, 2, and 3 were obtained at Bond numbers 0.185, 0.493, 0.9, respectively. For high Bond numbers, boiling can be considered as almost unconfined. The boiling curve obtained in the present study at $\mathrm{Bn} = 1.52$ did not differ significantly from that obtained by Hetsroni et al. (2002c, 2004b) in pool boiling (unconfined space). For example, at $q = 450\,\mathrm{W/m^2}$ the difference $(T_\mathrm{W} - T_\mathrm{S})$ is close to 21 K for boiling at $\mathrm{Bn} = 1.52$ and pool boiling. However, as the gap size decreased, noticeable decrease in CHF occurred.

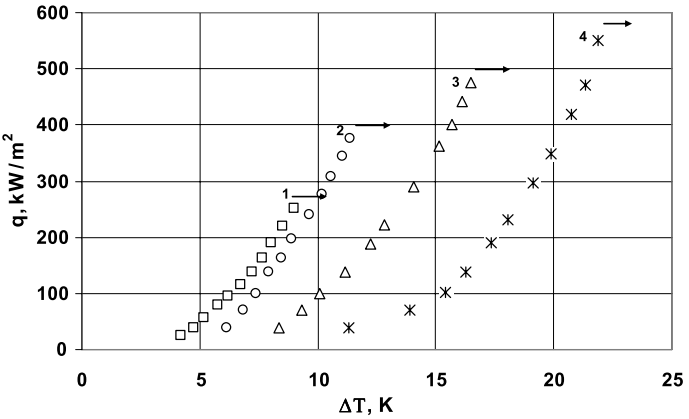

Fig. 2.42 Boiling curves of water in restricted space. *Squares* indicate Bond number Bn = 0.185, *circles* indicate Bond number Bn = 0.493, *triangles* indicate Bond number Bn = 0.9, and last symbol (⚹) indicate Bn = 1.52

Effect of channel length

The experimental values of CHF are plotted in Fig. 2.43 as $q_{\mathrm{CHF}}/q^0_{\mathrm{CHF}}$ versus Bond number, where q^0_{CHF} is the CHF in unconfined pool boiling with the space large enough (Bn $>$ 1.5). The data presented by Hetsroni et al. (2002c, 2004b) were used to calculate the value of q^0_{CHF}. The confined narrow space heavily reduced the CHF as the vapor bubbles have difficulty escaping from the narrow space, especially at larger lengths of the heater surfaces. In a confined space they are able to escape only through the exit. The larger the length of the heater surface, the lower the critical heat flux. Such behavior is in agreement with experimental results described by Katto et al. (1966), Fujita et al. (1988), Bonjour and Lallemand (1988), and Zhao et al. (2002).

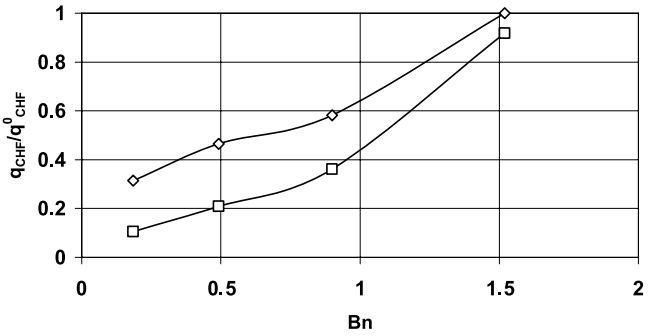

Fig. 2.43 Effect of restriction on CHF. Water boiling. *Diamonds* (◇) indicate $L = 2$ mm, and *squares* indicate $L = 36$ mm. Reprinted from Hetsroni et al. (2007) with permission

Flow in single channel

One of the most widely used correlations for saturated CHF in a single channel is the Katto–Ohno (1984) equation, which in the absence of subcooling reads:

$$\frac{q_{\mathrm{CHF}}}{Gh_{\mathrm{LG}}} = f\left[\frac{\rho_{\mathrm{L}}}{\rho_{\mathrm{G}}}, \frac{\sigma\rho_{\mathrm{L}}}{G^2L}, \frac{L}{d}\right]. \tag{2.15}$$

For most regimes, they found a linear rise in CHF with increasing liquid subcooling. Accordingly, subcooling was taken into account in the following equation:

$$q_{\mathrm{CHF,sub}} = q_{\mathrm{CHF}}\left(1 + K\frac{\Delta h_{\mathrm{in}}}{h_{\mathrm{LG}}}\right) \tag{2.16}$$

where G is mass flux, $q_{\mathrm{CHF,sub}}$ is the CHF for subcooled conditions, q_{CHF} is the saturated CHF, Δh_{in} is the inlet enthalpy of subcooling with respect to saturation, d is the channel diameter, L is the heated length of the channel, and K is an empirical inlet subcooling parameter.

A series of tests were performed by Wojtan et al. (2006) to determine the saturated critical heat flux in 0.5 and 0.8 mm inner diameter micro-channel tubes as a function of refrigerant mass velocity, heated length, saturation temperature and inlet liquid subcooling. The tested refrigerants were R-134a and R-245fa and the heated length of micro-channel varied between 20 and 70 mm. Figure 2.44 shows the evolution of the CHF as a function of mass velocity. All conditions (heated length and temperature of subcooling of refrigerant) were the same for both diameters. As can be seen, the CHF increased with increasing mass velocity. The CHF for the 0.8 mm micro-channel is higher than that for the 0.5 mm one (Fig. 2.45) and the difference (30–50%) becomes greater as the mass velocity increases. The influence of the heated length on the CHF in both micro-tube diameters at constant mass velocity is depicted in Fig. 2.45. The highest CHF was measured for the shortest heated length.

With the heated length for the 0.8 mm diameter tube enlarged from 20 to 70 mm, the drop in the CHF value is $q_{\mathrm{CHF}} = 400\,\mathrm{kW/m^2}$. It confirms that the heated length, besides the mass velocity, is one of the most important parameters in the design of heat sinks.

Figure 2.46 shows the influence of liquid subcooling on the CHF. Only three experimental points are available as measurements at stronger subcoolings proved impossible. On the basis of the limited data, it can be concluded that CHF does not change significantly for the subcooling range $\Delta T = 4.5$ to 12 K. This observation is in agreement with the results of Qu and Mudawar (2004) for micro-channel heat sinks.

Parallel channels

The analysis of experimental data resulted in version of the Katto–Ohno (1984) equation, namely

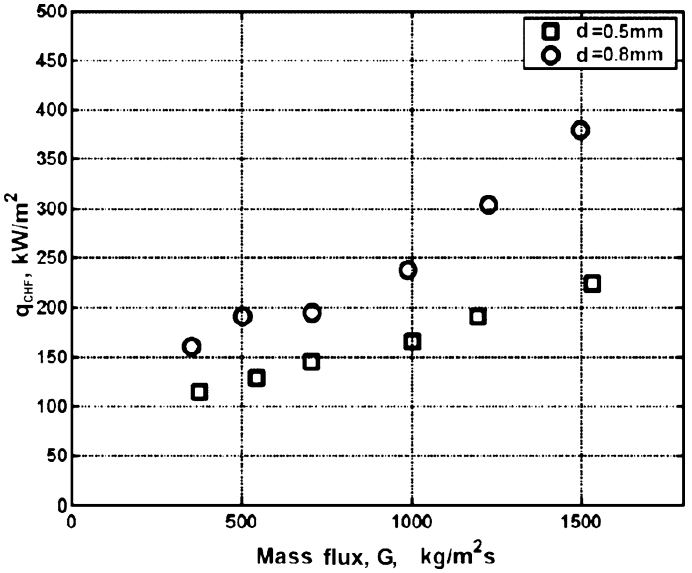

Fig. 2.44 Variation of CHF as a function of the mass velocity in 0.5 and 0.8 mm tubes. R-134a, $\Delta T_{sub} = 8$ K, $T_{sat} = 35\,^{\circ}$C, $L = 70$ mm. Reprinted from Wojtan et al. (2006) with permission

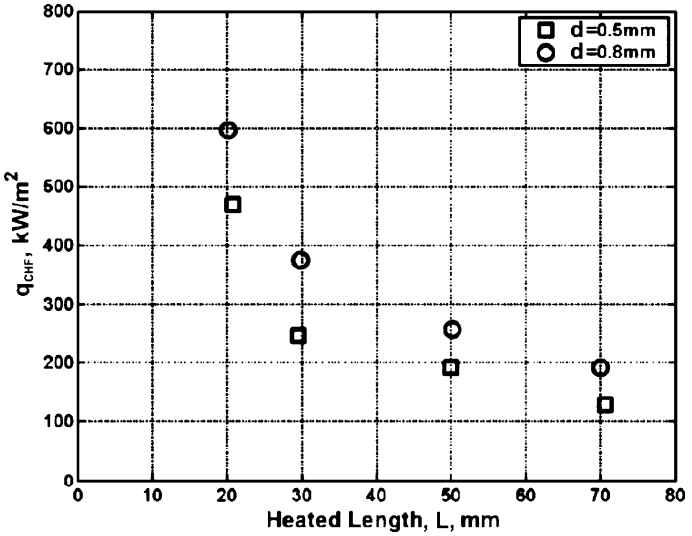

Fig. 2.45 Variation of CHF as a function of the heated length in 0.5 and 0.8 mm tubes. R-134a, $G = 500$ kg/m^{2}s, $\Delta T_{sub} = 8$ K, $T_s = 35\,^{\circ}$C. Reprinted from Wojtan et al. (2006) with permission

$$q_{CHF} = 0.437 \left(\frac{\rho_G}{\rho_L}\right)^{0.073} We_L^{-0.24} \left(\frac{L}{d}\right)^{-0.72} Gh_{LG} \tag{2.17}$$

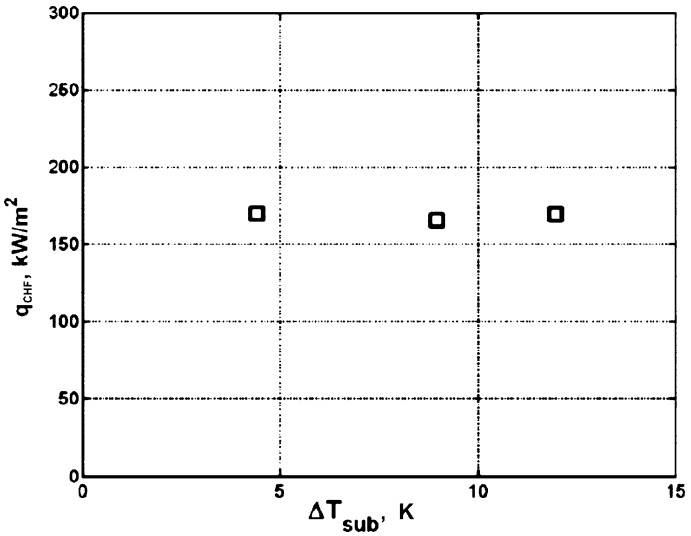

Fig. 2.46 Influence of refrigerant subcooling on CHF. R-134a, $G = 1{,}000\,\mathrm{kg/m^2 s}$, $T_s = 35\,^\circ\mathrm{C}$, $L = 70\,\mathrm{mm}$, $d = 0.5\,\mathrm{mm}$. Reprinted from Wojtan et al. (2006) with permission

The first experimental investigation of the CHF in multi-micro-channels was carried out by Bowers and Mudawar (1994), who tested a cooling element with an array of 17 circular channels, 0.51 mm in diameter, 28.6 mm in length, in a 1.59 mm-thick nickel block, heated over a central 10 mm square section. Boiling curves were generated that terminated in well-defined CHF measurements, which were found to be independent of the liquid subcooling and almost directly proportional to the mass flux, for which a dimensionless correlation was proposed. Jiang et al. (1999b) developed two multi-micro-channel heat sinks integrated with a heater and an array of implanted temperature sensors. There were 58 or 34 channels of rhombic shape, having a hydraulic diameter of 0.040 or 0.080 mm, respectively, in their $10 \times 20\,\mathrm{mm}$ test section. CHF data were taken for once-through water flow entering subcooled at $\Delta T = 20\,\mathrm{K}$. The CHF condition was characterized by a rapid rise in the temperature sensors. The critical power limit was found to be proportional to the total volumetric flow rate. In a recent paper, Qu and Mudawar (2004) reported a comprehensive study of the CHF in rectangular micro-channels. Their heated block contained 21 $0.215 \times 0.821\,\mathrm{mm}$ channels. The heat flux was reported based on the area of the three active sides of the channel. De-ionized, de-aerated water was supplied over a range of $G = 86$ to $368\,\mathrm{kg/m^2\,s}$, with an inlet temperature of 30–60 °C and outlet pressure of 1.13 bar. The dependence of the heat flux on the mass flux is shown in Fig. 2.47 ($q_{\mathrm{p},m}$ is the CHF based on channel heated inside area, $q_{\mathrm{eff},m}$ is the CHF based on the heat sink's top platform area). One can see that the CHF increases monotonically with increasing G for both inlet temperatures. What is quite surprising is that the inlet temperature T_{in} has an insignificant effect on the CHF. Interestingly, these CHF trends relative to the mass flux G and inlet temperature T_{in} mirror

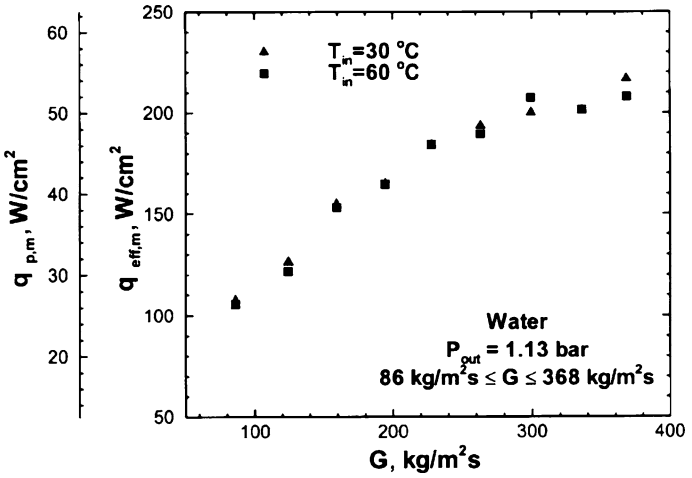

Fig. 2.47 Variation of CHF with mass velocity. Reprinted from Qu and Mudawar (2004)

those of Bowers and Mudawar (1994) for refrigerant R-113 in circular mini- and micro-channel heat sinks. While the trend of increasing CHF with increasing G is quite common, the lack of inlet temperature effect on the CHF seems to be unique to two-phase mini/micro-channel heat sinks, not to single mini/micro-channels. A key difference between these is the aforementioned amplification of parallel channel instability prior to the CHF. As discussed earlier, this amplification causes back flow of vapor into the upstream plenum, which results in strong mixing of the vapor with the incoming liquid. Regardless of how subcooled the incoming liquid, the mixing action appears to increase the liquid temperature close to the local saturation level as it approaches the channel inlet.

The CHF correlation (2.18) was developed by Qu and Mudawar (2004) for water in a rectangular micro-channel heat sink, as well as Bowers and Mudawar's CHF data (1994) for R-113 in a circular mini/micro-channel heat sink.

The following is the CHF correlation:

$$\frac{q_{\mathrm{p},m}}{Gh_{\mathrm{LG}}} = 33.43 \left(\frac{\rho_{\mathrm{G}}}{\rho_{\mathrm{L}}}\right)^{1.11} \mathrm{We}_{\mathrm{L}}^{-0.21} \left(\frac{L}{d_{\mathrm{h}}}\right)^{-0.36} . \tag{2.18}$$

Since the CHF for both mini/micro-channel heat sink databases shows no dependence on inlet subcooling, these databases were correlated without the subcooling multiplier.

Figure 2.48 compares the predictions of this correlation with the flow boiling CHF data for water both in the rectangular micro-channel heat sink (Qu and Mudawar 2004) and in the circular mini/micro-channel heat sinks (Bowers and Mudawar 1994). The overall mean absolute error of 4% demonstrates its predictive capability for different fluids, circumferential heating conditions, channel geometries, channel sizes, and length-to-diameter ratios.

Comparison of the results obtained by Wojtan et al. (2006) and the correlation presented by Qu and Mudawar (2004) is shown in Fig. 2.49. As can be seen there is significant scatter between the respective results. One can conclude that there is a lack of consistency in the reported data.

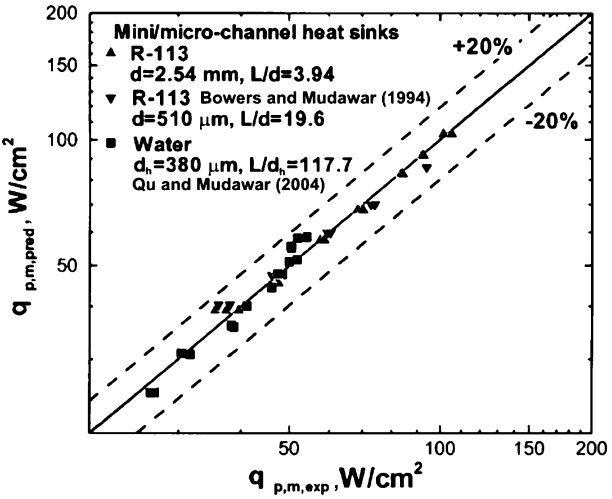

Fig. 2.48 Comparison of CHF data for water and R-113 in mini/micro-channel heat sinks correlation (2.18). Reprinted from Qu and Mudawar (2004) with permission

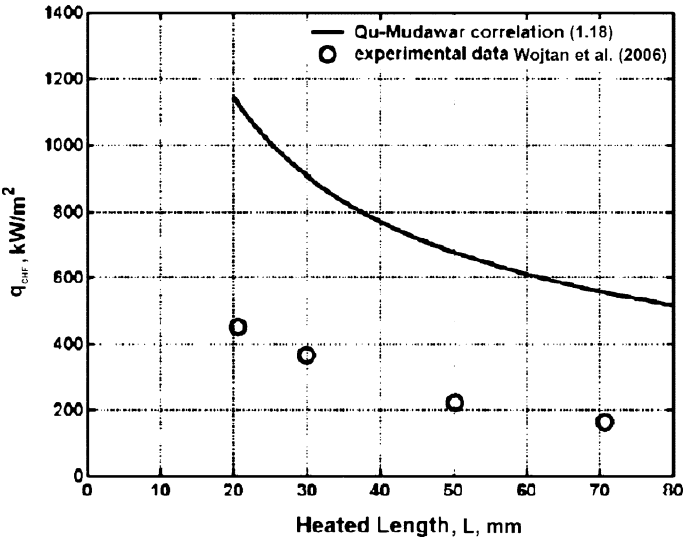

Fig. 2.49 Comparison of the experimental results by Wojtan et al. (2006) to the correlation (2.18) of Qu and Mudawar (2004). R-134a, $G = 500\,\mathrm{kg/m^2s}$, $\Delta T_{\mathrm{sub}} = 8\,\mathrm{K}$, $T_{\mathrm{s}} = 35\,^{\circ}\mathrm{C}$, $d = 0.5\,\mathrm{mm}$. Reprinted from Wojtan et al. (2006)

2.5 Surfactant Solutions

Properties of surfactant solutions: microstructure

The mechanisms that affect heat transfer in single-phase and two-phase aqueous surfactant solutions is a conjugate problem involving the heater and liquid properties (viscosity, thermal conductivity, heat capacity, surface tension). Besides the effects of heater geometry, its surface characteristics, and wall heat flux level, the bulk concentration of surfactant and its chemistry (ionic nature and molecular weight), surface wetting, surfactant adsorption and desorption, and foaming should be considered.

Surfactants have a unique long-chain molecular structure composed of a hydrophilic head and hydrophobic tail. Based on the nature of the hydrophilic part surfactants are generally categorized as anionic, non-ionic, cationic, and zwitterionic. They all have a natural tendency to adsorb at surfaces and interfaces when added in low concentration in water. Surfactant absorption/desorption at the vapor–liquid interface alters the surface tension, which decreases continually with increasing concentrations until the critical micelle concentration (CMC), at which micelles (colloid-sized clusters or aggregates of monomers) start to form is reached (Manglik et al. 2001; Hetsroni et al. 2003c).

Micro-structure of cationic Habon G surfactant solution at CMC concentration ($C = 530$ ppm) is presented in Fig. 2.50 (Hetsroni et al. 2003c). The surfactant solution was examined by direct imaging cryogenic temperature transmission electron microscopy (cryo-TEM). The most common structures are thread-like micelles, shown at high magnification in Fig. 2.50a. Micrographs like this one show quite clearly inner structural details of the micelles (arrowhead). It should be noted that thread-like micelles have been suggested as the one, possibly the most important, micro-structural feature that modifies flow patterns in a flowing fluid and reduces drag (Lu et al. 1998). The drag reduction takes place at values of shear velocity u^* higher than the onset wall shear. The shear velocity is calculated from the pressure drop $u^* = (\tau/\rho)^{0.5}$ (τ shear stress, ρ density). Thus, the drag reducing effect starts with wall shear stresses larger than a threshold value, which depends on the nature of additive and its concentration.

Another feature visible in surfactant solutions is vesicles, denoted by "V" in Fig. 2.50b. These are balloon-like structures made of a double-layer membrane. Such structures are found in many biological and synthetic amphiphiles (Evans and Wennerstrom 1999). In this micrograph we see vesicles co-existing with thread-like micelles (arrows). We have detected junctions between vesicles and thread-like micelles. In fact, three such junctions, one denoted by an arrowhead are seen in the lower left part of the field of view in Fig. 2.50b. The three micelles connecting the three vesicles are connected by a threefold junction seen above the arrowhead. Zheng et al. (2000) hypothesize that the straining actions of flow disrupt vesicles and thus include structural instability of the fragments that leads to their reconstruction into networks of branching thread-like micelles.

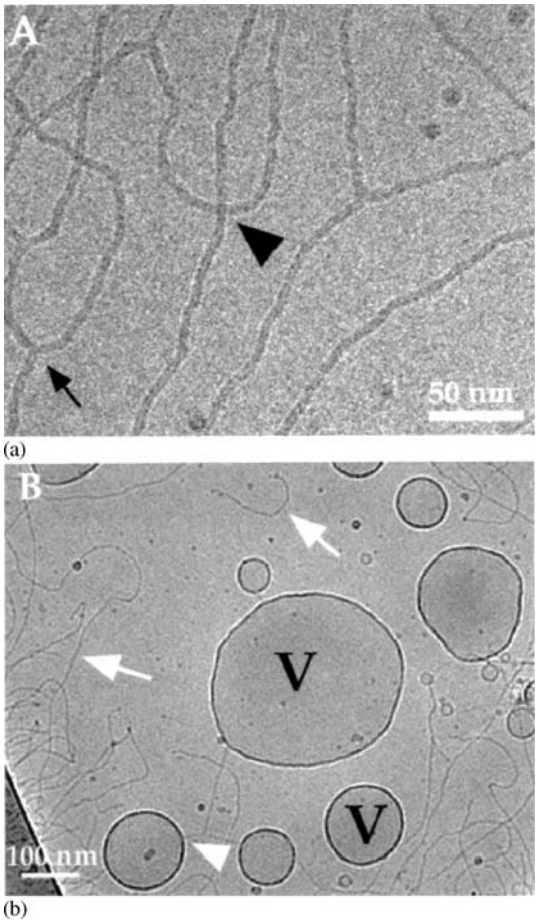

Fig. 2.50a,b Microstructure of the 530 ppm Habon G solution. (**a**) Thread-like micelles and (**b**) vesicles. Reprinted from Hetsroni et al. (2003c) with permission

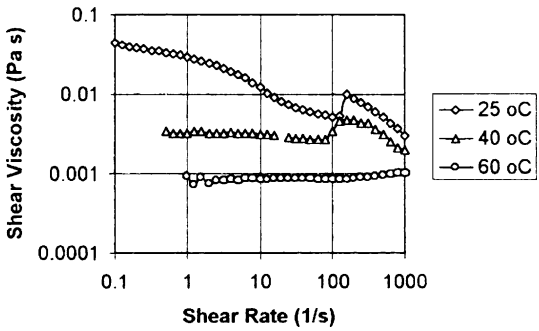

Fig. 2.51 The shear viscosity of 530 ppm Habon G solution vs. shear rate. Reprinted from Hetsroni et al. (2001b) with permission

Viscosity

Viscosity of surfactant solutions depends on the kind of solution, shear rate, temperature and concentration. Figure 2.51 shows the effect of shear rate ϖ on shear

viscosity η for a 530 ppm (parts per million weight) Habon G (the cationic surfactant of molecular weight 500) mixture at different temperatures. The magnitude of the shear viscosity as a function of the shear rate decreases, when the temperature of the solution increases. Moreover, the shear viscosity does not change significantly in the range of the shear rate ϖ=1–1000 1/s at T = 60 °C. Based on this result the kinematic viscosity behavior of Habon G solutions was studied at high shear rates for temperatures of T = 55 °C and above. Figure 2.52 shows the effect of temperature on kinematic viscosity of solutions at various Habon G concentrations. One can see the tendency of viscosity curves to approach that of pure water near the saturation temperature. The saturation temperature of aqueous surfactant solutions in the range of concentration 130 to 1060 ppm did not differ from that of pure water (Hetsroni et al. 2001b).

Thermal conductivity and capacity

Thermal conductivity and capacity of aqueous surfactant solutions in the concentration range 130 to 1,060 ppm did not differ from that of pure water (Hetsroni et al. 2001b). Figure 2.53 shows the dependence of thermal conductivity k on the temperature for $C = 530$ ppm Habon G solution. The value of the thermal conductivity agrees well with that for pure water within the standard deviation of 2%.

Contact angle

The change in surface wettability (measured by the contact angle) with concentration for the three surfactants is plotted in Fig. 2.54 (Zhang and Manglik 2005). The contact angle reaches a lower plateau around the CMC where bilayers start to form on the surface. Wettability of non-ionic surfactants in aqueous solutions shows that the contact angle data attains a constant value much below CMC. Direct interactions of their polar chain are generally weak in non-ionics, and it is possible for them to build and rebuild adsorption layers below CMC. The reduced contact an-

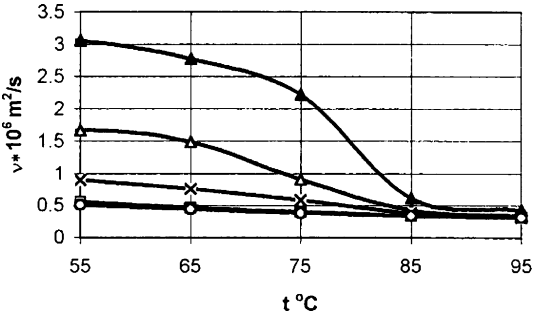

Fig. 2.52 Kinematic viscosity of solution vs. temperature at various Habon G concentrations. *Circles* (○) indicate water; Habon G, *boxes* (□) represent 130 ppm, *crosses* (×) represent 260 ppm, *empty triangles* (△) represent 530 ppm, *filled triangles* (▲) represent 1,060 ppm. Reprinted from Hetsroni et al. (2001b) with permission

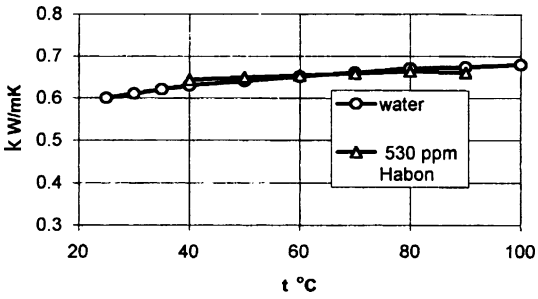

Fig. 2.53 Thermal conductivity vs. temperature. Reprinted from Hetsroni et al. (2001b) with permission

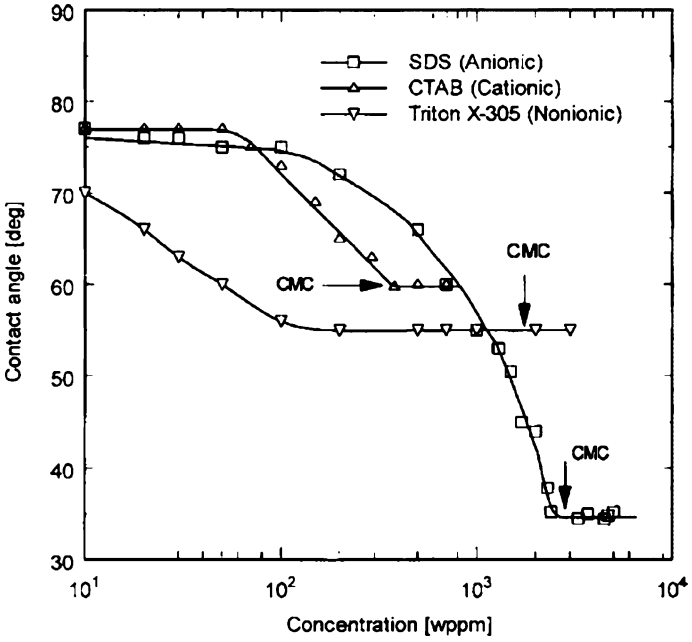

Fig. 2.54 Measured contact angle θ for aqueous surfactant solutions. Reprinted from Zhang and Manglik (2005) with permission

gle at lower concentration ($C < \text{CMC}$) can also be attributed to the absence of any electrical repulsion that could oppose molecular aggregation unlike that associated with ionic surfactants (Zhang and Manglik 2005). Bubble shape is the governing factor in mechanism of bubble growth and motion in nucleate pool boiling. The rapidity of the bubble growth allows the contact angle to deviate from the static value. Figure 2.55 (Hetsroni et al. 2006c) shows time behavior of contact angle for water and non-ionic alkyl (8-16) glucoside aqueous surfactant solution of concentration $C = 600$ ppm.

The results were obtained at heat flux $q = 10\,\text{kW/m}^2$. For both liquids at $t = 1$ ms the contact angle is approximately of $\theta = 60^\circ$, which is very close to the equilibrium surface tension of water. Throughout bubble growth this value decreases approxi-

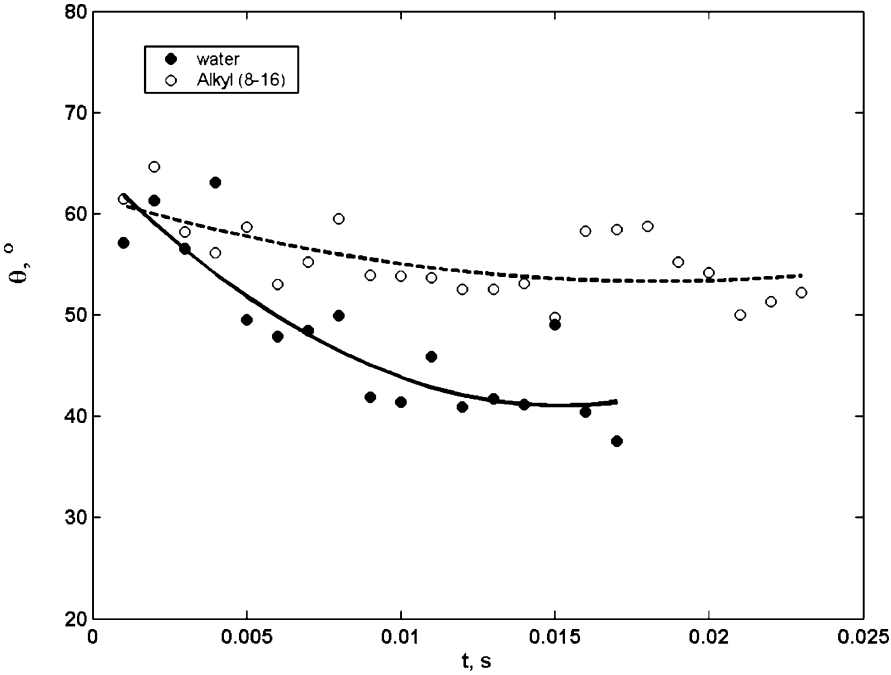

Fig. 2.55 Dependence of contact angle on time, $q = 10\,\mathrm{kW/m^2}$. Reprinted from Hetsroni et al. (2006c) with permission

mately up to 41° and 51° for water and surfactant solution, respectively. The time behavior of the contact angle of a bubble growing in surfactant solution is qualitatively similar to that of water. This in essence explains the time variation of bubble volume for water and surfactant solution shown in Fig. 2.56 (Hetsroni et al. 2006c). A surfactant solution cannot be expected to boil in the same way as a pure liquid even with exactly the same equilibrium surface tension value.

Bubble growth depends on heat flux. With an increase in heat flux, boiling in surfactant solution, when compared with that in pure water, was observed to be more vigorous. Surfactant solution promotes activation of nucleation sites in a clustered mode. This may be due to the retarded bubble coalescence caused by the Marangoni effect of elasticity described by Yang and Maa (2003). The cluster contains a number of small bubbles; the location of the nucleation sites and time behavior cannot be traced exactly. Dependence of a single bubble in water and a single bubble located in the cluster of non-ionic alkyl (8-16) glucoside aqueous surfactant solution of 600 ppm concentration at heat flux $q = 50\,\mathrm{kW/m^2}$ is shown in Fig. 2.57 (Hetsroni et al. 2006c). Analysis of the curves in Fig. 2.57 shows that the growth of bubbles in surfactant solution at high heat flux occurs slower than in water.

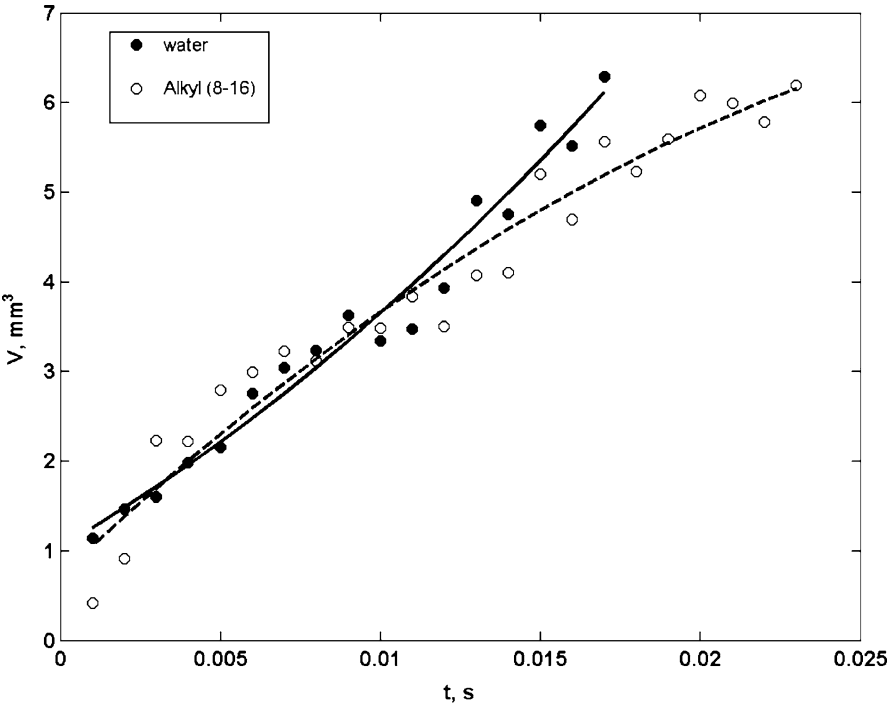

Fig. 2.56 Dependence of bubble volume on time, $q = 10\,\mathrm{kW/m^2}$. Reprinted from Hetsroni et al. (2006c) with permission

Surface tension

In Fig. 2.58 (Hetsroni et al. 2001b) the dependencies of the surface tension of the various surfactants σ divided on the surface tension of water σ_w are shown. One can see that beginning from some particular value of surfactant concentration (which depends on the kind of surfactant), the value of the relative surface tension almost does not change with further increase in the surfactant concentration. It should be emphasized that the variation of the surface tension as a function of the solution concentration shows the same behavior for anionic, non-ionic, and cationic surfactants at various temperatures.

For example, for alkyl (8-16) glycoside (Plantacare 818 UP) non-ionic surfactant solution of molecular weight 390 g/mol, an increase in surfactant concentration up to 300 ppm (CMC concentration) leads to a significant decrease in surface tension. In the range $300 \leq C \leq 1{,}200$ ppm the surface tension was almost independent of concentration. In all cases an increase in liquid temperature leads to a decrease in surface tension. This surface tension relaxation is a diffusion rate-dependent process, which typically depends on the type of surfactant, its diffusion/absorption kinetics, micellar dynamics, and bulk concentration levels. As the CMC is approached the absorption becomes independent of the bulk concentration, and the surfactant

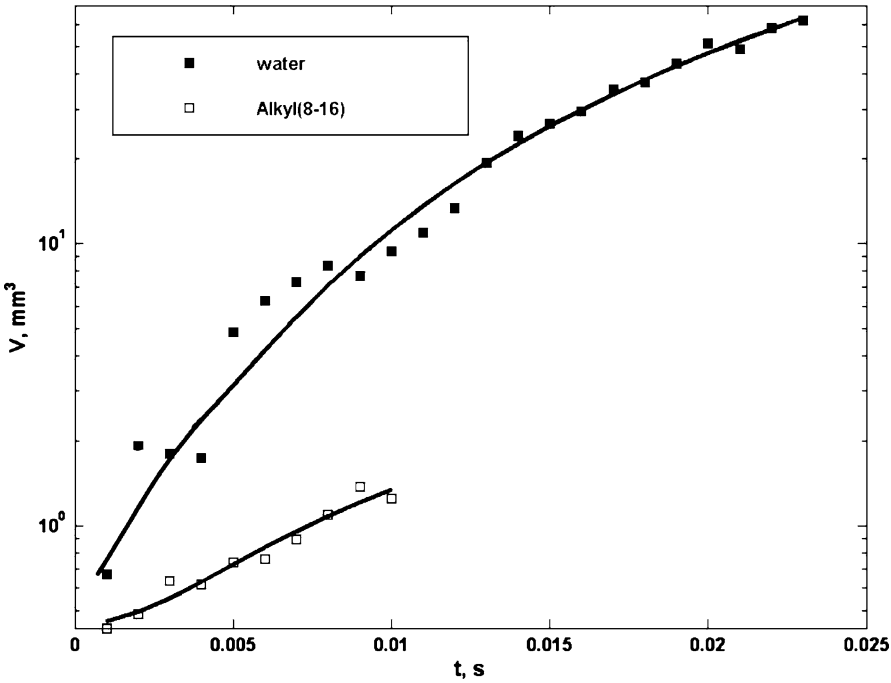

Fig. 2.57 Dependence of bubble volume on time, $q = 50\,\mathrm{kW/m^2}$. Reprinted from Hetsroni et al. (2006c) with permission

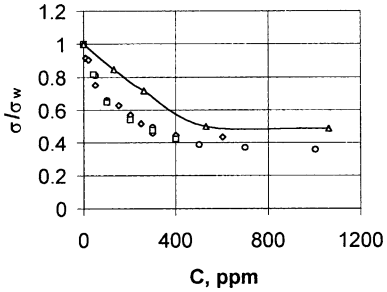

Fig. 2.58 The non-dimensional surface tension of various surfactants vs. solution concentration. *Diamonds* (◇) represent SDS (Wu et al. 1995), $T = 25\,^{\circ}\mathrm{C}$. Circles (○) represent SDS (Tzanand and Yang 1990), $T = 25\,^{\circ}\mathrm{C}$. Squares (□) represent SDS (Wu and Yang 1992), $T = 100\,^{\circ}\mathrm{C}$. Triangles (△) represent Habon G (Hetsroni et al. 2001b), $T = 70\,^{\circ}\mathrm{C}$. Reprinted from Hetsroni et al. (2001b) with permission

molecules form a bilayer on the surface to make it strongly hydrophilic (Zhang and Manglik 2005). The heat transfer in saturated nucleate boiling of aqueous surfactant solutions generally increases with increase in heat flux and additive concentration up to $C \leq$ CMC. With $C >$ CMC, the enhancement decreases and the heat transfer can even deteriorate. It should be emphasized that the variation of the non-dimensional

surface tension as a function of the surfactant concentration shows the same behavior for various temperatures. The normalized nucleate boiling heat transfer coefficient may be related to normalized surface tension of the surfactant solution. We used the magnitude of surfactant characteristic concentration C_0 where the change of relative surface tension reaches 90% of the complete change to normalize the concentration scale. The values $C_0 = 530$ and 700 ppm were chosen for Habon G and SDS solutions, respectively.

For normalization of the value of the heat transfer enhancement, we used its magnitude at the maximum for each curve. The result of such normalization is shown in Fig. 2.59. In this figure, C is the solution concentration, C_0 is the characteristic concentration, h is the heat transfer coefficient at given values of the solution concentration and the heat flux q, $h_{\max}$ is the maximum value of the heat transfer coefficient at the same heat flux, and h_w is the heat transfer coefficient for pure water at the same heat flux q. Data from all the sources discussed reach the same value of 1.0 at the magnitude of relative surfactant concentration equal to 1.0.

Thus, the enhancement of heat transfer may be connected to the decrease in the surface tension value at low surfactant concentration. In such a system of coordinates, the effect of the surface tension on excess heat transfer $(h - h_w)/(h_{\max} - h_w)$ may be presented as the linear fit of the value C/C_0. On the other hand, the decrease in heat transfer at higher surfactant concentration may be related to the increased viscosity. Unfortunately, we did not find surfactant viscosity data in the other studies. However, we can assume that the effect of viscosity on heat transfer at surfactant boiling becomes negligible at low concentration of surfactant only. The surface tension of a rapidly extending interface in surfactant solution may be different from the static value, because the surfactant component cannot diffuse to the absorber layer promptly. This may result in an interfacial flow driven by the surface tension gradi-

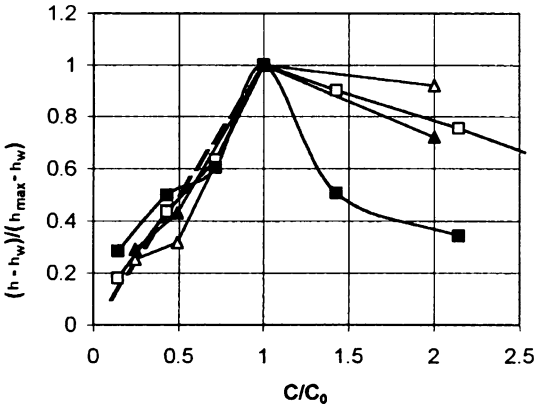

Fig. 2.59 The excess heat transfer coefficient vs. the surfactant concentration. For Habon G *empty triangles* (△) represent $q = 400\,\mathrm{kW/m^2}$, and *filled triangles* (▲) represent $q = 800\,\mathrm{kW/m^2}$. For SDS (Wu and Yang 1992) *empty squares* (□) represent $q = 350\,\mathrm{kW/m^2}$, and *filled squares* (■) represent $q = 400\,\mathrm{kW/m^2}$. Reprinted from Hetsroni et al. (2001b) with permission

ent (known as Marangoni flow). Phase change during boiling is a local phenomenon that is associated with the heat transfer and hydrodynamics in the vicinity of a growing vapor bubble. The concentration sublayer also determines the dynamic surface tension at the interface, which in turn directly influences the bubbly dynamics.

For pool boiling Wasekar and Manglik (2002) presented the results of a study that investigates the dependence of nucleate boiling heat transfer coefficients of aqueous surfactant solutions of different molecular weight and ionic nature. It was reported that the maximum enhancement increased with decreasing surfactant molecular weight. The criteria for nucleate boiling enhancement by surfactant additives was proposed by Yang and Maa (2003). As the first criterion, it was postulated that the surfactant should be soluble in water. As the second criterion, it was postulated that the surfactant should depress the equilibrium surface tension of solution significantly. As the third criterion, it was postulated that the surfactant should not depress the equilibrium contact angle significantly. According to Yang and Maa (2003), boiling heat transfer by addition of surfactant is enhanced by the depression of the equilibrium surface tension but suppressed by the depression of the equilibrium contact angle. Sher and Hetsroni (2002) developed a model of nucleate pool boiling with surfactant additives. Solid–vapor, solid–liquid and liquid–vapor surface tensions were assumed to be surfactant diffusion controlled, and the boiling curves were calculated. To the author's best knowledge no discussion on effect of channel gap size on natural convection boiling was found.

Additive of surfactant leads to enhancement of heat transfer compared to water boiling in the same gap size; however, this effect decreases with decreasing channel size. For the same gap size CHF in surfactant solutions is significantly lower than that in water. At high values of heat flux some foaming patches began to occur; this process increased with decrease in gap size and led to decrease in CHF, Hetsroni et al. (2007).

2.6 Design and Fabrication of Micro-Channel Heat Sinks

Typical channels studied in literature are rectangular, with one side unheated (usually a transparent cover plate in the experimental apparatus) and heat is applied near the opposite wall. Bergles et al. (2003) considered the general geometry, permitting relative simplicity in the vertical dimension, shown in the sketch of Fig. 2.60: a right parallelepiped heated (uniformly) on one side, and perforated by one or more rows of identical channels parallel to the heated surface. The system can be treated as a stack of plates, some with slots for the channels and some solid. Several possible patterns and channel sizes (d, d_i, ...) are shown for illustration, although in the following we shall assume that only one channel pattern is used in any particular case. The channels may be connected at the ends to form flow lengths of $L = 2W$, $3W$, or more, or divided at mid-block to form lengths of $L = W/2$, $W/3$, or less. Let the ratio of channel length to block width be $r = L/W$.

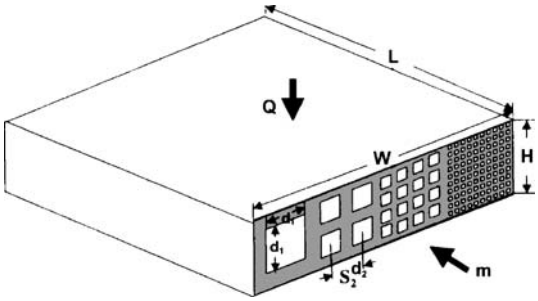

Fig. 2.60 Geometry of microchannel heat sink. Reprinted from Bergles et al. (2003) with permission

General problem

The design question is: given the heat rate Q, the length L, and width W, select a working fluid with mass flow rate m, channel dimension d, channel spacing $S \times d$ (for S is a number > 1), number of channels n, and material and thickness of the block H. We will be particularly interested in the pumping power P.

The width and thickness of the block, and the number, length, diameter, and spacing of the channels are not independent. The geometric configuration requires that the number of channels in a row, n_c, be

$$n_c = \frac{W}{Sd} \tag{2.19}$$

and that the number of rows be

$$n_r = \frac{H}{Sd}\,. \tag{2.20}$$

The total number of holes in a cross-section, which is the number of channels, is

$$n = n_c n_r = \frac{WH}{(Sd)^2} \tag{2.21}$$

and the total length of all channels

$$nL = nrW = r\frac{HW^2}{(Sd)^2}\,. \tag{2.22}$$

The number n must be an integer (i.e., $n = 1, 2, 3, \ldots$) and channel flow is characterized by lengths that are at least several diameters in magnitude. The latter constraint does not preclude operation in the "entry length" mode.

In a phase-change controlled thermal management system, the energy associated with phase change will account for most of the heat removal

$$Q = m\Delta\chi h_{LG} \tag{2.23}$$

where $\Delta\chi$ is the change in quality over the length of the channel and h_{LG} is the latent heat of vaporization for the coolant. For applications where the entire channel is in the subcooled boiling mode, there would be no change in equilibrium quality. In this case, the total heat removal might be on the order of that needed to bring the coolant to saturation temperature:

$$Q \approx mc_{\mathrm{p}}(T_{\mathrm{s}} - T_{\mathrm{sub}}) \tag{2.24}$$

where C_{p} is the specific heat of the liquid coolant, T_{s} the saturation temperature, and T_{sub} the inlet temperature of the subcooled coolant. Given a desired value of $\Delta\chi$ (low or high) or of $(T_{\mathrm{s}} - T_{\mathrm{sub}})$, Eq. (2.23) or (2.24) can be used to get a first estimate for the mass flow rate of the coolant at the system pressure. From the overall energy balance for square channels with sides of length $d_1 = d_2 = d$, we obtain

$$Q = 4dnLq = \frac{4rHW^2}{S^2 d} q \tag{2.25}$$

where q is the average heat flux at the channel wall. In the case of circular channels of the same diameter d, π replaces the number 4 in this equation.

The average heat flux must be less than the critical value q_{CHF} for the flow, in order to avoid excessive temperatures in the solid

$$q < q_{\mathrm{CHF}}\,. \tag{2.26}$$

It is important to note here that the CHF depends on the flow conditions, including the mass flux and the vapor quality. Using Eq. (2.25) to eliminate q, we find

$$q_{\mathrm{CHF}} > \frac{QS^2 d}{4rHW^2}\,. \tag{2.27}$$

For the lower heat transfer surfaces in Fig. 2.60 to contribute to the energy transport, the solid should be an effective conductor of heat through its thickness. In other words, conjugate heat transfer effects should not create a more significant resistance to heat flow than that of the fluid in the channel. Since the heat transfer coefficient is generally a maximum at CHF, this leads to

$$\frac{k_{\mathrm{solid}}(S-1)}{4H} \gg \frac{q_{\mathrm{CHF}}}{(T_{\mathrm{CHF}} - T_{\mathrm{s}})} > \frac{q}{(T_{\mathrm{CHF}} - T_{\mathrm{s}})} \tag{2.28}$$

where k_{solid} is the thermal conductivity of the solid, and T_{CHF} and T_{s} are the wall temperature at critical heat flux and the saturation temperature of the fluid, respectively. Substituting Eq. (2.25) in Eq. (2.28), we obtain

$$\frac{k_{\mathrm{solid}}(S-1)}{H} \gg \frac{Q}{rnLd\,(T_{\mathrm{CHF}} - T_{\mathrm{s}})} \tag{2.29}$$

Note that a good design will be one in which the pumping power P is small compared to the heat removal rate Q:

$$P \ll Q \tag{2.30}$$

Non-uniform temperature distribution

One drawback of a micro-channel heat sink is a relatively high temperature rise along the micro-channel compared to that for the traditional heat sink designs. In the direction of the flow, the wall temperature rises in a single-phase flow even when the wall heat flux is uniform. In a micro-channel heat sink, the large amount

of heat generated by the electronic device is removed from the package by a relatively small amount of coolant, which exits at a relatively high temperature. The large temperature rise produces thermal stresses in the elements and packages due to the differences in the coefficient of thermal expansion, thus undermining the device's reliability. This temperature rise may be accompanied by a complex pattern of spatial variations that can produce potentially destructive thermal stresses along the interface between the chip and the substrate or heat sink. This is one of the key justifications for seeking a nearly isothermal heat sink. Furthermore, a large temperature gradient is undesirable for the electronic performance, since many electronic parameters are adversely affected by it. One example is electrical-thermal instability because the basic elements of electronic circuits have a switching time that decreases with increasing temperature.

The surface of ultra large-scale integrated circuits (ULSI), from which the heat should be transferred, may be heated by a uniform heat flux, and more often by a non-uniform one. Even in the former case the temperature of the cooled surface is not uniform, but is determined by the heat transfer coefficients along the surface and in the spanwise direction.

We have designed, manufactured and tested a prototype that may be applied in thermal control of electronic devices. It was fabricated from a silicon substrate and a Pyrex cover, serving as both an insulator and a window through which flow patterns and boiling phenomena could be observed. A number of parallel triangular micro-channels were etched in the substrate. The heat transferred from the device was simulated by different types of electrical heaters that provided uniform and non-uniform heat fluxes, defined here respectively as constant and non-constant values

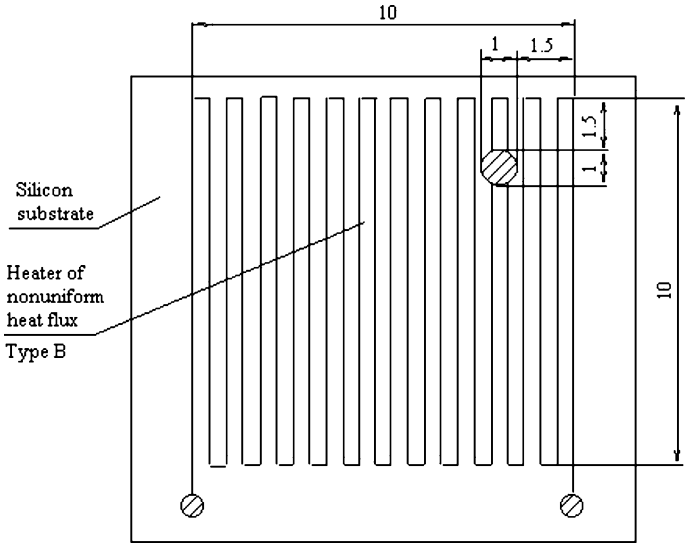

Fig. 2.61 Type of heater providing non-uniform heat flux. Reprinted from Hetsroni et al. (2001a) with permission

on the heated wall (HW). (In reality no heater can generate a really uniform heat flux, because of the concentration effects of the micro-channel geometry.)

In Fig. 2.61 the part of the heater, with a diameter of 1 mm, has the electrical resistance of 20% less than the average one (Hetsroni et al. 2001a).

For triangular micro-channels of $d_h = 130\,\mu m$ results based on experimental measurements at the same entrance flow rate $m = 0.046\,g/s$ are presented in Figs. 2.62 and 2.63.

The measurements performed in the heat flux range from 90 to $220\,kW/m^2$ showed that for all module types tested, the irregularity of $T_{w,max}$ across the heated bottom, increases with the increase of heat flux. This effect is more marked under boiling conditions. At uniform heat flux the irregularity of $T_{w,max}$ exceeds 20 K (Fig. 2.62). In the non-uniform heat flux case (average value $q = 220\,kW/m^2$), the irregularity exceeds 60 K (Fig. 2.63).

The temperature distribution in the flow direction for a fixed flow rate differs for different devices. This suggests that the heat transfer mechanism in these devices is not identical. The non-uniform (of about 20%) heat flux leads to conditions at which the wall temperature increases sharply. Idealizing the heat flux as uniform can result in a significant error in prediction of the temperature distribution.

Manifolds

Several studies (Klein et al. 2005; Mishan et al. 2007) showed that manifold design plays an important role in the liquid distribution among parallel micro-channels, which can lead to spanwise temperature gradients on the device surface, increase the thermal stresses and reduce reliability. To study the effect of entrance conditions

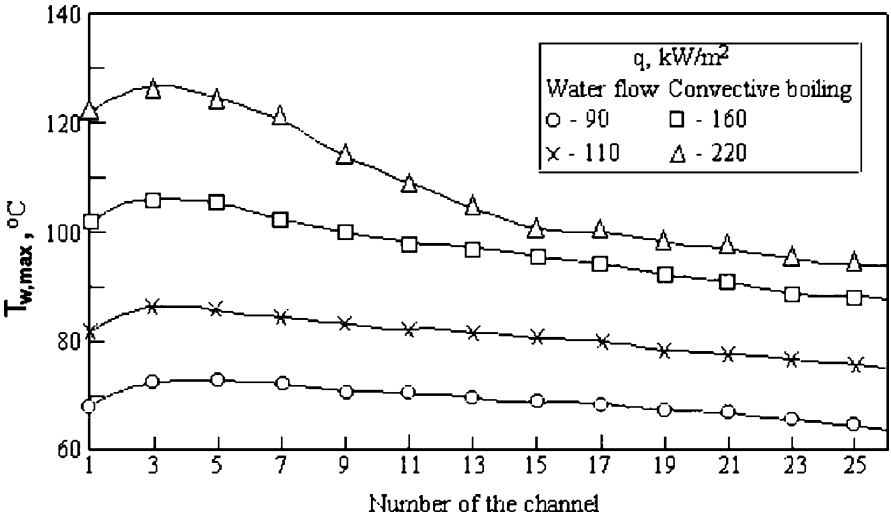

Fig. 2.62 Spanwise irregularity of maximum temperature on HW. Uniform heat flux. Reprinted from Hetsroni et al. (2001a) with permission

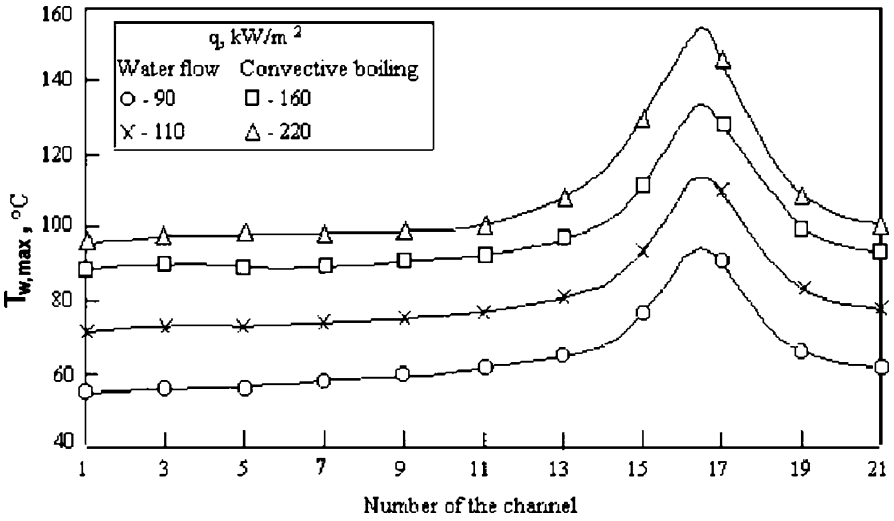

Fig. 2.63 Spanwise irregularity of maximum temperature on HW. Non-uniform heat flux. Reprinted from Hetsroni et al. (2001a) with permission

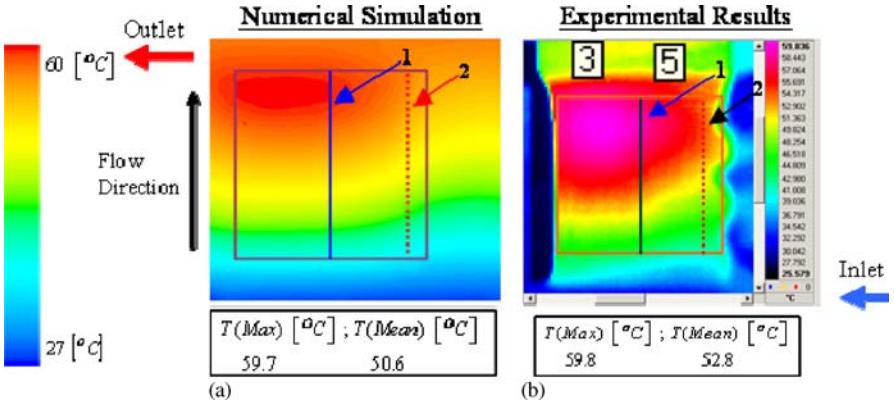

Fig. 2.64a,b Temperature field on heater. Reprinted from Mishan et al. (2007) with permission

on the temperature of the heater calculations using CFD software were conducted (Tiselj et al. 2004; Mishan et al. 2007). Developing heat transfer and fluid flow were investigated experimentally on rectangular micro-channels of $D_h = 440\,\mu m$, with water as working fluid. The experimental results were compared with theoretical predictions from literature and data obtained by numerical modeling of the present experiment. The experimental results of pressure drop and heat transfer confirm that including the entrance effects, the conventional theory is applicable for water flow through micro-channels. Figure 2.64 shows a typical temperature distribution on the heater. The fluid moves from the bottom to the top, the heat flux is $q = 4.4\,W/cm^2$ and the mass flux is $G = 8.33\,kg/m^2\,s$. The figure presents a comparison between

the temperature field of the heater obtained from the numerical simulation (A) and that obtained from IR measurements (B). The square enclosed area of $10 \times 10\,\text{mm}^2$ represents the heater. Both of the pictures show very close temperature distributions. Figure 2.65 shows the temperature distribution along the central and side lines, marked as lines 1, 2, respectively, in Fig. 2.64. Numerical and experimental results agree quite well.

To optimize the design of the manifold configuration, a number of numerical calculations were conducted for three types of manifolds shown in Fig. 2.66. Figure 2.67 shows the velocity distribution at 2 mm from the inlet to the microchannels, from which one can conclude that configuration 1 and 2 ensure uniform velocity distribution at the entrance.

It was shown that data presented by other researchers can be carried over to entrance effects. The present results highlight the importance of accounting for com-

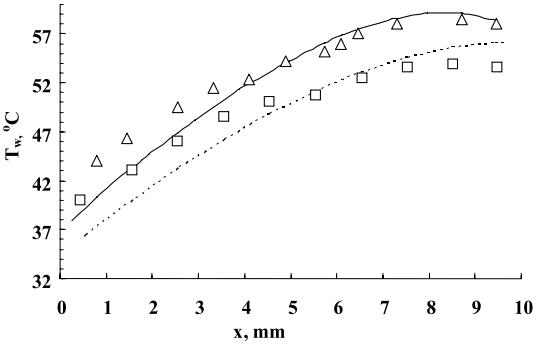

Fig. 2.65 Comparison between numerical simulation and experimental results for the temperature field on the heater surface. The *solid line* represents simulation, and *triangles* (△) experimental results (line 1 in Fig. 2.64); *dotted line* represents simulation, and *squares* experimental results (line 2 in Fig. 2.64). Reprinted from Mishan et al. (2007) with permission

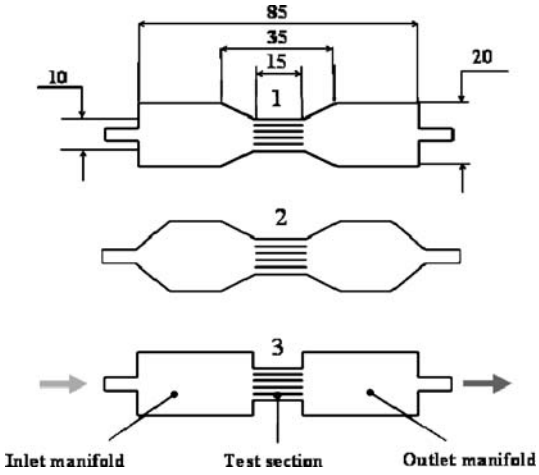

Fig. 2.66 Types of manifolds used for calculations. Reprinted from Mishan et al. (2007) with permission

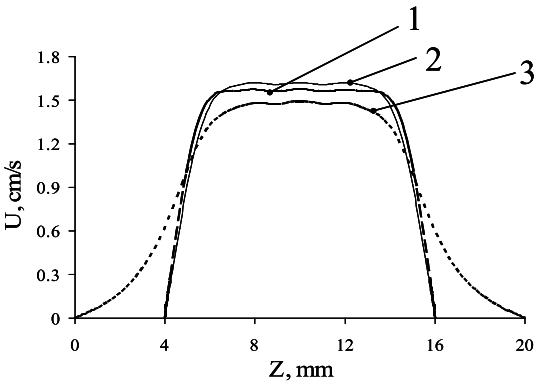

Fig. 2.67 Velocity profile at micro-channel entrance. Manifolds: *1* type 1, *2* type 2, *3* type 3. Reprinted from Mishan et al. (2007) with permission

mon phenomena that are often negligible in standard flows, such as profile of inlet velocity, axial heat conduction, and design inlet and outlet.

Optimization

The object of this optimization is minimization of the unit's overall thermal resistance, at a fixed pumping power per unit area. For a micro-channel heat sink, the thermal resistance consists of conduction resistance, convection resistance and bulk resistance due to the bulk temperature rise of the coolant. Since the micro-channel heat sink is typically thin and the materials used, such as silicon, have very high thermal conductivity, the conduction resistance is normally a small part of the overall resistance. As the channel size decreases, for a fixed pressure drop or pumping power, the convection resistance also decreases because the Nusselt number remains constant. However, the bulk resistance increases because now the flow rate decreases. Therefore there is an optimum channel dimension. If the pumping power is not limited, there is no optimum aspect ratio since the larger the aspect ratio, the better the convective heat transfer. With the constraint of pumping power, however, the aspect ratio cannot be indefinitely increased because the fluid flowing near the fin tip does not remove any heat at very high aspect ratios. Assuming fully developed conditions, Bau (1998) conducted an optimization study to minimize the temperature gradient and the overall thermal resistance. It was demonstrated that further reductions in overall thermal resistance and temperature gradient could be achieved by varying the cross-sectional dimensions of the micro-channel. Another optimization study by Knight et al. (1992) reported that at the optimal configuration, the thermal resistance for the Tuckerman and Pease device (1981) could be reduced by 35% if turbulent flow is allowed. However, the required pumping power is almost five times higher. Phillips (1990) provided an analytical model to estimate the thermal resistance of a micro-channel, whose results were compared with measurements and showed very good agreement. Weisberg et al. (1992) analyzed a micro-channel heat exchanger by numerical simulation of the heat transfer in the fluid and the solid substrate. Several assumptions made in the previous research were examined and found to be

valid in this study. The manifold micro-channel heat sink was first proposed by Harpole and Eninger (1991) and numerically studied in Copeland et al. (1997) and Ng and Poh (1999). Unlike a conventional micro-channel heat sink, the manifold type features many inlet and outlet manifolds, alternating at a periodic distance along the length of the micro-channel. It is expected to have a smaller pressure drop compared with its conventional counterpart for a fixed flow rate. Gillot et al. (1998) evaluated thermal performance of micro-channel heat sink for a multi-chip power module. A prototype demonstrated the capability of dissipating 230–350 W/cm with a temperature rise of 35 °C. The overall thermal resistance can be reduced by increasing the pumping power. However, this can be costly in terms of the micro-pump requirement. Another way to reduce thermal resistance is to increase the heat transfer area. For a substrate with fixed area, one way to increase the heat transfer area is to use a heat spreader and then attach a heat sink to the spreader. This is commonly used in cooling of the central processing unit in a computer. The area increase in this case is achieved in the plane of the substrate. The stacked micro-channel analyzed here increases the heat transfer area in the out-of-plane direction. The uniqueness of such a design is that a heat spreader is not required. Wei and Joshi (2000) evaluated the thermal performance of stacked micro-channel heat sinks (schematic shown in Fig. 2.68). At each layer, a number of parallel micro-channels are machined in the surface of a substrate, e.g., copper, silicon or diamond. These layers are then bonded into a stacked micro-heat exchanger.

It was demonstrated that for a fixed pumping power, the overall thermal resistance for a two-layered micro-channel stack is 30% less than for a one-layered micro-channel due to doubling of the heat transfer area. Methods for optimizing the thermal performance of micro-channel heat sinks were discussed by Kim (2004).

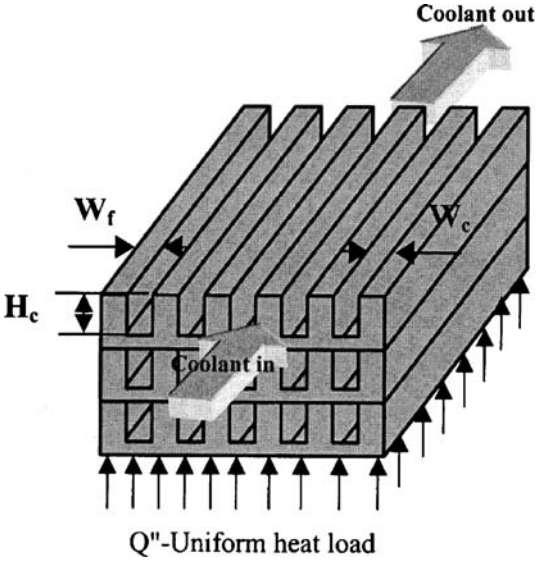

Fig. 2.68 Three-dimensional stack of micro-channels. Reprinted from Wei and Joshi (2000) with permission

These include analytical models (fin and porous medium) and a three-dimensional numerical approach. The fin model is based on the assumption of unidirectional conduction, constant heat transfer coefficient, and uniform fluid temperature, while the porous medium model is based on volume averaging of the velocities and temperatures in the direction perpendicular to the flow. From the optimization of a micro-channel heat sink, which minimizes the total thermal resistance under the constraint of a maximum pumping power, the optimal values of channel height, channel width, and fin thickness are presented. In order to check the validity of the analytical models, the temperature distributions from the two analytical models are compared with those from the numerical simulation. The assumption of unidirectional conduction, and the local volume-averaging technique, are shown to be justified, whereas the assumption of constant heat transfer coefficient with reference to the bulk mean temperature is invalid for large values of the aspect ratio. This latter assumption, combined with incorrect values of fin efficiency, may result in errors in the thermal design if the aspect ratio is larger than eight. Because of this defect, the fin model fails to provide the design variables.

It is noteworthy that several studies exhibit contradictory results for both the mechanical and thermal characteristics of the flow. This is generally due to differences in the many parameters that characterize these studies such as the geometry, shape and surface roughness of the channels, the fluid, the boundary conditions and the measuring methodology itself. These discrepancies indicate the need for extension of the experimental base to provide the necessary background to the theoretical model.

In the past few years, Bar-Cohen and co-workers documented an extended series of heat sink design and optimization studies aimed at achieving the highest energy efficiency for high-performance heat sinks (Bahadur and Bar-Cohen 2005; Bar-Cohen et al. 2006). In their work they introduced an approach involving a new metric, called the total coefficient of performance (COPT), which namely is the ratio of the heat removed by the sink to the total invested work, including both the pumping power and energy content of the heat sink. They successfully demonstrated the suitability of this approach for air-cooled heat sinks, and found that for a wide parametric range, the most energy efficient heat sink design involves use of "least material" optimum fins. This technique has yet to be applied to liquid-cooled heat sinks, where much higher heat transfer coefficients and heavier pumping power losses than experienced in air-cooled heat sinks will be encountered. Extension of this design and optimization methodology to high-performance micro-channel coolers can be expected to dramatically improve the energy efficiency of these thermal management devices and establish the broad applicability of the COPT approach.

A typical example of calculation of the thermal coefficient of performance for forced convection of air is shown in Fig. 2.69. COP surfaces are presented for the maximum and least material aluminum heat sink configurations in the design flow space between 0.01–0.04 m^3/s and 20–80 Pa.

These upper-bound COP values for maximum thermal performance aluminum arrays are seen to approach remarkably high values of nearly 1000 and provide

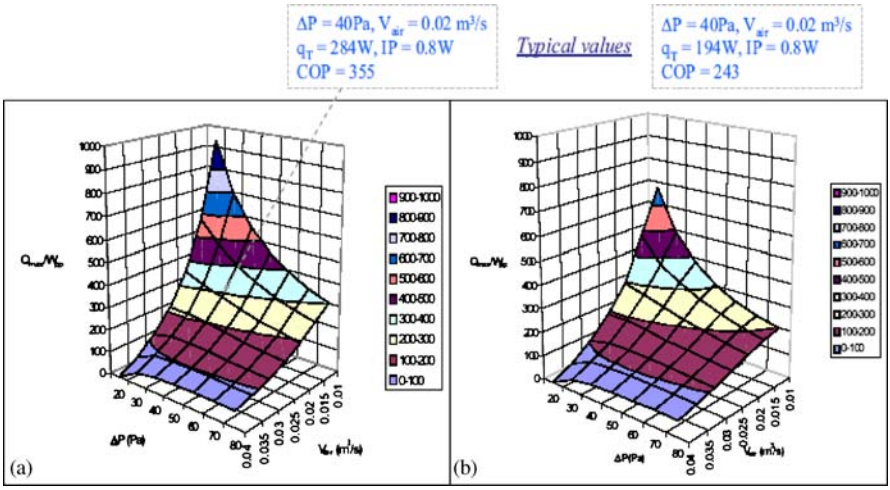

Fig. 2.69a,b Coefficient of performance for aluminum plate fin array in forced convection (**a**) maximum heat transfer design, and (**b**) least material design. Reprinted from Bar-Cohen et al. (2006) with permission

a broad range of flow rate/pressure head combinations with COPs above 300. Predictably, the least material configurations – in which some thermal performance is sacrificed in favor of significant mass reduction – offer lower, though still remarkably high COP values, peaking at nearly 700, with a broad range of options for attaining COP values above 200. It should be noted that for the maximum, as well as least material heat sinks, the peak COPs occur at the lowest values of pressure drop and flow rate and then decrease rather steeply with increasing volumetric flow rate and heat sink pressure drop.

Fabrication technique

The earliest micro-channels were built using anisotropic wet chemical etching techniques based on alkaline solutions. Recently, anisotropic dry processes have been developed. These are significantly faster and, from the manufacturing standpoint, involve fewer contamination and waste treatment problems. Some fabrication areas that may spur advances include new materials, high-aspect ratio patterning techniques other than dry etching, active fluid flow elements, and micro-molding. Miniaturized traditional techniques are in some respects the most straightforward approach to creating micro-channels. Saw cuts on the order of 25 μm width with accuracy of 4 μm can be obtained with commercially available equipment. Micro-discharge-electromachining has been demonstrated, using very fine wires as electrodes. Other cutting techniques such as ultrasonic and water jet machining are especially effective on hard brittle materials. Laser machining has become a powerful tool that can handle a wide variety of difficult materials. Focused ion beam machining offers many similar benefits and can operate in the submicron regime.

A review of micro-channel fabrication technology was published by Kandlikar and Grande (2002). In many cases silicon is the substrate of choice for reasons of cost and process compatibility. The etching can be carried out in either a wet chemical or dry plasma format, and both techniques have isotropic and anisotropic variants (Bean 1978; Bhardwaj et al. 1997). Anisotropic wet chemical etching (WCE) (using potassium hydroxide or ethylene diamine pyrocatechol) can produce specific micro-channel device designs. In most cases triangular micro-channels may be created with a 54.74° angle to the surface. Isotropic wet chemical etching (using hydrofluoric acid, nitric acid, and acetic acid) results in hemispherical etch profiles. Another constraint of anisotropic WCE is that features formed by the intersection of planes are stable only where the corner angle is less than 180°. A recent advance in etch technology are deep reactive ion etch processes (DRIE), which can produce vertical etch profiles in silicon. Figure 2.70 shows a set of micro-channels with 42 μm trenches etched to more than 100 μm. Bulk micro-machining etch processes are summarized in Fig. 2.71. Etch techniques can be combined in unique ways to create complex micro-channel structures. Figure 2.72 schematically illustrates a process that can create micro-channels buried inside a wafer. It is also possible to build sets of micro-channels at different depths and have them cross over one another. The micro-channels with hydraulic diameters in the range of 1.01 to 35.91 μm and length of 10–11 cm were fabricated using photolithography and wet etching techniques (Harley et al. 1995).

A class of very high-aspect ratio fabrication processes is based on the lost wax molding technique (LIGA) (lithography, electroforming, molding). As shown in Fig. 2.73, LIGA uses highly collimated X-rays projected through a special X-ray mask to provide near diffraction-free exposure of a thick photoresist. The technique can create structures with aspect ratios in excess of 100:1 and can hold submicron tolerances over many hundreds of microns of vertical height (Mohr et al. 1988).

Fabrication of micro-channels in dielectrics, using femtosecond lasers, has also been used (Hwang et al. 2004). In these applications amplified pulsed lasers produc-

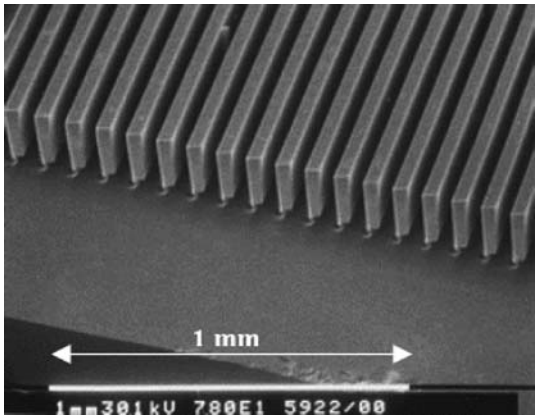

Fig. 2.70 Micro-channel array formed by silicon DRIE. Reprinted from Kandlikar and Grande (2002) with permission

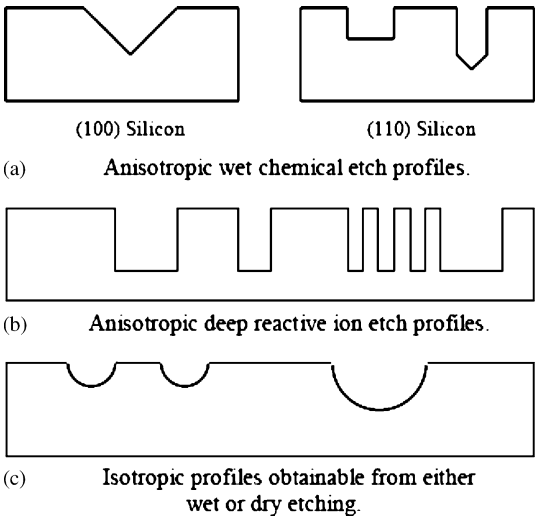

Fig. 2.71a–c Bulk micro-machining etch profiles. Reprinted from Kandlikar and Grande (2002) with permission

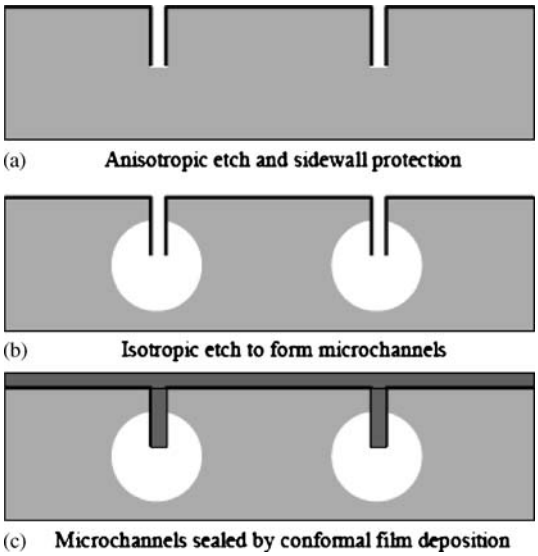

Fig. 2.72a–c Construction of buried micro-channels by combined anisotropic and isotropic etching. Reprinted from Kandlikar and Grande (2002) with permission

ing micro-joules per pulse were used to overcome the optical breakdown threshold of the substrate, typically glass or fused silica. Based on this method, cylindrical micro-channels with diameters ranging from 8 to 20 μm can be fabricated in a water-immersed polymethyl methacrylate (PMMA) substrate (Fig. 2.74). The laser beam is focused onto the sample by a long working distance objective. Water immersion is used to reduce aberrations and improve the performance and consistency of the fabrication method.

None of the technologies described above can individually produce a complete micro-system. Hybridization is the means of combining all the necessary disparate

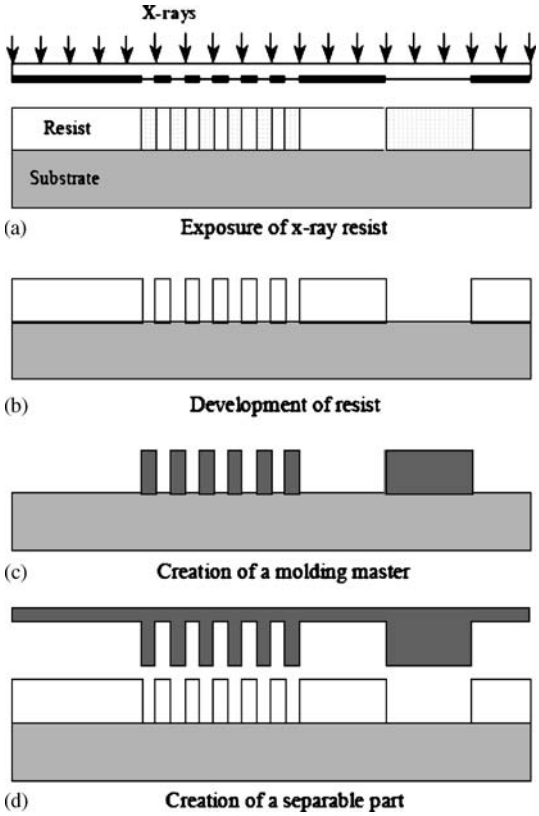

Fig. 2.73a–d The LIGA process. Reprinted from Kandlikar and Grande (2002) with permission

components. Direct wafer bonding can generally be used to obtain a wide range of adhesive bond strengths (Plosl and Krauter 1999). Three bonding techniques of particular interest are fusion bonding, anodic bonding, and adhesive bonding. In fusion bonding two wafers whose surfaces are silicon or silicon compounds can be bonded through a combination of chemical surface treatments, pressure, and annealing at elevated temperature. In anodic bonding silicon and ionic glass surfaces are jointed through a combination of pressure, temperature, and electric field. While both fusion and anodic bonding can produce interfaces of high strength, they are quite material-specific. For generic hetero-bonding, adhesive techniques are the solution. Figure 2.75 shows how micro-channel devices can be formed by wafer bonding.

A method that creates patterned micro-structures distributed on the bottom wall of the micro-channel was proposed by Yang et al. (2006). A roughened bottom wall was created using the crystal orientation characteristics of the wafers.

Wet etching procedures were used in fabrication of the micro-channel heat sink. The substrates were covered with thermally grown silicon dioxide and patterned in a photolithography process. Hexagonal cavities distributed over the channel bottom wall were created using a mask containing parallelograms in the micro-channel. Figure 2.76 shows a typical example of created micro-structures distributed along

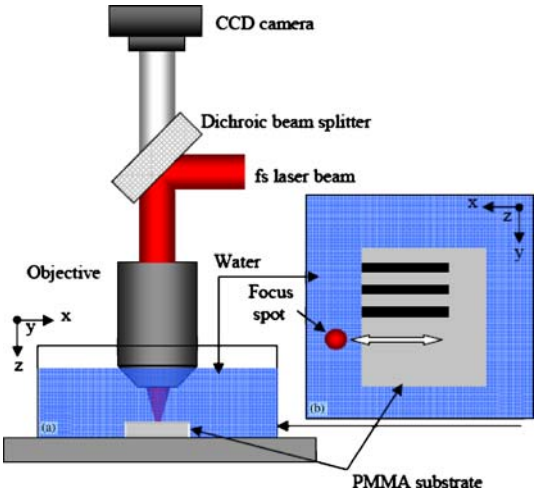

Fig. 2.74a,b Schematic diagram of (**a**) the experimental set-up for fabrication of micro-channels and (**b**) the fabrication geometry in the sample. Reprinted from Hwang et al. (2004) with permission

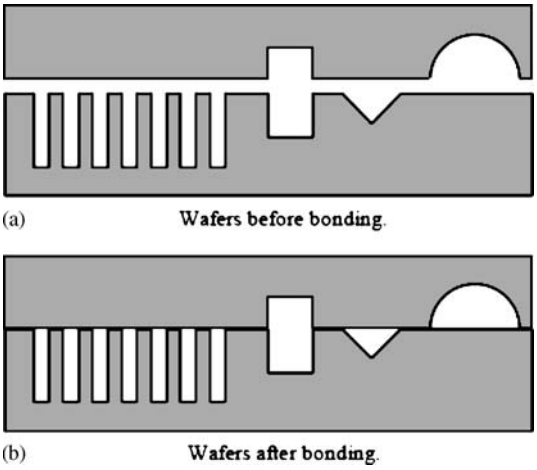

Fig. 2.75 The wafer bonding process. Reprinted from Kandlikar and Grande (2002) with permission

the bottom walls. The channel width is 500 μm and the cavity size is $200 \times 200 \times 55$ μm. The microstructures are expected to induce fluid flow and thermal boundary layer disturbances, leading to an enhanced heat transfer coefficient.

A completely different way involves use of metal foams, or metal made porous otherwise (North and Cho 2003; Hetsroni et al. 2006a).

Aluminum foam can be used as a porous medium in the model of a heat sink with inner heat generation (Hetsroni et al. 2006a). Open-cell metal foam has a good effective thermal conductivity and a high specific solid–fluid interfacial surface area.

Depending on the metal foam configuration, its specific surface area varies from 500 for original foam to $10{,}000\,\mathrm{m}^2/\mathrm{m}^3$ for compressed foam. Aluminum foam of 40 pores per inch (ppi) was studied. The structure of the porous material is presented in Fig. 2.77.

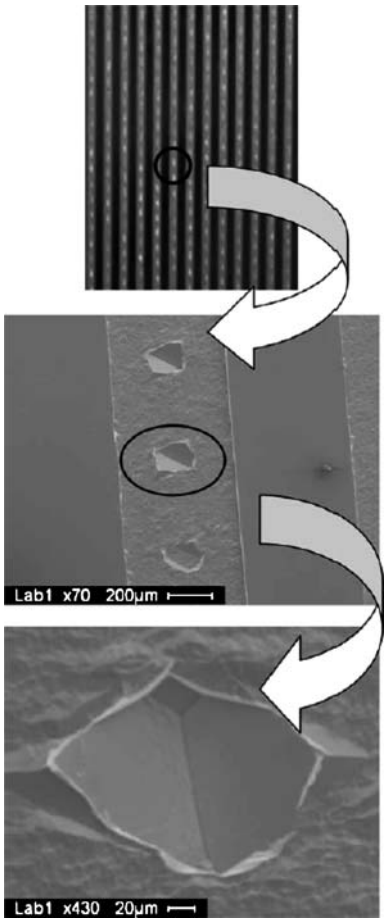

Fig. 2.76 SEM micrograph of roughened micro-channel bottom wall with distributed hexagonal micro-structures. Reprinted from Yang et al. (2006) with permission

Summary

1. The increased power density in electronic and other devices leads to higher operational temperature, which limits the device performance. Cooling problems are becoming acute for such devices, and an efficient cooling system is required to maintain an isothermal temperature of the device. Direct liquid cooling has emerged as one of the most promising thermal management techniques for micro-systems where the control of both the operating temperature and the temperature cycling is still a challenging task.

The active micro-channel cooling contains a cooling system centered on a micro-heat collector that is fabricated much in the same way as the chip. Heat collector usually has a dense amount of micro-channels etched into the surface that works to transfer heat to a fluid, which is circulated through the entire package.

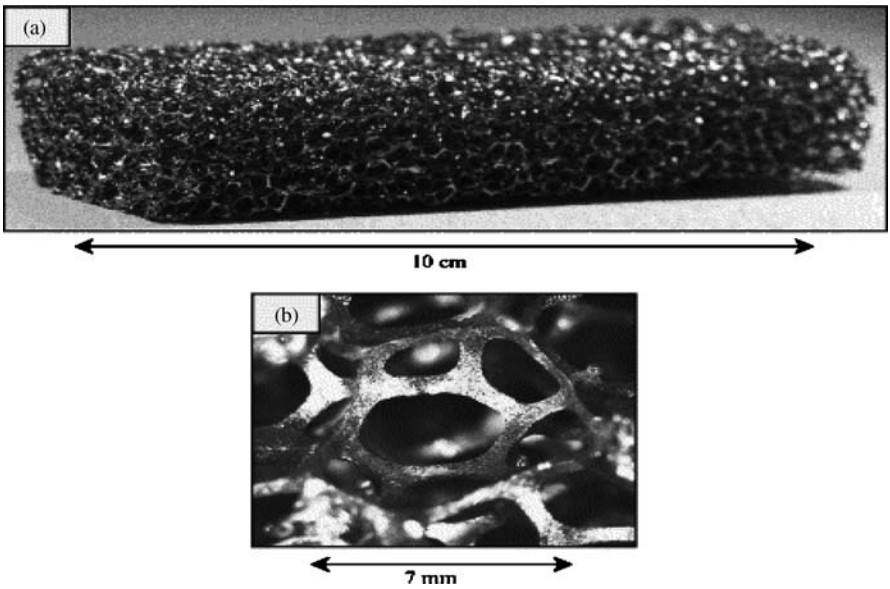

Fig. 2.77a,b Sample of aluminum foam. Reprinted from Hetsroni et al. (2006a) with permission

There are now companies engaged in the development and commercialization not only of micro-channels, but also spray cooling, synthetic jets, liquid metal cooling, and sintered porous inserts. For heat flux densities up to 10–50 W/cm^2 air cooling may remain the cooling option of choice. For heat fluxes over 100–500 W/cm^2 some form of liquid cooling appears to be the most viable option. Several investigations demonstrated that using water as cooling fluid has the potential for industrial application in the range between 500 and 1,000 W/cm^2. There are also devices with cooling heat flux requirements on the order of 10^3–10^4 W/cm^2. Fusion reactors, for example, contain components that require continuous cooling on the order of 10^4 W/cm^2. Other examples are directed energy devices such as high efficiency, multi-megawatt continuous-wave magnetrons used for short-pulse lasers and radars, optical devices that deliver high brilliance beams. The enormous cooling requirements of these high-energy devices preclude the use of refrigerants. For these applications, water and liquid metals remain the coolants of choice. The high cost of the systems, the stringent material and compatibility requirements constrain the application of liquid metals to cooling. Water may be chosen as a cooling fluid because of its outstanding thermophysical properties: very high specific heat and latent heat of vaporization.

The high-performance supercomputers, certain power devices, electric vehicles, and advanced avionics need to maintain their temperature in the range of 30–60 °C at the high-flux range. However, because of its very low vapor pressure at the expected design saturation temperatures of 40–65 °C, water is not a candidate fluid for the flow boiling coolant. The most promising are liquid refrigerants, which at atmospheric pressure have saturation temperatures in the range of 30–60 °C. For

example, FC-72 may be taken as a possible candidate of various dielectric fluids. It has at atmospheric pressure the saturation temperature of 56.6 °C, and the latent heat 94.8 kJ/kg. It should be taken into account that there is some concern over the global warming potential of all refrigerants, as well as the danger of chemical breakdown and production of harmful substances upon exposure to high temperatures.

2. In this book we will consider the channels with hydraulic diameters ranging roughly from 5 to 500 μm as micro-channels and the channels with hydraulic diameters $d_h > 500$ μm as conventional size channels. Heat transfer in micro-channels has been studied in a number of investigations, and has been compared with the behavior of conventional (i.e., large-sized) length scales. However, there have been wide discrepancies between different sets of published results. Measured heat transfer coefficients in single-phase and two-phase micro-channel flows have either well exceeded, or fallen far below, those predicted for conventional channels. The Reynolds number at which the flow behavior indicates a transition from laminar to turbulent flow has also differed widely in these studies We considered these problems with regard to micro-channels to gain a better understanding of the distinctive properties of the measurement techniques and uncertainties, the conditions, under which the experimental results should be compared to analytical or numerical predictions, boiling phenomenon, as well as different types of micro-channel heat sinks.

3. Pressure drop measurements. For the majority of experiments the instrumentation was relatively similar. Due to limitations associated with the small size of the channels, pressures were not measured directly inside the micro-channels. To obtain the channel entrance and exit pressures, measurements were taken in a plenum or supply line prior to entering the channel. It is insufficient to assume that the friction factor for laminar compressible flow can be determined by means of analytical predictions for incompressible flow.

The method of the measurement pressure drop inside the channel itself should be used to check the overall agreement between experimental and predicted results. The internal pressure measurements should be used also to validate the entrance and exit losses.

4. Temperature measurements. Reliable measurement and control of temperature in the micro-scale are highly required to develop various micro-devices. Many temperature measurement methods traditionally applied to macro-devices are evolving into more advanced techniques applicable to micro-devices taking into consideration enhanced spatial, temporal, and temperature resolution. The thermochromic liquid crystal may be employed for full-field mapping of temperature fields. The good results obtained by the widespread use of infrared thermography (IR) in experimental studies of convective heat transfer and boiling in micro-channels have proved this method to be an effective tool in overcoming several limitations of the standard sensors originating both from the measurement and the visualization techniques. Recently IR has been developed to measure the temperature of the fluid and wall in a micro-channel, using a transparent cover. Measurement of the temperature field of a micro-object by an infrared camera has a number of problems. The small size of the object causes a substantial amount of infrared radiation from the

background. The problem of background influence on the object temperature measurement should be taken into account.

5. In general, the result of measurement is only an approximation or estimate of the value of the specific quantity subject to measurement, and thus the result is complete only when accompanied by a quantitative statement of its uncertainty. Because the reliability of evaluations of components of uncertainty depends on the quality of the information available, it is recommended that all parameters upon which the measurand depends be varied to the fullest extent practicable so that the evaluations are based as much as possible on observed data.

6. Pressure drop and heat transfer in a single-phase incompressible flow. According to conventional theory, continuum-based models for channels should apply as long as the Knudsen number is lower than 0.01. For air at atmospheric pressure, Kn is typically lower than 0.01 for channels with hydraulic diameters greater than 7 μm. From descriptions of much research, it is clear that there is a great amount of variation in the results that have been obtained. It was not clear whether the differences between measured and predicted values were due to determined phenomenon or due to errors and uncertainties in the reported data. The reasons why some experimental investigations of micro-channel flow and heat transfer have discrepancies between standard models and measurements will be discussed in the next chapters.

7. Steam–liquid flow. Two-phase flow maps and heat transfer prediction methods which exist for vaporization in macro-channels and are inapplicable in micro-channels. Due to the predominance of surface tension over the gravity forces, the orientation of micro-channel has a negligible influence on the flow pattern. The models of convection boiling should correlate the frequencies, length and velocities of the bubbles and the coalescence processes, which control the flow pattern transitions, with the heat flux and the mass flux. The vapor bubble size distribution must be taken into account.

The flow pattern in parallel micro-channels is quite different from that found in a single micro-channel. At the same values of heat and mass flux, different flow regimes exist in a given micro-channel depending on the time. Moreover, at the same time, different flow regimes may exist in various parallel micro-channels. At low vapor quality heat flux causes a sudden release of energy into the vapor bubble, which grows rapidly and occupies the entire channel. The rapid bubble growth pushes the liquid–vapor interface on both caps of the vapor bubble, at the upstream and the downstream ends, and leads to a reverse flow. This phenomenon may be regarded as explosive boiling. The CHF phenomenon is different from that observed in annular flow. A key difference is the amplification of flow and wall temperature instabilities prior to CHF.

Confined boiling of water and surfactant solutions under condition of natural convection causes a heat transfer enhancement. Additive of surfactant leads to enhancement of heat transfer compared to water boiling in the same gap size; however, this effect decreased with decreasing gap size. For the same gap size, CHF decreases with an increase in the channel length. CHF in surfactant solutions is significantly lower than in water.

It is noteworthy that several studies presented very different results for both the heat transfer at flow boiling and CHF in micro-channels. This is generally due to differences in many parameters that characterize these studies such as the geometry, the hydraulic diameter, the shape and surface roughness of the channels, the fluid nature, the boundary conditions, the flow regimes and the measuring technique. Such a large variety of experimental conditions often makes it difficult to apply the results of a given study to other investigations. The present chapter gives only a general insight on the problem. In the next chapters the main categories of effects will be discussed to study the boiling in micro-channels.

8. For micro-channel heat sink there is an optimum channel dimension. If the pumping power is not limited, there is no optimum aspect ratio since the larger the aspect ratio, the better the heat transfer. With the constraint on pumping power, however, the aspect ratio cannot be indefinitely increased because the fluid flowing near the fin does not remove any heat at very high aspect ratios. For an actual micro-channel cooling element, the micro-channels often have a rectangular shape in its cross-section, with aspect ratio in the range of 5–10 (with the short side at the base of the cooling element and the long sides forming fins between channels).

9. Fabrication technique. The micro-channels on the order of 25 μm width with accuracy of 4 μm can be manufactured with commercially available equipment. The micro-channels with diameters ranging from 8 to 20 μm can be fabricated using femtosecond lasers. In some experiments on the effect of rarefaction on the friction factor the channels of $d_h = 4.688\,\mu m$ with surface roughness ranging from 0.002 to 0.06 μm were used. Using photolithography and wet etching technique it was possible to fabricate micro-channels with hydraulic diameters from 1.01 to 35.91 μm and lengths from 10 to 11 cm.

References

Acikalin T, Wait S, Garimella S, Raman A (2004) Experimental investigation of the thermal performance of piezoelectric fans. Heat Transfer Eng 25:4–14

Adams TM, Abdel-Khalik SI, Jeter SM, Qureshi ZH (1998) An experimental investigation of single-phase forced convection in micro-channels. Int J Heat Mass Transfer 41:851–857

Adams TM, Dowling MF, Abdel-Khalik SI, Jeter SM (1999) Applicability of traditional turbulent single phase forced convection correlations to non-circular micro-channels. Int J Heat Mass Transfer 42:4411–4415

American Society Of Mechanical Engineers (ASME) (2000) Policy on reporting uncertainties in experimental measurements and results. J Heat Transfer 122:411–413

Azar K, Benson JR, Manno VP (1991) Liquid crystal imaging for temperature measurement of electronic devices. In: Proceedings of 7th Annual IEEE Semiconductor Thermal Measurement and Management Symposium, Phoenix, 12–14 February 1991, pp 23–33

Bahadur R, Bar-Cohen A (2005) Thermal design and optimization of polymer-based pin fin natural convection heat sinks. IEEE Trans Comp Packag Technol 28(2):238–246

Bar-Cohen A, Bahadur R, Iyengar M (2006) Least-energy optimization of air-cooled heat sinks for sustainability-theory, geometry and material selection. Energy 31:579–619

Bau HH (1998) Optimization of conduits' shape in micro heat exchangers. Int J Heat Mass Transfer 41:2717–2723

Bean KE (1978) Anisotropic etching of silicon. IEEE Trans Electron Dev 25(10):1185–1193
Beratlis N, Smith M (2003) Optimization of synthetic jet cooling for micro-electronics applications. In: Proceedings of 19th SemiTherm Symposium, San Jose, 11–13 March 2003, pp 66–73
Bergles AE, Lienhard JH, Gall V, Kendall GE, Griffith P (2003) Boiling and evaporation in small diameter channels. Heat Transfer Eng 24:18–40
Bhardwaj J, Ashraf H, McGuarrie A (1997) Dry silicon etching for MEMS. In: Proceedings of the 191st Meeting of the Electrochemical Society, Microstructures and Microfabricated Systems, III Symposium, Montreal, 4–9 May 1997, vol 97-5, pp 118–130
Bonjour J, Lallemand M (1998) Flow patterns during boiling in a narrow space between two vertical surfaces. Int J Multiphase Flow 24:947–960
Bowers MB, Mudawar I (1994) High flux boiling in low flow rate, low pressure drop mini-channel and micro-channel heat sinks. Int J Heat Mass Transfer 37:321–332
Boyd RD (1985) Subcooled flow boiling critical heat flux and its application to fusion energy components. Part 1. A review of fundamentals of CHF and related data base. Fusion Tech 7:7–31
Calame JP, Myers RE, Binari SC, Wood FN, Garven M (2007) Experimental investigation of micro-channel coolers for the high heat flux thermal management of GaN-on-SiC semiconductor devices. Int J Heat Mass Transfer 50: 4767-4779
Celata GP, Cumo M, Zummo G (2004) Thermal-hydraulic characteristics of single- phase flow in capillary pipes. Exp Thermal Fluid Sci 28:87–95
Celata GP (2004). Heat transfer and fluid flow in micro-channels. Begell House, N.Y.
Celata GP, Cumo M, McPhail SJ, Tesfagabir L, Zummo G (2005) Experimental study on compressibility effects in micro-tubes, in Proceedings of the XXIII UIT Italian National Coference, 2005:53-60
Chaudhari AM, Woudenberg TM, Albin M, Goodson KE (1998) Transient liquid crystal thermometry of microfabricated PCR vessel arrays. J Microelectromech Sys 7:345–355
Cheng P, Wu WY (2006) Mesoscale and microscale phase heat transfer. In: Greene G, Cho Y, Hartnett J, Bar-Cohen A (eds) Advances in heat transfer, vol 39. Elsevier, Amsterdam
Choi SB, Barron RF, Warrington RQ (1991) Fluid flow and heat transfer in micro- tubes. ASME DSC 40:89–93
Chung PM-Y, Kawaji M (2004) The effect of channel diameter on adiabatic two-phase flow characteristics in micro-channels. Int J Multiphase Flow 30:735–761
Colgan E (2005) A practical implementation of silicon microchannel coolers for high power chips. In: Proceedings of 21st SemiTherm Symposium, San Jose, 15–17 March 2005, pp 1–7
Copeland D, Behnia M, Nakayama W (1997) Manifold micro-channel heat sinks: isothermal analysis. IEEE Trans Comp Packag Manuf Technol A 20:96–102
Dupont V, Thome JR, Jacobi AM (2004) Heat transfer model for evaporation in microchannels. Part II. Comparison with the database. Int J Heat Mass Transfer 47:3387–3401
Evans FE, Wennerstrom H (1999) The colloidal domain, 2nd edn. VCH, New York
Fabbri M, Jiang S, Dhir VK (2005) A comparative study of cooling of high power density electronics using sprays and microjets. J Heat Transfer 127:38–48
Fujita Y, Ohta H, Uchida S, Nishikawa K (1988) Nucleate boiling heat transfer and critical heat flux in narrow space between rectangular surface. Int J Heat Mass Transfer 31:229–239
Furjes P, Vízvary Zs, Adam M, Barsony I, Morrissey A, Ducso Cs (2002) Materials and processing for realization of micro-hotplates operated at elevated temperature. J Micromech Microeng 12:425–429
Gad-el-Hak M (1999) The fluid mechanics of micro-devices. The Freemen Scholar Lecture. J Fluid Eng 121:5–33
Garimella S, Sobhan C (2003) Transport in microchannels: a critical review. Ann Rev Heat Transfer 13:1–50
Gillot C, Schaeffer C, Bricard A (1998) Integrated micro heat sink for power multichip module. IEEE Trans Ind Appl 36(1):217–221
Guo ZY, Li ZX (2003) Size effect on single-phase channel flow and heat transfer at microscale. Int J Heat Mass Transfer 24:284–298

Harley JC, Huang Y, Bau H, Zemel JN (1995) Gas flow in micro-channels. J Fluid Mech 284:257–274

Harpole GM, Eninger JE (1991) Micro-channel heat exchanger optimization. In: Proceedings of 7th IEEE SemiTherm Symposium, Scottsdale, 12–14 February 1991, pp 59–63

Hetsroni G, Gurevich M, Mosyak A, Pogrebnyak E, Rozenblit R, Yarin LP (2003a) Boiling in capillary tubes. Int J Multiphase Flow 29:1551–1563

Hetsroni G, Gurevich M, Mosyak A, Rozenblit R (2004a) Drag reduction and heat transfer of surfactants flowing in a capillary tube. Int J Heat Mass Transfer 47:3797–3809

Hetsroni G, Gurevich M, Mosyak A, Rozenblit R, Yarin LP (2002c) Subcooled boiling of surfactant solutions. Int J Multiphase Flow 28:347–361

Hetsroni G, Gurevich M, Rozenblit R (2006a) Sintered porous medium heat sink for cooling of high-power mini-devices. Int J Heat Fluid Flow 27:259–262

Hetsroni G, Mosyak A, Segal Z (2001a) Nonuniform temperature distribution in electronic devices cooled by flow in parallel micro-channels. IEEE Trans Comp Packag Technol 24:16–23

Hetsroni G, Zakin JL, Lin Z, Mosyak A, Pancallo EA, Rozenblit R (2001b) The effect of surfactants on bubble growth, wall thermal patterns and heat transfer in pool boiling. Int J Heat Mass Transfer 44:485–497

Hetsroni G, Mosyak A, Pogrebnyak E, Segal Z (2005b) Explosive boiling of water in parallel micro-channels. Int J Multiphase Flow 31:371–392

Hetsroni G, Mosyak A, Pogrebnyak E, Segal Z (2006b) Periodic boiling in parallel micro-channels at low vapor quality. Int J Multiphase Flow 32:1141–1159

Hetsroni G, Mosyak A, Pogrebnyak E, Sher I, Segal Z (2006c) Bubble growth in saturated pool boiling in water and surfactant solution. Int J Multiphase Flow 32:159–182

Hetsroni G, Mosyak A, Pogrebnyak E, Segal Z (2007) Natural convection boiling of water and surfactants in narrow horizontal annular channels. Int J Multiphase Flow 33:469–483

Hetsroni G, Mosyak A, Pogrebnyak E, Yarin L (2005a) Fluid flow in micro-channels. Int J Heat Mass Transfer 48:1982–1998

Hetsroni G, Mosyak A, Pogrebnyak E, Yarin LP (2005c) Heat transfer in micro-channels: comparison of experiments with theory and numerical results. Int J Heat Mass Transfer 48:5580–5601

Hetsroni G, Mosyak A, Segal Z, Pogrebnyak E (2003b) Two-phase flow patterns in parallel micro-channels. Int J Multiphase Flow 29:341–360

Hetsroni G, Mosyak A, Bernheim-Groswasser A, Talmon Y, Zakin JL (2003c) The effect of cationic surfactant on turbulent flow patterns. J Heat Transfer ASME 125:947–950

Hetsroni G, Mosyak A, Segal Z, Pogrebnyak E (2002a) Two-phase flow patterns in parallel micro-channels. Int J Multiphase Flow 9:341–260

Hetsroni G, Mosyak A, Segal Z, Ziskind G (2002b) A uniform temperature heat sink for cooling of electronic devices. Int J Heat Mass Transfer 45:3275–3286

Hetsroni G, Zakin JL, Gurevich M, Mosyak A, Pogrebnyak E, Rozenblit R (2004b) Saturated flow boiling heat transfer of environmentally acceptable surfactants. Int J Multiphase Flow 30:717–734

Hwang DJ, Choi TY, Grigoropoulos CP (2004) Liquid assisted femtosecond laser drilling of straight and three-dimensional micro-channels in glass. Appl Phys A 79:605–612

Jiang L, Wang Y, Wong M, Zohar Y (1999a) Fabrication and characterization of a microsystem for a micro-scale heat transfer study. J Micromech Microeng 9:422–428

Jiang L, Wong M, Zohar Y (1999b) Phase change in microchannel heat sinks with integrated temperature sensors. J Microelectromech Syst 8:358–365

Jiang L, Wong M, Zohar Y (2000) Unsteady characteristics of a thermal microsystem. Sens Actuators A 82:108–113

Kakac S, Vasiliev LL, Bayazitoglu Y, Yener Y (2005). Micro-scale heat transfer. Springer, Berlin Heidelberg.

Kandlikar SG, Grande W (2002) Evolution of micro-channel flow passages – thermo-hydraulic performance and fabrication technology. In: Proceedings of IMECE ASME International Mechanical Engineering Congress and Exposition, New Orleans, 17–22 November 2002, IMECE 2002-32043, pp 1–13

Kandilikar SG, Upadhye H (2005) Extending the heat flux limit with enhanced microchannels in direct single-phase cooling of computer chips. In: Proceedings of 21st SemiTherm Symposium, San Jose, 15–17 March 2005, pp 8–15

Kandlikar SG, Garimella S, Li D, Colin S, King MR (2005) Heat Transfer And Fluid Flow In Minichannels And Microchannels. Elsevier Science & Technology (Netherlands)

Karniadakis GE, Beskon A (2002) Fundamentals and simulation. Springer, Berlin Heidelberg New York

Katto Y, Ohno H (1984) An improved version of the generalized correlation of critical heat flux for the forced convective boiling in uniformly heated vertical tubes. Int J Heat Mass Transfer 27(9):1641–1648

Katto Y, Yokoya S, Teraoka K (1966) Experimental study of nucleate boiling in case of making interference-plate approach to the heating surface. In: Proceedings of 3rd International Heat Transfer Conference, 1966, vol 3, pp 219–227

Kim SJ (2004) Methods for thermal optimization of microchannel heat sinks. Heat Transfer Eng 25(1):37–49

Kim HJ, Kihm KD (2001) Application of a two-color laser induced fluorescence (LIF) technique for temperature mapping. In: Proceedings of ASME International Mechanical Engineering Congress and Exposition, IMECE2001/HTD-24411, New York, 11–16 November 2001

Kim J, Golliher E (2002) Steady state model of a micro loop heat pipe. Proceedings of 18th SemiTherm Symposium, San Jose, 15–17 March 2005, pp 137–144

Klein D, Hetsroni G, Mosyak A (2005) Heat transfer characteristics of water and APG surfactant solution in a micro-channel heat sink. Int J Multiphase Flow 31:393–415

Kline SJ, McClintock FA (1953) Describing uncertainties in single-sample experiments. Mech Eng 75(Jan):3–8

Knight RW, Hall DJ, Goodling JS, Jaeger RC (1992) Heat sink optimization with application to micro-channels. IEEE Trans Comp Hybrids Manuf Technol 15:832–842

Kohl MJ, Abdel-Khalik SI, Jeter SM, Sadowski DL (2005) An experimental investigation of microchannel flow with internal pressure measurements. Int J Heat Mass Transfer 48:1518–1533

Lasance CJM, Simons RE (2005) Advances in high performance cooling for electronics. http://electronics-cooling.com/html/2005nov.article2.html. Accessed 2007

Le Berre M, Pandraud G, Morfouli P, Lallemand M (2006) The performance of micro heat pipes measured by integrated sensors. J Micromech Microeng 16:1047–1050

Lee DY, Vafai K (1999) Comparative analysis of jet impingement and microchannel cooling for high heat flux applications. Int J Heat Mass Transfer 42:1555–1568

Lee PC, Tseng FG, Pan C (2004) Bubble dynamics in micro-channels. Part 1. Single microchannel. Int J Heat Mass Transfer 47:5575–5589

Li X, Lee WY, Wong M, Zohar Y (2000) Gas flow in constriction microdevices. Sens Actuators A 83:277–283

Lin Q, Jiang F, Wang X-Q, Han Z, Tai Y-C, Lew J, Ho C-M (2000) MEMS Thermal Shear-Stress Sensors: Experiments, Theory and Modeling, Technical Digest, Solid State Sensors and Actuators Workshop, Hilton Head, SC, 4–8 June 2000, pp 304–307

Lin TY, Yang CY (2007) An experimental investigation of forced convection heat transfer performance in micro-tubes by the method of liquid crystal thermography. Int. J. Heat Mass Transfer 50: 4736-4742

Liu J, Enzelberger M, Quake S (2002) A nanoliter rotary device for polymerase chain reaction. Electrophoresis 23:1531–1536

Lu B, Zheng Y, Scriven LE, Davis HT, Talmon Y, Zakin JL (1998) Effect of variation counterion-to-surfactant ratio on rheology and micro-structures of drag reducing cationic surfactant systems. Rheol Acta 37:528–548

Luo K, Shi Z, Varesi J, Majumdar A (1997) Sensor nanofabrication, performance, and conduction mechanisms in scanning thermal microscopy. J Vac Sci Technol B 15:349–360

Majumdar A (1999) Scanning thermal microscopy. Annu Rev Mater Sci 29:505–585

Manglik RM, Wasekar VM, Zhang J (2001) Dynamic and equilibrium surface tension of aqueous surfactant and polymeric solutions. Exp Thermal Fluid Sci 25:55–64

Maynes D, Webb AR (2002) Velocity profile characterization in sub-millimeter diameter tubes using molecular tagging velocimetry. Exp Fluids 32:3–15

Mehendale SS, Jacobi AM, Shah RK (1999) Heat exchangers at micro- and meso-scales. In: Proceedings of International Conference on Compact Heat Exchangers and Enhance Technology for the Process Industries, Banff, 18–23 July 1999, pp 55–74

Miner A, Ghoshal U (2004) Cooling of high-power density microdevices using liquid metal coolants. Appl Phys Lett 85:506–508

Mishan Y, Mosyak A, Pogrebnyak E, Hetsroni G (2007) Effect of developing flow and thermal regime on momentum and heat transfer in micro-scale heat sink. Int J Heat Mass Transfer 50:3100–3114

Mohapatra S, Loikitis D (2005) Advances in liquid coolant technologies for electronics cooling. In: Proceedings of 21st SemiTherm Symposium, San Jose, 15–17 March 2005, pp 354–360

Mohr J, Ehrfeld W, Munchmeyer D (1988) Requirements on resist layers in deep-etch synchrotron radiation lithography. J Vac Sci Technol B6:2264–2267

Morini GL (2004) Single phase convective heat transfer in micro-channels: overview of experimental results. Int J Thermal Sci 43:631–651

Morini Gl, Lorenzini M, Salvigini S (2006) Friction characteristics of compressible gas flows in micro-tubes. Exp. Thermal and Fluid Science 30:733-744

Mudawar I (2001) Assessment of high-heat-flux thermal management schemes. IEEE CPT Trans 24:122–141

Ng EYK, Poh ST (1999) Investigative study of manifold microchannel heat sinks for electronic cooling design. J Electron Manuf 9(2):155–166

North M, Cho W (2003) High heat flux liquid-cooled porous metal heat sink. In: Proceedings of IPAK 2003, Maui, 6–11 July 2003, Paper 35320

Palm R (2001) Heat transfer in micro-channels. Micro-scale Thermophys Eng 5:155–175

Peng XF, Peterson GP (1995) The effect of thermo-fluid and geometric parameters on convection of liquid through rectangular micro-channels. Int J Heat Mass Transfer 38:755–758

Peng XF, Peterson GP (1996) Convective heat transfer and flow friction for water flow in microchannel structures. Int J Heat Mass Transfer 39:2599–2608

Peng XF, Peterson GP, Wang BX (1994a) Frictional flow characteristics of water flowing through micro-channels. Exp Heat Transfer 7:249–264

Peng XF, Peterson GP, Wang BX (1994b) Heat transfer characteristics of water flowing through microchannels. Exp Heat Transfer 7:265–283

Peng XF, Wang BX (1998) Forced convection and boiling characteristics in micro-channels. In: Proceedings of 11 IHTC, 1, Kyonji, Korea, 23–28 August 1998, pp 371–390

Peterson M, Fisher T, Garimella S, Schlitz D (2003) Experimental characterization of low voltage field emission from carbon-based cathodes in atmospheric air. In: Proceedings of IMECE'03, Washington DC, 15–23 November 2003, Paper 41775

Pfund D, Rector D, Shekarriz A, Popescu A, Welty J (2000) Pressure drop measurements in a microchannel. AIChE J 46:1496–1507

Phillips RJ (1990) Micro-channel heat sinks. In: Bar-Cohen A, Kraus AD (eds) Advances in thermal modeling of electronic components and systems, vol 2, pp 109–184

Plosl A, Krauter G (1999) Wafer direct bonding: tailoring adhesion between brittle materials. Mater Sci Eng R25:92–98

Prasher RS, Chang JY, Sauciuc I, Narasimhan S, Chau D, Chrysler G, Myers A, Prstic S, Hu C (2005) Nano and micro technology-based next-generation package-level cooling solutions. Intel Technol J 4(4):285–296

Qu W, Mudawar I (2002a) Experimental and numerical study of pressure drop and heat transfer in a single-phase micro-channel heat sink. Int J Heat Mass Transfer 45:2549–2565

Qu W, Mudawar I (2004) Measurement and correlation of critical heat flux in two-phase microchannel heat sinks. Int J Heat Mass Transfer 47:2045–2059

Qu W, Mudawar I (2002b) Prediction and measurement of incipient boiling heat flux in microchannel heat sinks. Int J Heat Mass Transfer 45:3933–3945

Revellin R, Dupont V, Ursenbacher T, Thome JR, Zun I (2006) Characterization of diabatic two-phase flows in microchannels: flow parameter results for R-134a in a 0.5 mm channel. Int J Multiphase Flow 32:755–774

Ross D, Gaitan M, Locascio LE (2001) Temperature measurement in microfluidic systems using a temperature-dependent fluorescent dye. Anal Chem 73:4117–4123

Sammarco TS, Burns MA (1999) Thermocapillary pumping of discrete drops in microfabricated analysis devices. AIChE J 45:350–366

Schlicting H, Gersten K (2000) Boundary layer theory, 8th rev and England edn. Springer, Berlin Heidelberg New York

Serizawa A, Feng Z, Kawara Z (2002) Two-phase flow in microchannels. Exp Thermal Fluid Sci 26:703–714

Shah RK, London AL (1978) Laminar flow forced convection in ducts. Academic, New York

Sher I, Hetsroni G (2002) An analytical model for nucleate pool boiling with surfactant additives. Int J Multiphase Flow 28:699–706

Shih JC, Ho C-M, Liu J, Tai Y-C (1996) Monatomic and polyatomic gas flow through uniform microchannels. Microelectromech Syst (MEMS) DSC 59:197–203

Simons RE (1996) Direct liquid immersion cooling for high power density microelectronics. Electron Cooling 2(2):7–12

Sobhan CB, Garimella SV (2001) A comparative analysis of studies on heat transfer and fluid flow in micro-channels. Microscale Thermophys Eng 5:293–311

Steinke M, Kandlikar SG (2003) Flow boiling and pressure drop in parallel flow micro-channels. In: Kandlikar SG (ed) Proceedings of 1st International Conference on Micro-channels and Mini-channels, Rochester, 24–25 April 2003, pp 567–579

Thome JR (2006) State-of-the-art overview of boiling and two-phase flows in microchannels. Heat Transfer Eng 27(9):4–19

Thome JR, Dupont V, Jacobi AM (2004) Heat transfer model for evaporation in microchannels. Part I. Presentation of the model. Int J Heat Mass Transfer 47:3375–3385

Tiselj I, Hetsroni G, Mavko B, Mosyak A, Pogrebnyak E, Segal Z (2004) Effect of axial conduction on the heat transfer in micro-channels Int J Heat Mass Transfer 47:2551–2565

Triplett KA, Ghiaasiaan SM, Abdel-Khalik SI, Sadowski DL (1999) Gas–liquid two-phase flow in microchannels. Part I. Two-phase flow patterns. Int J Multiphase Flow 25:377–394

Tsai J-H, Lin L (2002) Transient thermal bubble formation on polysilicon micro-resisters. J Heat Transfer 124:375–382

Tuckerman D, Pease RFW (1981) High performance heat sinking for VLSI. IEEE Electron Device Lett 2:126–129

Turner SE, Lam LC, Faghri M, Gregory OJ (2004) Experimental investigation of gas flow in microchannels. J Heat Transfer 126:753–763

Turner SE, Sun H, Faghri M, Gregory OJ (2002) Gas flow through smooth and rough microchannels. In: Proceedings of the 12th International Heat Transfer Conference, Grenoble, 18–23 August 2002

Tzanand YL, Yang YM (1990) Experimental study of surfactant effects on pool boiling heat transfer J Heat Transfer 112:207–212

Varesi J, Majumdar A (1998) Scanning joule expansion microscopy at nanometer scales. Appl Phys Lett 72:37–39

Wang BX, Peng XF (1994) Experimental investigation of liquid forced-convection heat transfer through micro-channels. Int J Heat Mass Transfer 37:73–82

Wasekar VM, Manglik RM (2002) The influence of additive molecular weight and ionic nature on the pool boiling performance of aqueous surfactant solutions. Int J Heat Mass Transfer 45:483–493

Webb RL, Zhang M (1998) Heat transfer and friction in small diameter channels. Microscale Thermophys Eng 2:189–202

Wei XJ, Joshi Y (2002) Optimization study of stacked micro-channel heat sinks for microelectronic cooling. IEEE Trans Comp Packag Technol 26(1):55–61

Weisberg A, Bau HH, Zemel JN (1992) Analysis of micro-channels for integrated cooling. Int J Heat Mass Transfer 35(10):2465–2474
Wojtan L, Revellin R, Thome JR (2006) Investigation of saturated critical heat flux in a single, uniformly heated microchannel. Exp Thermal Fluid Sci 30:765–774
Wu PY, Little WA (1984) Measurement of the heat transfer characteristics of gas flow in fine channel heat exchangers used for micro-miniature refrigerators. Cryogenics 23:415–420
Wu WT, Yang YM (1992) Enhanced boiling heat transfer by surfactant additives. In: Pool and External Flow Boiling. ASME, New York, pp 361–366
Wu WT, Yang YM, Maa JR (1995) Enhancement of nucleate boiling heat transfer and depression of surface tension by surfactant additives. J Heat Transfer 117:526–529
Yang H, Lee F, Chein R (2006) Micro-channel heat sink fabrication with roughened bottom walls. Microsyst Technol 12:760–765
Yang YM, Maa JR (2003) Boiling heat transfer enhancement by surfactant additives. In: Proceedings of the 5th International Conference Boiling Heat Transfer, ICBHT, Montego Bay, Jamaica, 4–8 May 2003
Yao SC, Chang Y (1983) Pool boiling heat transfer in a narrow space. Int J Heat Mass Transfer 26:841–848
Yen T-H, Shoji M, Takemura F, Suzuki Y, Kasagi N (2006) Visualization of convective boiling heat transfer in single micro-channels with different shaped cross-sections. Int J Heat Mass Transfer 49:3884–3894
Yoo JY (2006) Recent studies on fluid flow and heat transfer in thermal microdevices. Nanoscale Microscale Thermophys Eng 10:67–81
Yoon DS, Lee Y-S, Lee Y, Cho HJ, Sung SW, Oh KW, Cha J, Lim G (2002) Precise temperature control and rapid thermal cycling in a micromachined DNA polymerase chain reaction chip. J Micromech Microeng 12:813–823
Yu DL, Warrington RO, Barron RF, Ameel T (1995) An experimental and theoretical investigation of fluid flow and heat transfer in micro-tubes. ASME/JSME Thermal Eng Conf 1:523–530
Zhang J, Manglik RM (2005) Additive adsorption interfacial characteristics of nucleate pool boiling in aqueous surfactant solutions. J Heat Transfer ASME 127:684–690
Zhang L, Goodson KE, Kenny TW (2004). Silicon micro-channel heat sinks. Springer-Verlag Berlin Heidelberg
Zhang Z (2007) Nano/Micro-scale Heat Transfer. McGraw-Hill
Zhao YH, Masuoka T, Tsuruta T (2002) Unified theoretical prediction of fully developed nucleate boiling and critical heat flux based on a dynamic microlayer model. Int J Heat Mass Transfer 45:3189–3197
Zheng Y, Lin Z, Zakin JL, Talmon Y, Davis HT, Scriven LE (2000) Cryo-TEM imaging the flow induced transition from vesicles to threadlike micelles. J Phys Chem B 104(22):5263–5271

Nomenclature

A	Surface area
B	Bias limit
C	Concentration
C_0	Characteristic concentration
c_p	Heat capacity at constant pressure
d	Diameter
G	Mass flux, mass velocity of liquid plus vapor
g	Acceleration due to gravity
h	Heat transfer coefficient

h_{LG}	Latent heat
H	High, depth
K	Subcooling parameter
k	Thermal conductivity
k_{s}	Surface roughness
L	Channel length
m	Mass flow rate
N	Power, number of sample
N	Number of channels
P	Pressure, precession limit
Q	Heat rate
q	Heat flux
R	Thermal resistance, gas constant, auto-correlation function, radius
r	Radius, ration of channel length to block width
S	Distance between channels
T	Temperature
U	Average flow velocity in micro-channel, uncertainty
U_{LS}	Superficial liquid velocity
U_{GS}	Superficial gas velocity
u^*	Shear velocity
V	Volume
w	Width
x, y, z	Cartesian coordinates
$\mathrm{Bn} = \delta[\frac{g(\rho_{\mathrm{L}} - \rho_{\mathrm{G}})}{\sigma}]^{0.5}$	Bond number
$\mathrm{Bo} = \frac{q}{Gh_{\mathrm{LG}}}$	Boiling number
$\mathrm{Kn} = \frac{\overline{\lambda}}{d_{\mathrm{h}}}$	Knudsen number
$\mathrm{Ma} = \frac{U}{U_{\mathrm{sound}}}$	Mach number
$\mathrm{Nu} = \frac{hd_{\mathrm{h}}}{k}$	Nusselt number
$\mathrm{Po} = \lambda \cdot Re$	Poiseuille number
Pr	Prandtl number
$\mathrm{Re} = \frac{Ud_{\mathrm{h}}}{\nu}$	Reynolds number
$\mathrm{We} = \frac{G^2 d_{\mathrm{h}}}{\sigma\rho}$	Weber number

Greek symbols

δ	Gap size, thickness
ΔP	Pressure drop
ΔT	Temperature difference
φ	Ratio of total heated area to circuit area
$\overline{\Phi}$	Pressure drop ratio
$\overline{\lambda}$	Wave length, mean free path
$\lambda = 2\Delta P \frac{d_\mathrm{h}}{L} \frac{1}{\rho U^2}$	Friction factor
μ	Dynamic viscosity
ν	Kinematic viscosity
ρ	Density
σ	Surface tension
τ	Shear stress
χ	Vapor quality
θ	Contact angle
η	Shear viscosity
ϖ	Shear rate

Subscripts

c	Channel
cond	Conduction
conv	Convection
CHF	Critical heat flux
crit	Critical
dry	Dryout
eff,m	Heated platform area
exp	Experimental
film	Film
G	Gas
h	Hydraulic, heated
heat	Heat
in	Inlet
L	Liquid
LG	Liquid/gas
max	Maximum
mean	Average
min	Minimum
out	Outlet
p	Liquid-bubble slug

pm	Heated inside area
pred	Predicted
r	Row
s	Saturation
sound	Sound
sub	Subcooled
theory	Theory
w	Wall